

Thermo-Hydro-Mechanical Properties of Cobourg Limestone

NWMO-TR-2014-26

December 2014

M.H.B. Nasser and R.P. Young

University of Toronto

nwmo

NUCLEAR WASTE
MANAGEMENT
ORGANIZATION

SOCIÉTÉ DE GESTION
DES DÉCHETS
NUCLÉAIRES

Nuclear Waste Management Organization

22 St. Clair Avenue East, 6th Floor

Toronto, Ontario

M4T 2S3

Canada

Tel: 416-934-9814

Web: www.nwmo.ca

Thermo-Hydro-Mechanical Properties of Cobourg Limestone

NWMO-TR-2014-26

December 2014

M.H.B. Nasser and R. P. Young
University of Toronto

This report has been prepared under contract to NWMO. The report has been reviewed by NWMO, but the views and conclusions are those of the authors and do not necessarily represent those of the NWMO.

All copyright and intellectual property rights belong to NWMO.

Document History

Title:	Thermo-Hydro-Mechanical Properties of Cobourg Limestone		
Report Number:	NWMO-TR-2014-26		
Revision:	R000	Date:	December 2014
University of Toronto			
Authored by:	M.H.B. Nasserri and R. P. Young		
Verified by:	R. P. Young		
Approved by:	R. P. Young		
Nuclear Waste Management Organization			
Reviewed by:	Tom Lam		
Accepted by:	Mark Jensen		

ABSTRACT

Title: Thermo-Hydro-Mechanical Properties of Cobourg Limestone
Report No.: NWMO-TR-2014-26
Author(s): M. H. B. Nasser and R. P. Young
Company: University of Toronto
Date: December 2014

To improve understanding of the effects of Thermo-Hydro-Mechanical (THM) processes, as well as the individual coupled effects of the processes on Cobourg limestone, a two-phase experimental program was undertaken at the Rock Fracture Dynamics Laboratory at University of Toronto.

In Phase 1, uniaxial compressive strength tests on dry and saturated samples of 50 and 38 mm diameter were conducted to measure the ultrasonic wave-velocity changes and permeability changes with temperature under Hydrostatic pressure equivalent to the lithostatic stress at 500 m depth. The uniaxial compressive strength (UCS) of dry and saturated samples show that the limestone is generally strong but variable reflecting sample heterogeneity. There appears no specific trend in strength or Young's modulus with changing temperature when specimens are subjected to pre-heating. The results also suggest that the permeability of the samples, ranging between 10^{-19} and 10^{-20} m², decreases with an increase in hydrostatic stress and with increasing temperature. The latter will result in a decrease of approximately an order of magnitude when temperature increases from ambient temperature of 25°C to 125°C. This reduction in permeability may be attributed to changes in the interconnectivity of the pore network resulting from the expansion of clay material.

In the Phase 2 experimental program, physical property, uniaxial compression and THM triaxial compression testing were performed on dry and saturated samples which were stepwise thermally treated to 150°C while subjected to mechanical loading. The results show that a self-consistent relationship exists between strength, deformation, wave velocities, elastic constants and permeability during the various heating stages, despite the heterogeneous and anisotropic nature of the limestone.

TABLE OF CONTENTS

	<u>Page</u>
ABSTRACT	iii
1. INTRODUCTION	1
2. THM PROPERTIES OF COBOURG LIMESTONE: PHASE 1.....	2
2.1 INTRODUCTION	2
2.2 EXPERIMENTAL METHODS.....	2
2.2.1 Physical Properties Measurement	2
2.2.2 Permeability Measurement	3
2.2.3 Uniaxial Compressive Strength (UCS) Tests.....	3
2.2.4 Hydrostatic Thermo-Hydro Experiments.....	4
2.3 EXPERIMENTAL RESULTS FROM PHASE 1.....	6
2.3.1 Physical Property Tests	6
2.3.2 Uniaxial Compression Test.....	6
2.3.3 Strength Anisotropy of Samples	21
2.3.4 Evolution of Seismic Velocity with Stress	22
2.3.5 Evolution of Seismic Velocity with Temperature	24
2.3.6 Evolution of Permeability with Stress.....	25
2.3.7 Evolution of Permeability with Temperature	29
2.3.8 Effect of Thermal Expansion on Test Results.....	30
2.4 DISCUSSION OF PHASE 1 RESULTS	35
3. THM PROPERTIES OF COBOURG LIMESTONE: PHASE 2.....	36
3.1 INTRODUCTION	36
3.2 EXPERIMENTAL METHODS	37
3.2.1 Physical Properties Measurement	37
3.2.2 Permeability Measurement	37
3.2.3 Uniaxial Compressive Strength (UCS) Tests.....	37
3.2.4 Triaxial Thermo-Hydro-Mechanical Experiments.....	39
3.2.5 Dynamic Elastic Constants	41
3.3 RESULTS FROM PHASE 2 TESTING	41
3.3.1 Physical Properties	41
3.3.2 Uniaxial Compressive Strength Test	41
3.3.3 Triaxial Thermo-Hydro-Mechanical Tests.....	49
3.3.3.1 Testing at Room Temperature, HM Tests	49
3.3.3.2 Testing at 50°C, THM Tests.....	54
3.3.3.3 Testing at 100°C, THM Tests.....	63
3.3.3.4 Testing at 150°C, THM Tests.....	74
3.3.4 Specimen L7.....	75
3.3.5 Specimen L8.....	80
3.3.6 Thermal Expansion Coefficient of Cobourg Limestone.....	91
3.4 DISCUSSION OF PHASE 2 RESULTS	94
4. SUMMARY AND CONCLUSIONS.....	103

ACKNOWLEDGEMENTS	105
REFERENCES	107
APPENDIX A: ACOUSTIC EMISSION ANALYSIS	109

LIST OF TABLES

	<u>Page</u>
Table 1: Summary of testing in Phase 1.....	2
Table 2: Physical properties of Cobourg Limestone.....	6
Table 3: Peak UCS and deformation properties of dry Cobourg Limestone specimens from Darlington	9
Table 4: Peak UCS and deformational properties of saturated Cobourg Limestone specimens from Darlington.....	9
Table 5: Summary of testing in Phase 2.....	36
Table 6: Physical properties of Cobourg Limestone measured in the laboratory	42
Table 7: UCS Values of all the Tested Specimens	44
Table 8: Dynamic elastic constant calculated along three axes for Specimen RT6b.	54
Table 9: Variation of dynamic elastic constant along three axes during heating of Specimen L3 up to 50°C.....	60
Table 10: Variation of dynamic elastic constant along three axes during heating of Specimen L4 up to 50°C.	61
Table 11: Variation of dynamic elastic constants along three axes during the heating up to 100°C for Specimen L5.	70
Table 12: Variation of dynamic elastic constants along three axes during heating up to 100°C of Specimen L9.....	71
Table 13: Variation of dynamic elastic constants along three axes during heating up to 150 °C and as a function of vertical stress for Specimen L7.	78
Table 14: Variation of dynamic elastic constant along three axes during first cycle of heating up to 150°C for Specimen L8	83
Table 15: Variation of dynamic elastic constant along three axes during 2 nd cycle of heating up to 150 °C under load control (axial expansion was allowed) for Specimen L8	90

LIST OF FIGURES

	<u>Page</u>
Figure 1: Preparation of samples with four strain gauges: two units for axial strain change and two units for diametric strain change.....	4
Figure 2: Floor Standing Acoustic System for testing under thermal treatment and hydrostatic pressures	5
Figure 3: A schematic view of FSAS experimental arrangement	5
Figure 4: A picture of premature failure of Specimen C5 due to a pre-existing inclined feature	7
Figure 5: Pictures of pre-mature failure of Specimen C16 and C24 (saturated), thermally treated at 75 and 100°C before testing.....	7
Figure 6: Comparison between UCS of (a) dry and (b) saturated Cobourg Limestone.....	8
Figure 7: Comparison between dry and saturated Young's moduli of Cobourg Limestone.....	10
Figure 8: Stress-strain plots of dry Specimens C10, C11 and C12 at ambient temperature ...	10
Figure 9: Volumetric strain of dry Specimens C10, C11 and C12 at ambient temperature	11
Figure 10: Stress-strain plots of dry Specimens C1, C7 and C25 thermally treated at 50°C.....	11
Figure 11: Volumetric strain of dry Specimens C1, C7 and C25 at 50°C	12
Figure 12: (a) Stress-strain Plots of dry Specimens C5, C6 and C23, thermal treatment at 75°C. (b) Specimen C6 experiences axial splitting failure whereas Specimen C5 shows pre-mature failure due to a pre-existing inclined feature	13
Figure 13: Volumetric strain of dry Specimens, C5, C6 and C23, thermally treated at 75°C.....	14
Figure 14: Stress-strain plots of dry Specimens, C8, C9 and C13 thermally treated at 100°C..	15
Figure 15: Volumetric strain of dry Specimens C8, C9 and C13, thermally treated at 100°C ...	16
Figure 16: Stress-strain plots of saturated Specimens, C3 and C17 for ambient temperature .	16
Figure 17: (a) Volumetric strain for saturated Specimens, C3 and C17, for ambient temperature and (b) a 75° inclined failure plane of Specimen C17	17
Figure 18: (a) A photo of saturated Specimens, C18, C19 and C20, thermally treated at 50°C prior to testing and (b) Stress-strain plots of the three saturated specimens .	18
Figure 19: Volumetric strain of saturated Specimens C18, C19 and C20, thermally treated at 50°C.....	19
Figure 20: (a) A photo of saturated Specimens C21, C22 and C24, thermally treated at 75°C prior to Testing. (b) Stress-strain Plots of the three specimens.....	19
Figure 21: Volumetric strain of saturated Specimens C21, C22 and C24, thermally treated at 75°C.....	20
Figure 22: (a) A photo showing heterogeneous and anisotropic nature of Specimens C14, C15 and C16, thermally treated at 100°C and (b) Stress-strain plots of the three specimens	20
Figure 23: Volumetric strain of saturated Specimens C14, C15 and C16, thermally treated at 100°C.....	21
Figure 24: Cobourg specimens characterized with inclined features at different orientations (C16 and C17 – after tests and C14 – before test).....	22
Figure 25: Variation of UCS with inclined feature orientation (β) in Cobourg specimens	22
Figure 26: Variation of V_p , with hydrostatic stress during loading and unloading of Specimen S0	23
Figure 27: Variation of V_s , with hydrostatic stress during loading and unloading of Specimen S0	23
Figure 28: Evolution of V_p with hydrostatic stress increments up to 12.5 MPa of Specimens S0, S2 and S3	24

Figure 29: Evolution of V_s with Hydrostatic Stress Increments up to 12.5 MPa of Specimens S0, S2 and S3	24
Figure 30: Evolution of V_p with Temperature Increments up to 125°C of Specimens S0, S2 and S3	25
Figure 31: Evolution of V_s with hydrostatic stress increments up to 125°C of Specimens S0, S2 and S3	26
Figure 32: Decrease in elastic-wave velocities as temperature increase in Specimens S0, S2 and S3	26
Figure 33: Variation of dynamic Young's modulus as a function of hydrostatic stress at a constant temperature up to 12.5 MPa and of temperature at constant stress up to 100°C	27
Figure 34: Decay of pore pressure with time in a typical pulse decay measurement used for permeability determination	28
Figure 35: Permeability decreases with increase in hydrostatic pressure, indicating the closure of well-connected pores	28
Figure 36: Evolution of permeability with temperature up to 125°C for Specimen S4	29
Figure 37: Evolution of permeability during temperature increase at a constant stress Specimen S2.	30
Figure 38: The evolution of the coefficient of thermal expansion of water with increase in temperature (Horseman and McEwen, 1996)	30
Figure 39: Evolution of V_p under a constant 12.5 MPa hydrostatic stress under ambient temperature (the red line), and during temperature increase (the blue line) of Specimen S3	31
Figure 40: Evolution of V_s under a constant 12.5 MPa under ambient temperature (the red line), and during temperature increase (the blue line) of Specimen S3	32
Figure 41: Variation of axial strain (%) and seismic wave velocities with temperature, Specimen S3	32
Figure 42: Axial elongation (blue) due to sample expansion and permeability (pink) reduction with temperature in Specimen S3	33
Figure 43: Axial strain (blue) decrease and permeability (pink) decrease with temperature in Specimen S3	34
Figure 44: Variation of seismic wave velocities, permeability, axial strain and hydrostatic stress with temperature for Cobourg Limestone	34
Figure 45: St. Mary's cement's quarry in Bowmanville and cored samples	36
Figure 46: Micro-CT images of a Cobourg specimen (carried out by the U. of Toronto's Geomechanics group)	38
Figure 47: Setup for the comparison of axial measurements by LVDTs and strain gauges.	39
Figure 48: (a) The geophysical imaging cell's internal view of the confining rubber and the X and Y direction velocity stacks along with rock specimen and (b) the cell being setup in the MTS loading machine for testing.	40
Figure 49: Stress-strain plots of dry Specimen L1-RT, UCS testing	43
Figure 50: Stress-strain plots of dry Specimen L2-RT, UCS testing	43
Figure 51: Stress-strain plots of saturated Specimen L3-RT, UCS testing	45
Figure 52: Stress-strain plots of saturated Specimen L4-RT, UCS testing	45
Figure 53: A photo of Specimens L1-RT, L2-RT, L3-RTS and L4-RTS after tests	46
Figure 54: Stress-strain plots of Specimens L1-50 C, L2-50 C and L3-50 C, thermally treated at 50°C	46
Figure 55: Stress-strain plots of Specimens L1-100 C, L2-100 C and L3-100 C, thermally treated at 100°C	47

Figure 56: Stress-strain plots of Specimens L1-150 C, L2-150 C and L3-150 C, thermally treated at 150°C	47
Figure 57: A photo of thermally treated Specimens L1-50 C, L2-50 C and L3-50 C after tests	48
Figure 58: A photo of thermally treated Specimens L1-100 C, L2-100 C and L3-100 C after tests	48
Figure 59: A photo of thermally treated Specimens L1-150 C, L2-150 C and L3-150 C after tests	49
Figure 60: Axial, diametral and volumetric strain plots of Specimen L6b under HM testing.....	50
Figure 61: Evolution of V_P along two horizontal directions (X and Y axes) and the vertical direction (Z axis), with differential stresses in coupled HM testing of Specimen L6b under ambient temperature	51
Figure 62: Evolution of (a) V_{S1} , and (b) V_{S2} with differential stresses in coupled HM testing of Specimen L6b under ambient temperature	52
Figure 63: Evolution of shear wave splitting (SWS) with differential stresses in coupled HM testing of Specimen L6b under ambient temperature.....	52
Figure 64: A photo of Specimens L2 and L6b after tests.....	53
Figure 65: Variation of dynamic Young's moduli with differential stresses for Specimen L6b...	54
Figure 66: Stress-strain and volumetric strain plots of Specimen L3.....	55
Figure 67: Stress-strain and diametral strain plots of Specimen L4	56
Figure 68: Evolution of (a) V_P and (b) V_S along Y and Z axes of Specimen L3 during heating and differential stress increments.....	57
Figure 69: Evolution of V_{S2} along the Y and Z axes of Specimen L3 during heating and differential stress increments.....	57
Figure 70: Evolution of (a) V_P and (b) V_S along Y and Z axes of Specimen L4 during heating and differential stress increments.....	58
Figure 71: Evolution of V_{S2} along the Y and Z axes of Specimen L4 during heating and differential stress increments.....	58
Figure 72: A photo of Specimens L3 and L4 after tests.....	59
Figure 73: Evolution of dynamic Young's moduli with differential stresses in Z and Y directions for Specimen L3	60
Figure 74: Evolution of dynamic Young's moduli with differential stresses in Z and Y directions for Specimen L4	61
Figure 75: Evolution of permeability and V_p of Specimen L3 as a function of hydrostatic stress at room temperature (value shown in the red circle), and as a function of increased axial stress increments.	62
Figure 76: Evolution of permeability (RT k) and V_p of Specimen L4 as a function of hydrostatic stress at room temperature and as a function of increased axial stress increments (50°C k).....	63
Figure 77: Stress-strain and diametral strain plots of Specimen L5	64
Figure 78: Axial, diametral and volumetric strain during in-situ heating of Specimen L5 under the MTS displacement control mode.....	64
Figure 79: Stress-strain and diametral strain plots of Specimen L9	65
Figure 80: Axial, diametral and volumetric strain during in-situ heating of Specimen L9 under the MTS displacement control mode.....	66
Figure 81: A photo of Specimens L5 and L9 after testing.....	66
Figure 82: Evolution of (a) V_P and (b) V_S along the X, Y and Z axes of Specimen L5 during heating and differential stress increments. The points in the box show the effect of thermal heating.....	67

Figure 83: Variation of V_{S2} along the X, Y and Z axes of Specimen L5 during heating and differential stress increments. The points in the box show the effect of thermal heating.....	68
Figure 84: Variation of (a) V_P and (b) V_S along the X, Y and Z axes of Specimen L9 during heating and differential stress increments. The points in the box show the effect of thermal heating.....	68
Figure 85: Variation of V_{S2} along the X, Y and Z axes of Specimen L9 during heating and differential stress increments.....	69
Figure 86: Evolution of dynamic moduli of Specimen L5 with differential stresses along X, Y and Z directions.....	71
Figure 87: Evolution of moduli of Specimen L9 with differential stresses along X, Y and Z directions.....	72
Figure 88: Evolution of permeability and V_p of Specimen L5 as a function of hydrostatic stress, and as a function of increased temperature, and differential stress increments.....	73
Figure 89: Evolution of permeability and V_p of Specimen L9 as a function of hydrostatic stress, and as a function of increased temperature, and differential stress increments.....	73
Figure 90: Stress-strain and diametral strain plots of Specimen L7.....	74
Figure 91: Axial, diametral and volumetric strains of Specimen L7 during in-situ heating under the displacement control mode.....	75
Figure 92: Evolution of (a) V_P and (b) V_{S1} along the X, Y and Z axes of Specimen L7 during heating and differential stress increments.....	76
Figure 93: Evolution of (a) V_{S2} along the X, Y and Z axes of Specimen L7 during heating (value shown with the green rectangle) and differential stress increments and (b) shear wave splitting as a function of heating and thermal expansion.....	76
Figure 94: A photo of Specimens L7 and L8 after testing.....	77
Figure 95: Evolution of moduli with differential stresses along X, Y and Z directions of Specimen L7.....	79
Figure 96: Evolution of permeability of Specimen L7 as a function of hydrostatic at ambient temperature, as a function of thermal stress measured at 150°C temperature and differential stress increments.....	80
Figure 97: Stress-strain, thermal pressurization and volumetric strain plots of Specimen L8 ...	81
Figure 98: Axial, diametral and volumetric strain plots of Specimen L8 during in-situ heating under displacement control mode.....	81
Figure 99: Evolution of (a) V_P and (b) V_{S1} along the X, Y and Z axes during heating of the L8 specimen up to 150°C.....	82
Figure 100: Evolution of (a) V_{S2} along the X, Y and Z axes as a function of thermal pressurization during the heating of Specimen L8 up to 150°C and (b) shear wave splitting as a function of heating.....	82
Figure 101: Evolution of moduli of Specimen L8 with temperature up to 150°C along X, Y and Z directions during first cycle of heating.....	83
Figure 102: Evolution of permeability of Specimen L8 as a function of thermal stress.....	84
Figure 103: Axial, diametral and volumetric strains of Specimen L8 during heating up to 150°C under load control mode.....	85
Figure 104: Axial, diametral and volumetric strain plots of Specimen L8.....	86
Figure 105: Evolution of (a) V_P and (b) V_{S1} along the X, Y and Z axes during heating and differential stress increments. Points in the boxes show the effect of thermal heating.....	87

Figure 106: Variation of (a) V_{S2} along the X, Y and Z axes as a function of thermal pressurization during the heating of the L8 specimen up to 150°C and (b) shear wave splitting as a function of heating. Points in the boxes show the effect of thermal heating.....	87
Figure 107: Variation of V_P as a function of axial expansion caused by heating (thermal expansion) for Specimen L8.....	88
Figure 108: Variation of V_{S1} as a function of axial expansion caused by heating (thermal expansion) for Specimen L8.....	88
Figure 109: Variation of V_{S2} as a function of axial expansion caused by heating (thermal expansion) for Specimen L8.....	89
Figure 110: Evolution of moduli of Specimen L8 with temperature increase to 150° C along X, Y and Z directions during 2nd cycle of heating under load control	90
Figure 111: Evolution of permeability and V_P of Specimen L8 as a function of differential stress, tested at ambient temperature and as a function of increased temperature. 91	91
Figure 112: Variation of α (1/K) with in situ heating temperature for Specimens L5 and L9.....	92
Figure 113: Variation of α (1/K) with in situ heating temperature for Specimen L8 during the 1 st and 2 nd cycle of heating.	93
Figure 114: Thermal expansion curves for Specimens L5 and L9.....	93
Figure 115: Thermal expansion curves for L8 for the 1 st and 2 nd cycles of heating up to 150°C	94
Figure 116: Stress-strain plots for RT, 50 °C, 100 °C and 150°C specimens tested under coupled THM.	96
Figure 117: Variation of V_{PZ} (compression wave along vertical direction) for RT, 50°C, 100°C and 150°C during in-situ heating. Points in the box and oval circles show the effect of thermal heating	97
Figure 118: (a) Evolution of V_P along the X axis for RT, 50°C, 100°C and 150°C during in-situ heating (values shown within oval and rectangle), and as a function of differential stresses under constant σ_3 and constant displacement control and (b) Evolution of V_{PY} in the other horizontal axis.	98
Figure 119: Evolution of (a) V_{S1Z} and (b) V_{S2Z} (vertical direction) for RT, 50°C, 100°C and 150°C during in-situ heating (values shown in ovals and rectangles).....	98
Figure 120: Evolution of (a) V_{S1} and (b) V_{S2} along the X axis for RT, 50°C, 100°C and 150°C during in-situ heating (values shown in the oval and rectangle).....	99
Figure 121: Variation of moduli along Z axis for RT, 50°C, 100°C and 150°C during in-situ heating (values shown in oval).	100
Figure 122: Variation of moduli along Y axis for RT, 50°C, 100°C and 150°C during in-situ heating (values shown in oval),	100
Figure 123: Variation of E_{dX} (dynamic Young's modulus along X axis) for RT, 50°C, 100°C and 150°C during in-situ heating (values shown in oval and rectangle).	101
Figure 124: Permeability as a function of differential stresses measured under ambient temperature (25°C, RT K) and elevated temperatures	102
Figure 125: UCS and triaxial compressive strengths as a function of temperature for all specimens in Phase 2	102

1. INTRODUCTION

The Nuclear Waste Management Organization (NWMO) is responsible for implementing Adaptive Phased Management (APM), Canada's plan for the long-term disposal of used nuclear fuel produced by Canada's nuclear reactors. In support of APM implementation, NWMO pursues applied Research and Development Programs including a multi-component strategy to address THM modelling capabilities in support of performance assessment. The purpose of this research is to improve the understanding of THM coupled processes as measured at the laboratory-scale on the fluid transport properties of sedimentary rock.

This two-phase experimental program investigates THM processes in the Cobourg argillaceous limestone from southern Ontario and was implemented at the Rock Fracture Dynamics Laboratory (RFDL) at University of Toronto. The RFDL is an integrated rock testing facility with geophysical imaging and hydraulic testing systems. The RFDL's unique polyaxial testing apparatus can perform tests on thermally treated samples under uniaxial to triaxial conditions to investigate the effect of temperature on strength and deformational responses.

2. THM PROPERTIES OF COBOURG LIMESTONE: PHASE 1

2.1 INTRODUCTION

The purpose of Phase 1 testing is to experimentally investigate the coupled thermo-hydro-mechanical (THM) properties of the Cobourg argillaceous limestone. Uniaxial compressive strength (UCS) tests were carried out on saturated and dry specimens that have been thermally treated (pre-heating) to understand the thermo-mechanical responses of limestone. The pre-heating process is when a core sample is subjected to heating treatment prior to mechanical testing. Limestone specimens of 54 mm diameter selected for the testing were obtained from the Darlington area. They were retrieved from investigation boreholes drilled as part of Darlington nuclear development field investigation from the near surface depth between 20 and 40 meters and were kept in a core storage facility for the past 20 years. The pre-heating UCS testing is presented in the following sections and is summarized in Table 1.

In the late part of the project, THM responses of the same Cobourg limestone were studied under triaxial stresses, using a geophysical imaging system. The effect of in-situ heating on strength and transport properties of the limestone was evaluated. In-situ heating means when a sample is subjected to heating while it is inside a loading cell under hydrostatic stress. Thirty-seven mm diameter test specimens were cored from a rock sample retrieved from the St. Mary's cement quarry in Bowmanville, Ontario. Details of the THM testing is presented in Section 2.3.3 to 2.3.7.

Table 1: Summary of Testing in Phase 1

Experiment	Diameter of Specimen, mm	Total number of Test	Room Temp.	50°C	75°C	100°C
Physical Property Test	54	3	3			
Uniaxial Compressive Strength Test (dry)	54	12	3	3	3	3
Uniaxial Compressive Strength Test (saturated)	54	12	3	3	3	3
Hydrostatic TH Test (saturated)	37	4	Varies (from 25 to 125°C)			

2.2 EXPERIMENTAL METHODS

2.2.1 Physical Properties Measurement

In this study, porosity was determined using the standard ISRM (1981) water saturation porosity technique. Three representative samples were chosen and their ends were polished to meet with the ISRM standard tolerance for specimen preparation. These specimens were oven-dried for 72 hours at 60°C before the dry weights were taken. Then the samples were saturated with water under vacuum for more than 24 hours before the maximum saturated weights were

measured. The difference between the dry and saturated weights of the samples was used to calculate the effective porosity of the samples using the equation given below. The porosities of the samples were found ranging from 0.77% to 1.19%, with an average of 1.01%. Based on the same approach, dry density, saturated density and void ratio of the specimens were measured (Table 2).

$$\Phi = \frac{V_r - V_{solid}}{V_r} = \frac{V_{pore}}{V_r} = \frac{PoreVolume}{TotalVolume} \quad (1)$$

where Φ is the porosity, V_r is the total volume, V_{solid} is the volume of solid within the rock, and V_{pore} is the pore volume.

2.2.2 Permeability Measurement

Cores with a diameter of 38 mm and approximate 70 mm in length were drilled from blocks of rocks obtained from St. Mary Quarry in Bowemanville, Ontario. The permeability of the limestone was measured as a function of hydrostatic pressure up to 12.5 MPa to simulate a deposition depth of 500 m. A transient method (pulse decay method) suggested by Brace et al. (1968) was used to estimate permeability. This method involves a small step change of pore pressure imposed at one end of the sample, and then measuring the pore pressure decay with time. The pressure gradient decays exponentially to zero, and the pressure P_1 in reservoir 1 is given by following equation. Appendix A shows the detail of the method used here (after Roy et al. 1993).

$$(P_1 - P_f) = \Delta P \left[\frac{V_2}{V_1} + V_2 \right] e^{-\alpha t} \quad (2)$$

where A is the cross-sectional area, L is the length of sample, V_1 and V_2 are volumes of reservoirs 1 and 2, P_f is the final pressure, μ is the viscosity of the water, β is the conversion constant and ΔP is the step change of pressure in reservoir at time = 0. The permeability, k of the sample is found by plotting the pressure decay ($P_1 - P_f$) on semi-log scale with time. The slope of the resulting line is the $-\alpha$, while permeability is found from the following equation.

$$\alpha = (kA / \mu\beta L) (1/V_1 + 1/V_2) \quad (3)$$

2.2.3 Uniaxial Compressive Strength (UCS) Tests

Twenty four cylindrical samples with length-to-diameter ratios of 1: 2.5 L/D ratios, i.e. 54 mm in diameter and approximate 135 mm in length, were prepared (ISRM 1977) and treated at different temperatures prior to the uniaxial compressive strength tests. The samples were divided into two groups: 12 were tested in dry condition and the rest were tested under saturated condition. Within each group, 3 samples were untreated (i.e. at ambient temperature), 3 samples were treated at 50°C, 3 samples were treated at 75°C, and 3 samples were treated at 100°C. The UCS tests were carried out according to the ISRM (1977) suggested methods for determining the uniaxial compressive strength and deformability of rock materials. Electrical resistance strain gauges were used for the measurement of strain. Figure 1 shows the mounting

of four electrical resistance strain gauges for the measurement of axial and circumferential strains. All four strain gauges were mounted at mid-height of the sample. Two strain gauges were mounted parallel to the vertical axis of the sample for axial strain measurements, and two were mounted perpendicular to the vertical axis of the sample for circumferential strain measurements. The axial and circumferential strains were calculated by averaging the sets of strain gauges attached to the specimen surface in vertical and horizontal directions, respectively.

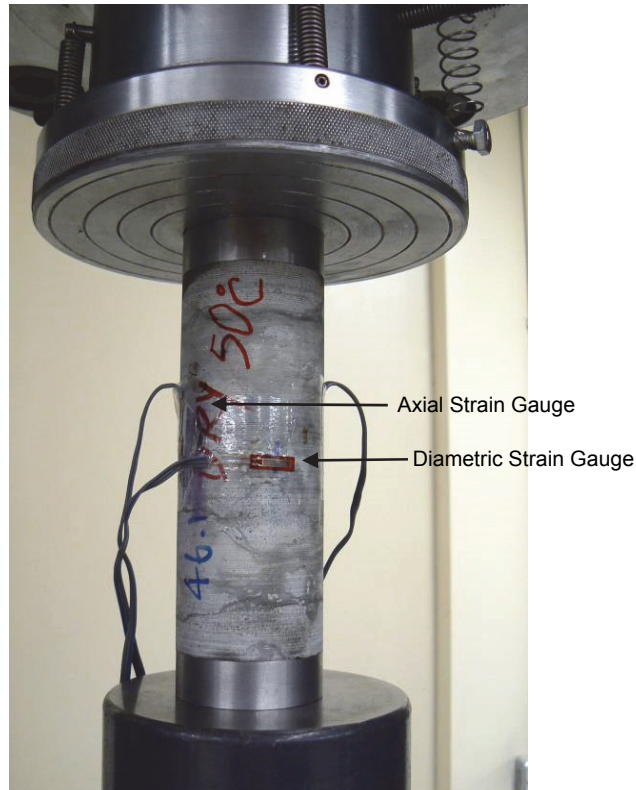


Figure 1: Preparation of samples with four strain gauges: two units for axial strain change and two units for diametric strain change

2.2.4 Hydrostatic Thermo-Hydro Experiments

Four samples of 37 mm diameter and 75 mm length were tested under hydrostatic pressure of 12.5 MPa (maximum). This mimics the lithostatic pressure at 500 m underground. The Floor Standing Acoustic System (FSAS) is equipped with ultrasonic-wave velocity stacks (Figure 2). During experiments, the saturated samples were loaded gradually to 12.5 MPa and then, after increasing the pore water pressure up to 4 - 5 MPa, the internal heater is turned on to regulate the temperature increase at steps of 25°C up to 125°C. The permeability of specimens at each temperature was measured using the pulse decay method. In addition, seismic wave velocities were measured during the tests to observe transient changes in rock matrix properties. Figure 3 shows a schematic diagram of the Floor Standing Acoustic System.



Figure 2: Floor Standing Acoustic System for testing under thermal treatment and hydrostatic pressures

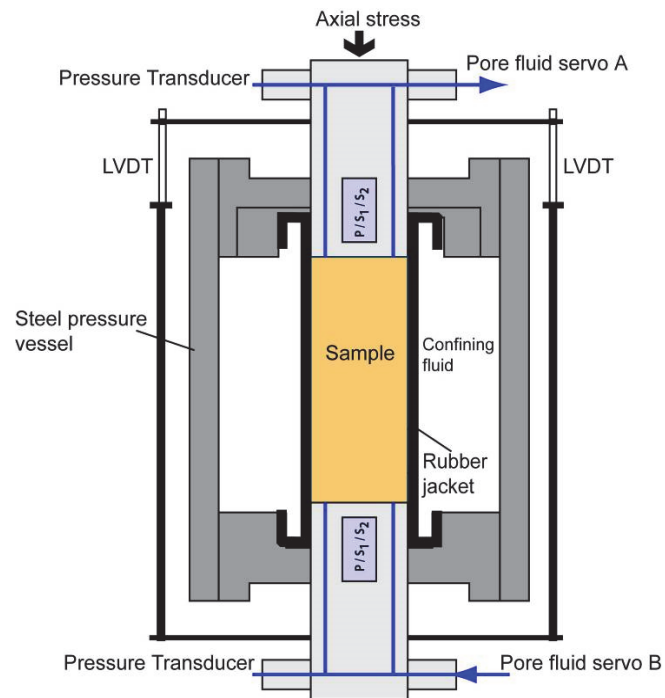


Figure 3: A schematic view of FSAS experimental arrangement

2.3 EXPERIMENTAL RESULTS FROM PHASE 1

The investigation study is divided into the following four parts:

1. The physical properties of the Cobourg limestone,
2. The variation of uniaxial compressive strengths, and the deformational properties for dry and saturated pre-heat treated specimens up to 100°C,
3. The evolution of permeability with increasing hydrostatic pressures at ambient and stepwise increase of temperature up to 125°C (in-situ heating), and
4. The evolution of ultrasonic-wave velocities as a function of hydrostatic stress and temperature.

2.3.1 Physical Property Tests

The determination of the physical properties of the limestone has been carried out based on ISRM (1977) and the results are presented in Table 2.

Table 2: Physical Properties of Cobourg Limestone

Sample	L cm	Dia. cm	Dry wt. g	Sat. wt. g	Porosity %	Dry den. g/cc	Sat. den. g/cc	Void ratio
P1	8	5.4	497.9	500	1.06	2.67	2.68	0.01
P2	9.5	5.5	589.5	592	1.19	2.64	2.66	0.01
P3	13	5.5	787.8	790	0.77	2.67	2.68	0.01

2.3.2 Uniaxial Compression Test

A total of 12 uniaxial compressive strength (UCS) tests were carried out on pre-heat treated dry specimens. The results reveal that the pre-heating process has no influence on the UCS. Uniaxial compressive strength of all dry specimens shows an average value of 121 MPa excluding the result from Specimen C5 which was a pre-maturely failed specimen on an existing inclined weak plane (Figure 4). The test on Specimen C5 measured a much lower value of 58 MPa (Table 3). The corresponding standard deviation for all pre-heated specimens up to 100°C is 20 MPa.

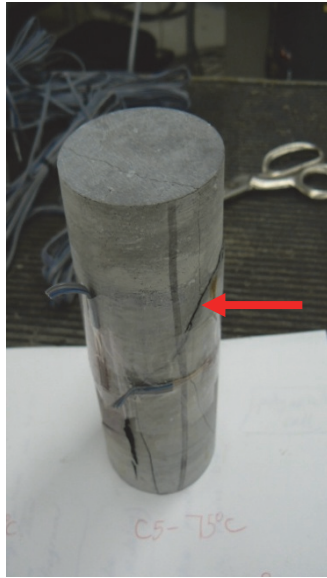


Figure 4: A picture of premature failure of Specimen C5 due to a pre-existing inclined feature

A total of 12 UCS tests were carried out on pre-heat treated saturated specimens. Similar to the dry specimen results, the UCS is not significantly influenced by the pre-heating process. The uniaxial compressive strength of saturated specimens shows an average value of 87.61 MPa excluding the test values of C16 and C24 specimens, which both contain inclined existing weak planes resulting in pre-mature failure (Figure 5). The standard deviation calculated is 15.53 MPa (Table 3).



Figure 5: Pictures of pre-mature failure of Specimen C16 and C24 (saturated), thermally treated at 75 and 100°C before testing

Figure 6 shows the comparison between saturated and dry UCS values for the tested specimens at ambient temperature and thermally treated ones up to 100°C. Under both conditions, it appears that the pre-heated treatment does not have a significant effect on the

UCS and the elastic properties of the rock. Values for the dry UCS show a larger spread varying from 90 to 160 MPa, where such a spread is limited to a range between 67 and 100 MPa for saturated specimens.

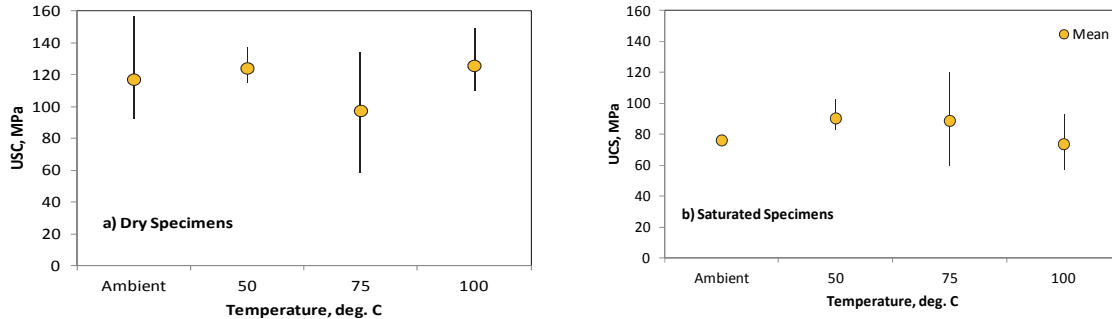


Figure 6: Comparison between UCS of (a) dry and (b) saturated Cobourg Limestone

Table 3 also shows range of Young's moduli, Poisson's ratios and maximum volumetric strains for dry Cobourg limestone. These deformational properties were obtained from stress-strain curves for each group of specimens (3 in each group) at ambient temperature and pre-heated to 50, 75 and 100°C prior to testing. Figure 7 shows variation between the saturated and dry Young's moduli for Cobourg limestone. Similar trend to UCS variation is observed for their deformational properties. The scatter for dry Young's modulus values is larger than the one observed for saturated specimens. Figures 8 to 23 shows the stress-strain and volumetric strain curves and the failure patterns of some specimens subjected to pre-mature failure which demonstrates the influence of a pre-existing inclined feature on rock strength. The average Young's modulus, Poisson's ratio and maximum volumetric strain for these groups of dry specimens are 67.39 GPa, 0.27 and 0.08%, respectively with respective standard deviation of 24GPa , 0.09 and 0.05%.

Table 3: Peak UCS and Deformation Properties of Dry Cobourg limestone Specimens from Darlington

Temperature (°C)	Dry Sample ID	Peak UCS (MPa)	E_t (GPa)	ν	Maximum ϵ_v %	E/ν	Comments
Ambient	C10	102.88	49.4	0.20	0.160	247.1	
Ambient	C11	92.07	95.0	0.30	0.019	316.7	
Ambient	C12	156.18	47.2	0.22	0.160	214.4	
50	C1	136.45	74.6	0.17	0.060	438.8	
50	C7	114.89	74.0	0.20	0.080	370.0	
50	C25	120.88	60.0	0.34	0.050	176.5	
75	C5	58.08	31.0	0.21	0.110	147.6	Pre-Mature Failure
75	C6	100.31	123.0	0.49	0.060	251.0	
75	C23	133.81	50.0	0.31	0.060	161.3	
100	C8	110.14	75.0	0.27	0.043	277.8	
100	C9	117.45	74.0	0.27	0.029	274.1	
100	C13	149.48	39.4	0.29	0.065	135.9	

Table 4: Peak UCS and Deformational Properties of Saturated Cobourg Limestone Specimens from Darlington

Temperature (°C)	Saturated Sample ID	Peak UCS (MPa)	E_t (GPa)	ν	Max Vol. Strain ϵ_v , %	E/ν	Comments
Ambient	C3	75.7	19.6	0.50	0.210	163	
Ambient	C17	76.5	36.5	0.17	0.200	145	
50	C18	83.0	38.4	0.26	0.160	147	
50	C19	103.0	84.5	0.28	0.089	301	
50	C20	85.0	27.6	0.15	0.180	307	
75	C21	120.0	50.2	0.37	0.044	135	
75	C22	86.7	34.2	0.45	0.019	76	
75	C24	59.6	8.7	0.25	0.123	74	Pre-mature failure
100	C14	93.0	31.4	0.28	0.114	112	
100	C15	70.4	22.7	0.19	0.160	119	
100	C16	57.6	33.1	0.18	0.100	183	Pre-mature failure

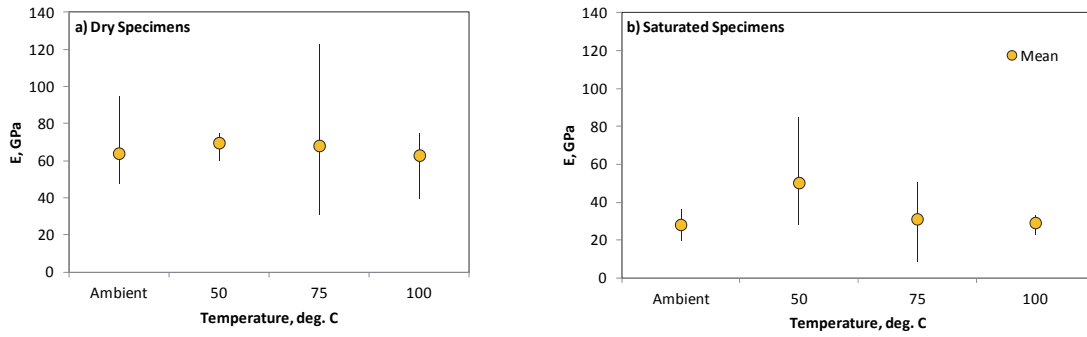


Figure 7: Comparison between dry and saturated Young's moduli of Cobourg Limestone

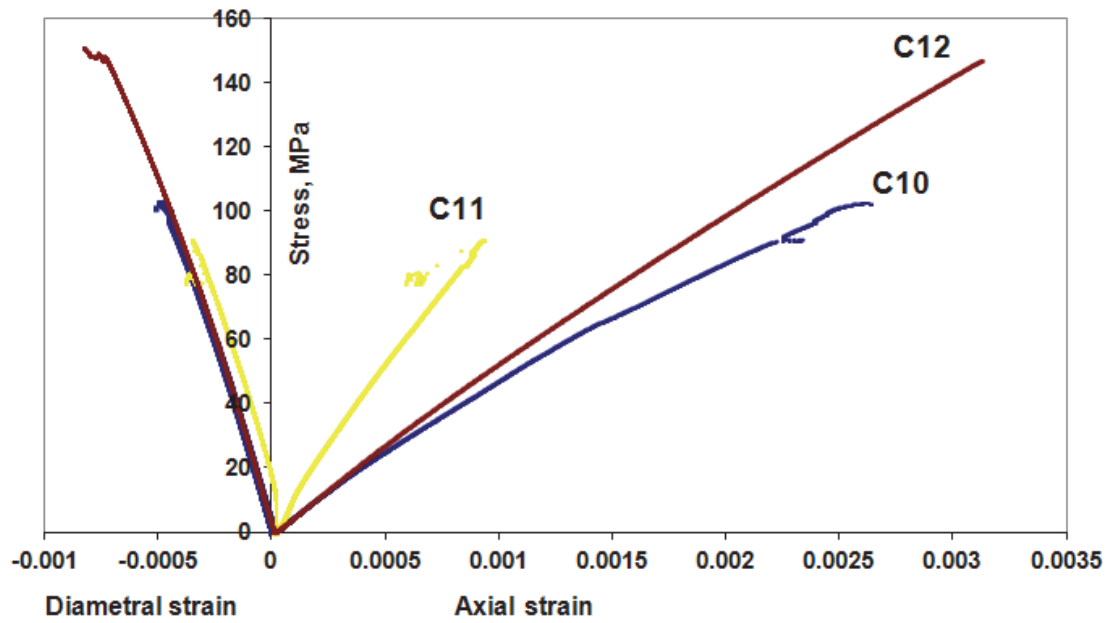


Figure 8: Stress-strain plots of dry Specimens C10, C11 and C12 at ambient temperature

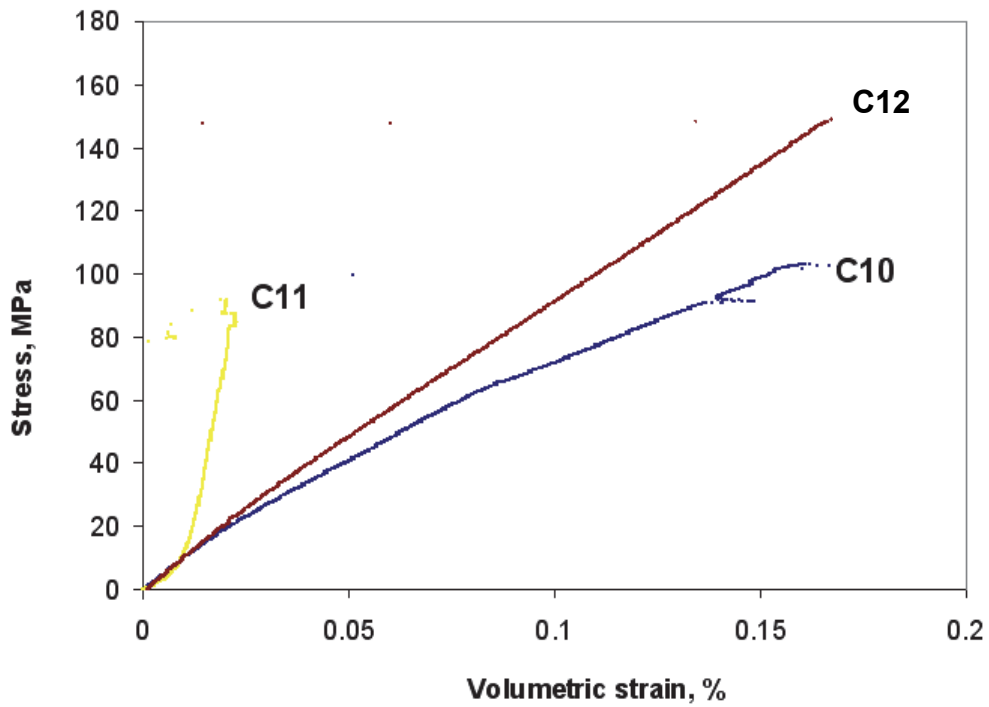


Figure 9: Volumetric strain of dry Specimens C10, C11 and C12 at ambient temperature

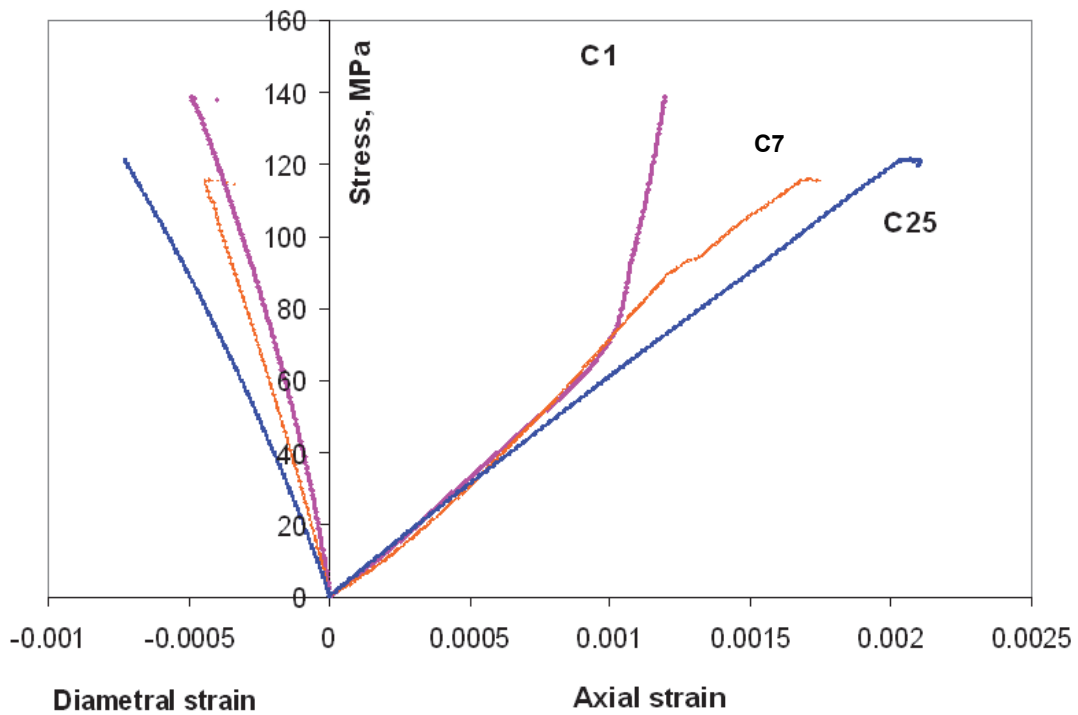


Figure 10: Stress-strain plots of dry Specimens C1, C7 and C25 thermally treated at 50°C

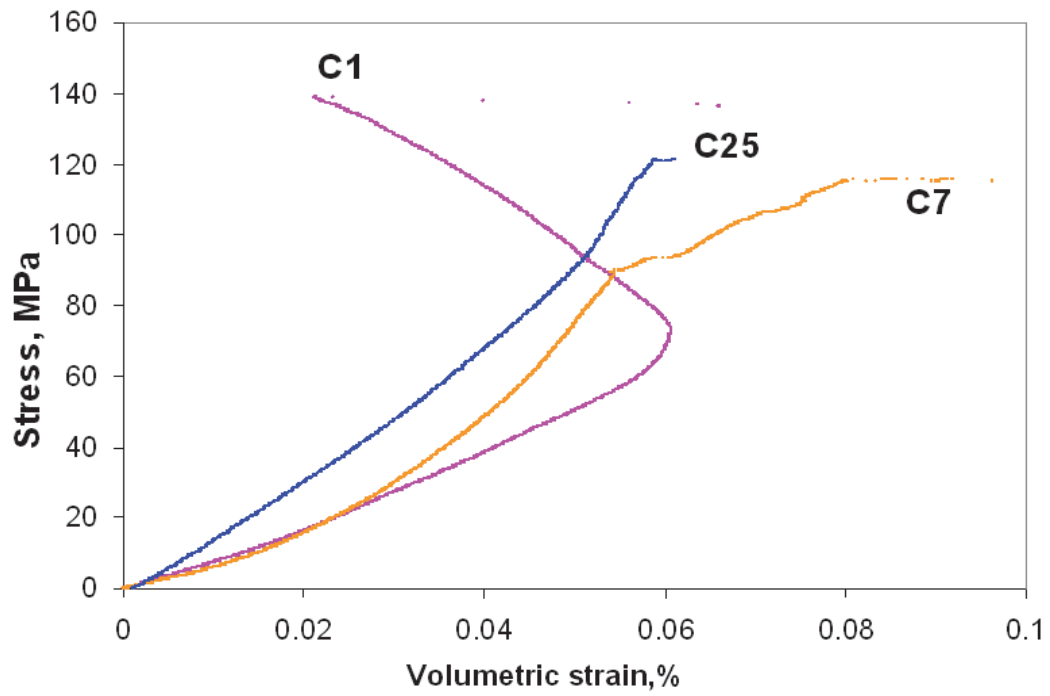


Figure 11: Volumetric strain of dry Specimens C1, C7 and C25 at 50°C

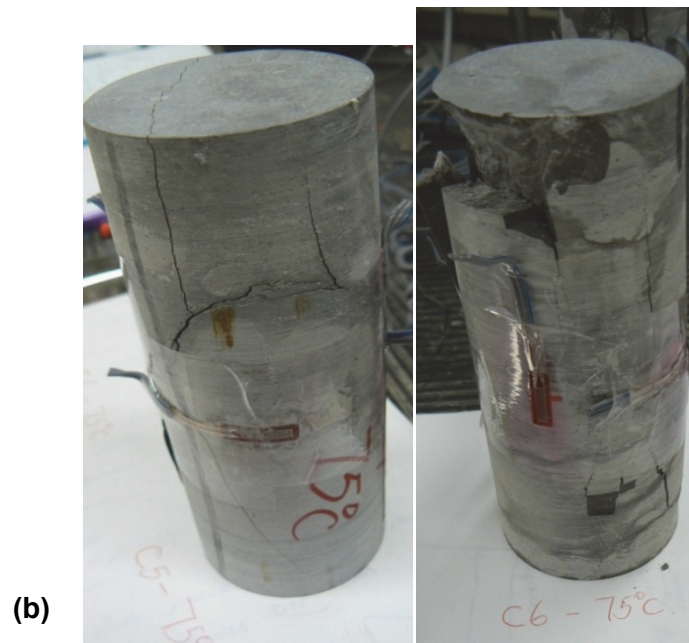
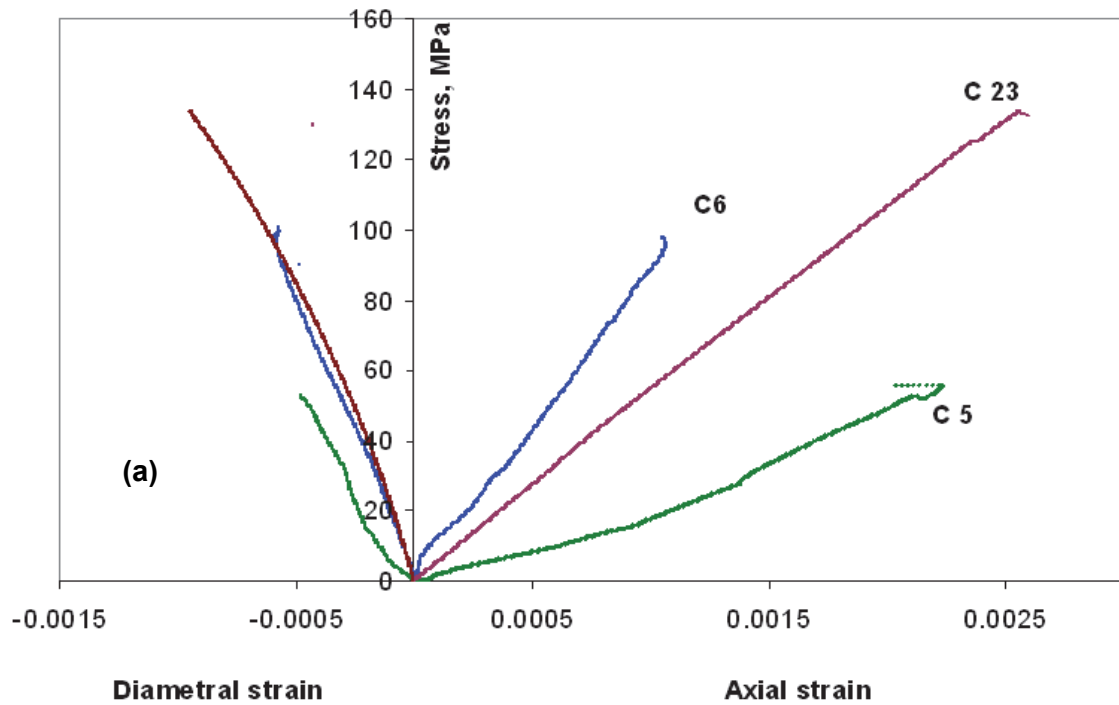


Figure 12: (a) Stress-strain Plots of dry Specimens C5, C6 and C23, thermal treatment at 75°C. (b) Specimen C6 experiences axial splitting failure whereas Specimen C5 shows pre-mature failure due to a pre-existing inclined feature

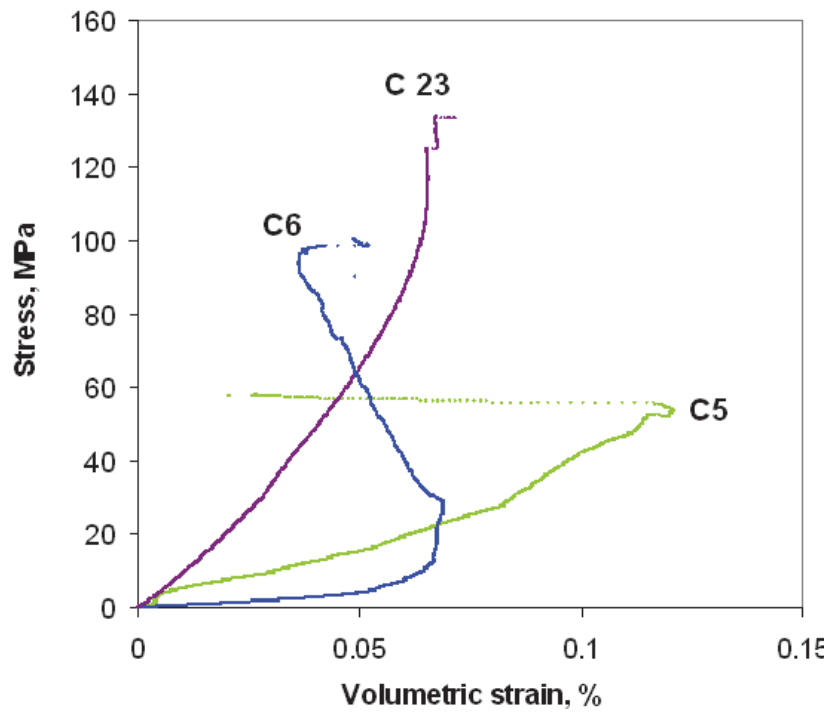


Figure 13: Volumetric strain of dry Specimens, C5, C6 and C23, thermally treated at 75°C

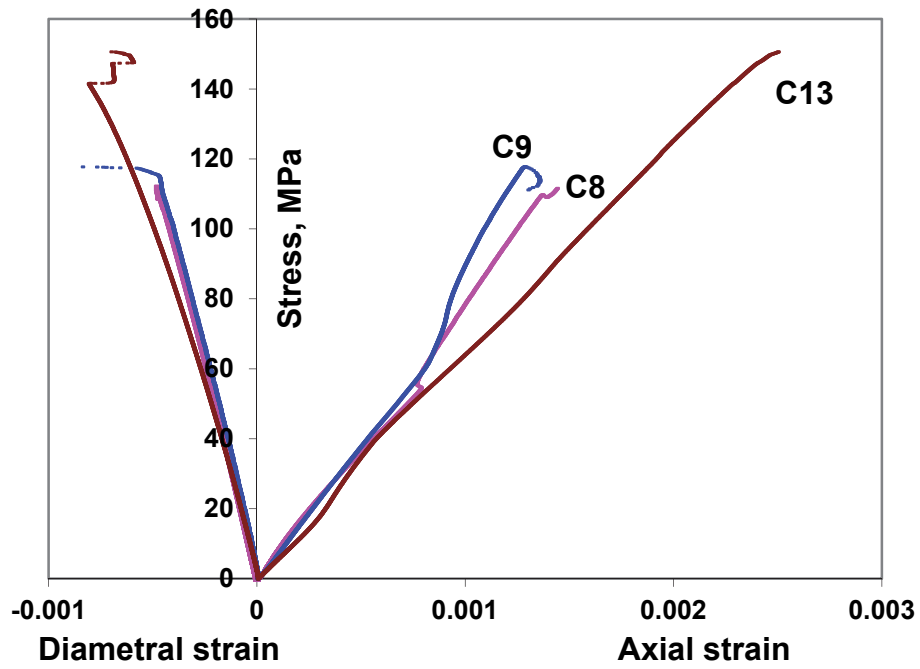


Figure 14: Stress-strain plots of dry Specimens, C8, C9 and C13 thermally treated at 100°C

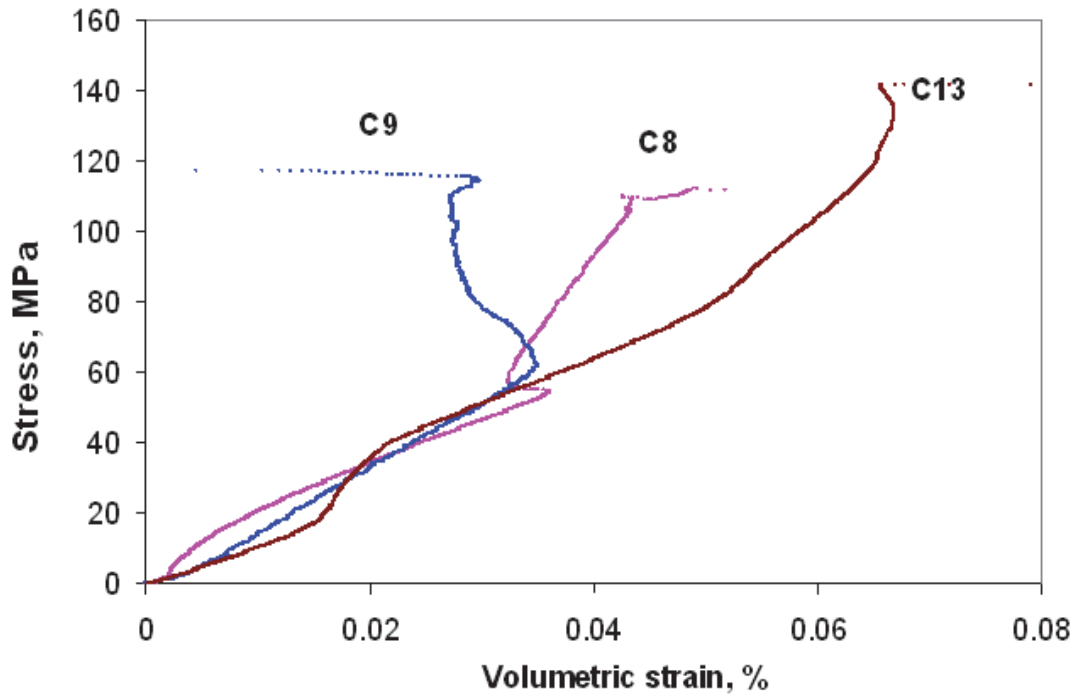


Figure 15: Volumetric strain of dry Specimens C8, C9 and C13, thermally treated at 100°C

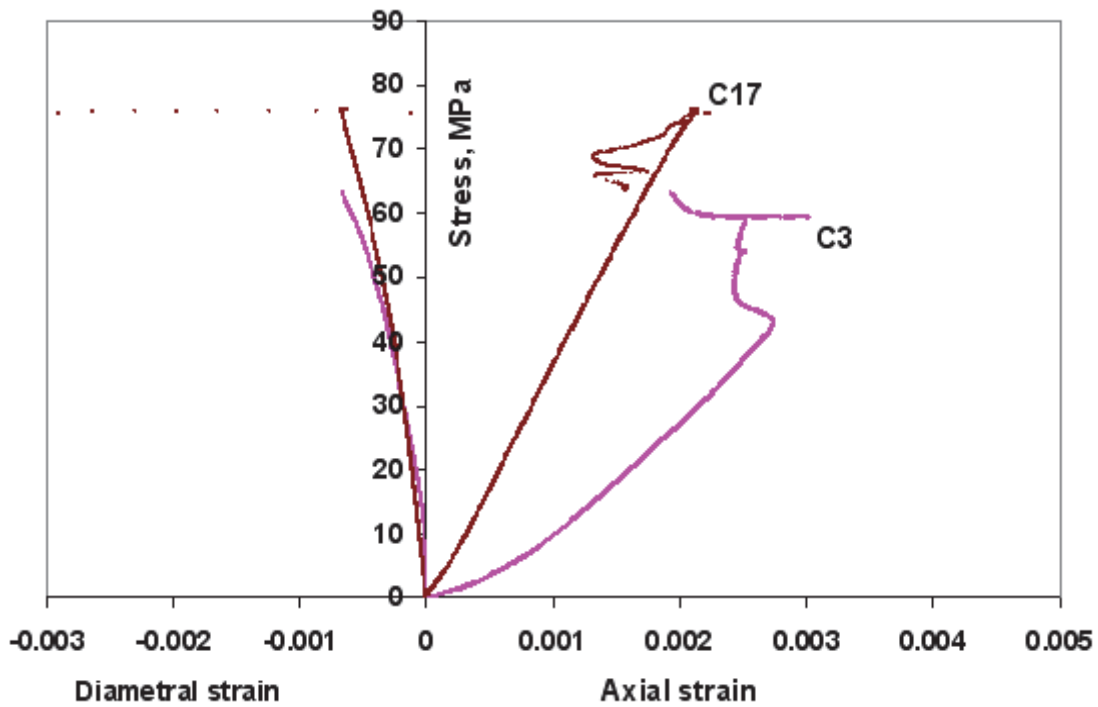


Figure 16: Stress-strain plots of saturated Specimens, C3 and C17 for ambient temperature

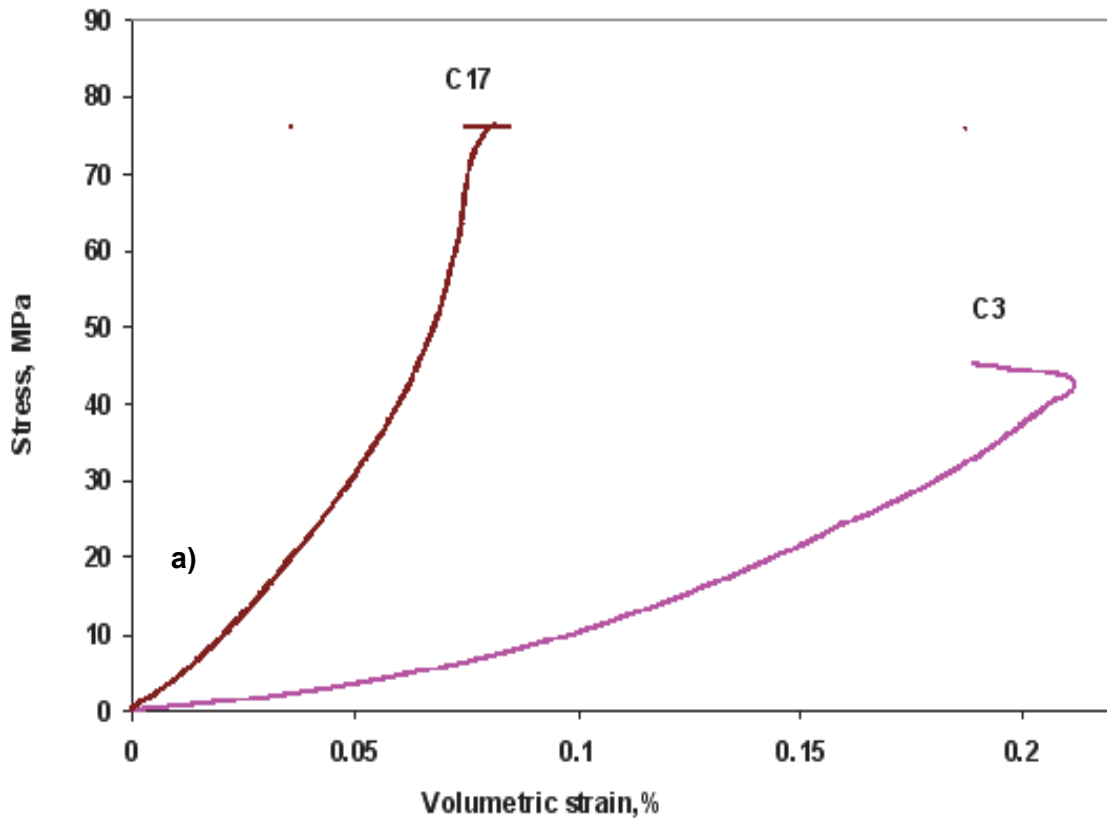


Figure 17: (a) Volumetric strain for saturated Specimens, C3 and C17, for ambient temperature and (b) a 75° inclined failure plane of Specimen C17

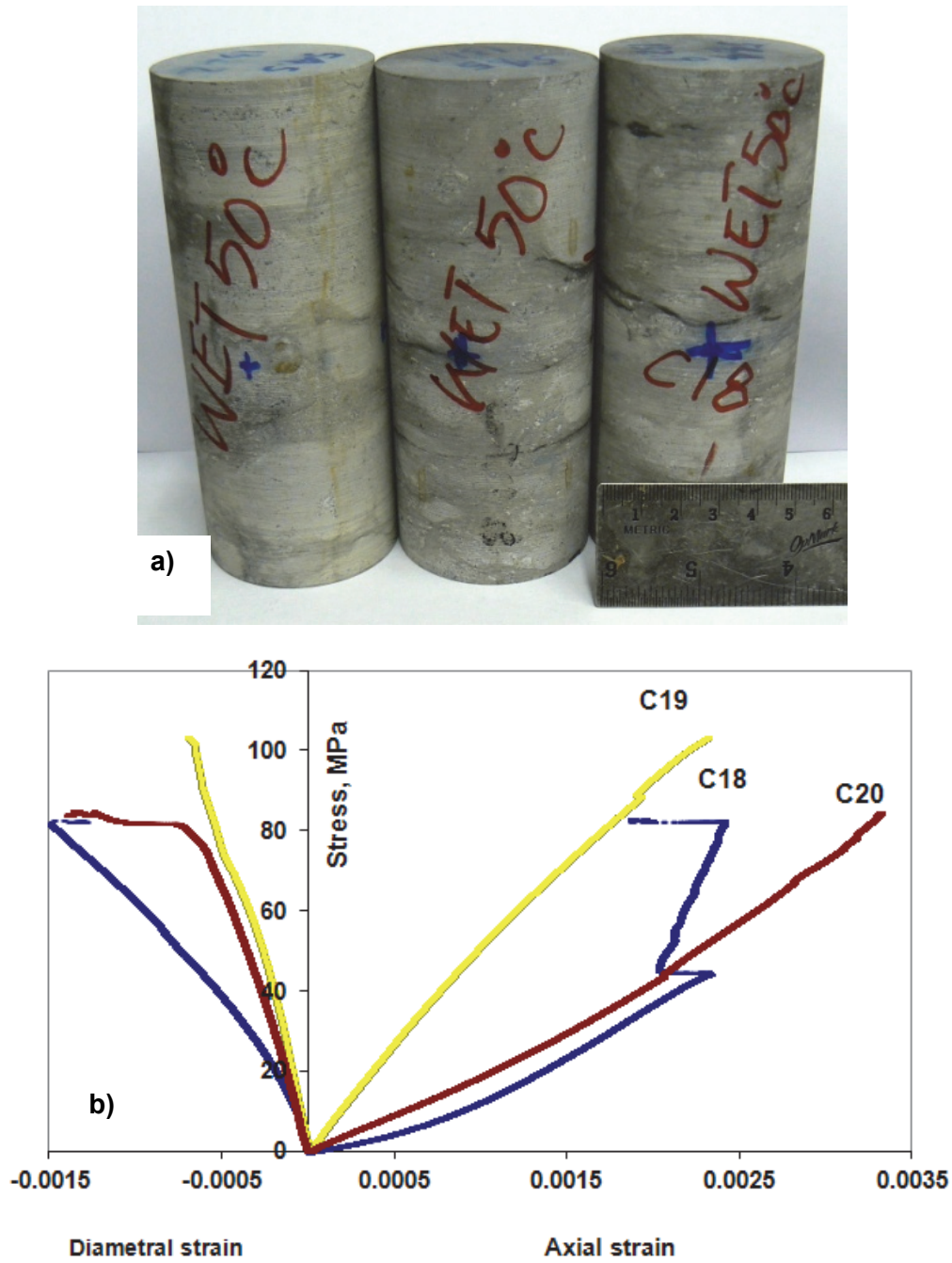


Figure 18: (a) A photo of saturated Specimens, C18, C19 and C20, thermally treated at 50°C prior to testing and (b) Stress-strain plots of the three saturated specimens

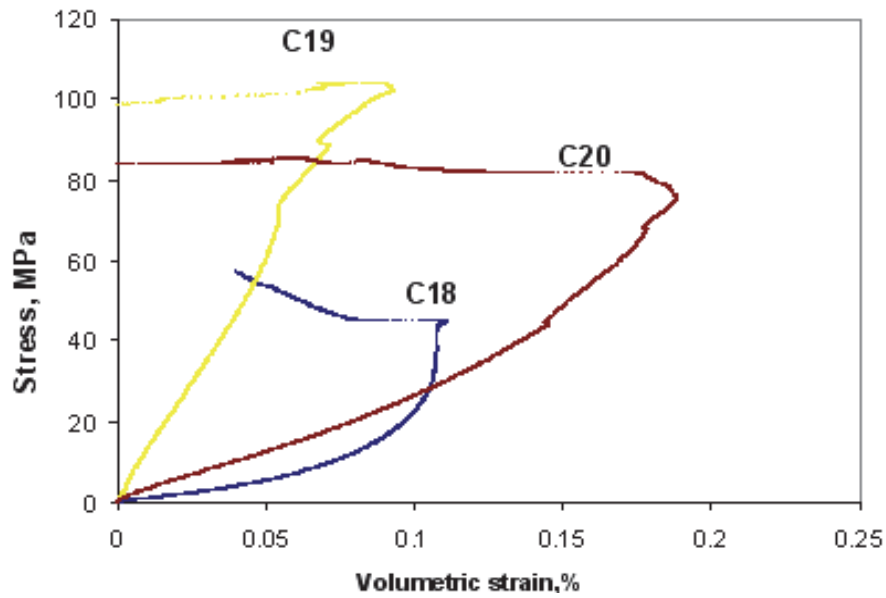


Figure 19: Volumetric strain of saturated Specimens C18, C19 and C20, thermally treated at 50°C.

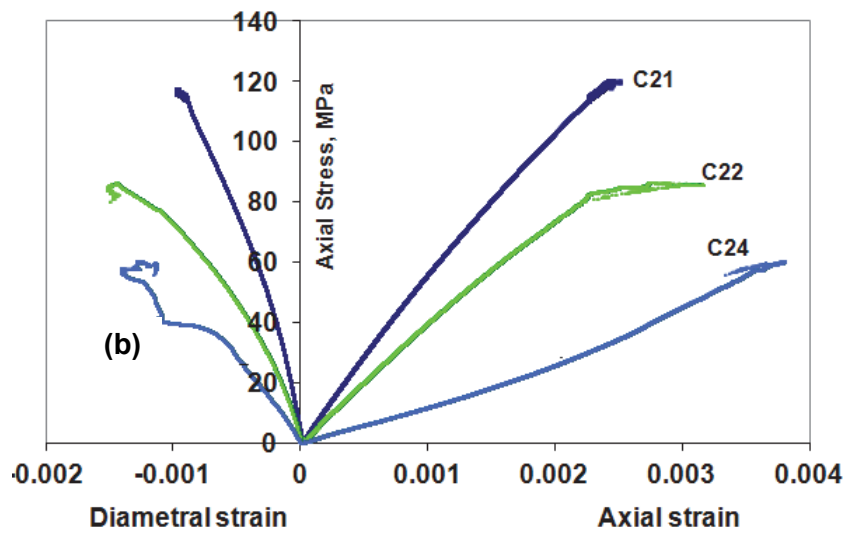
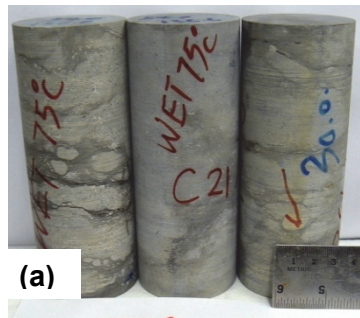


Figure 20: (a) A photo of saturated Specimens C21, C22 and C24, thermally treated at 75°C prior to Testing. (b) Stress-strain Plots of the three specimens

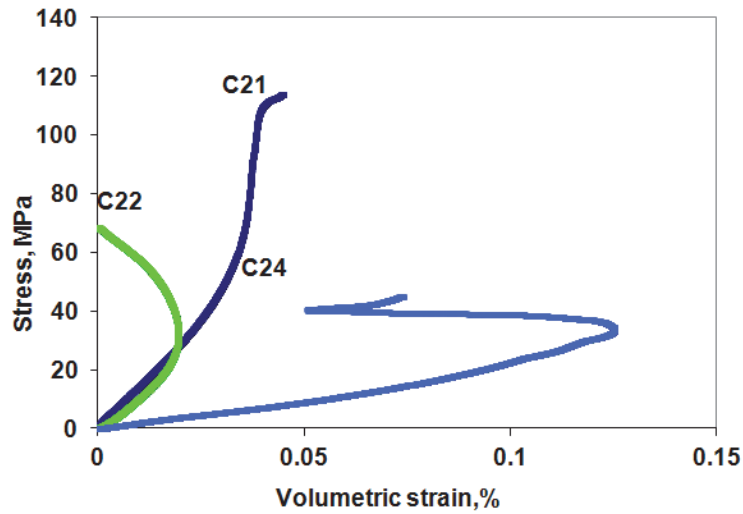
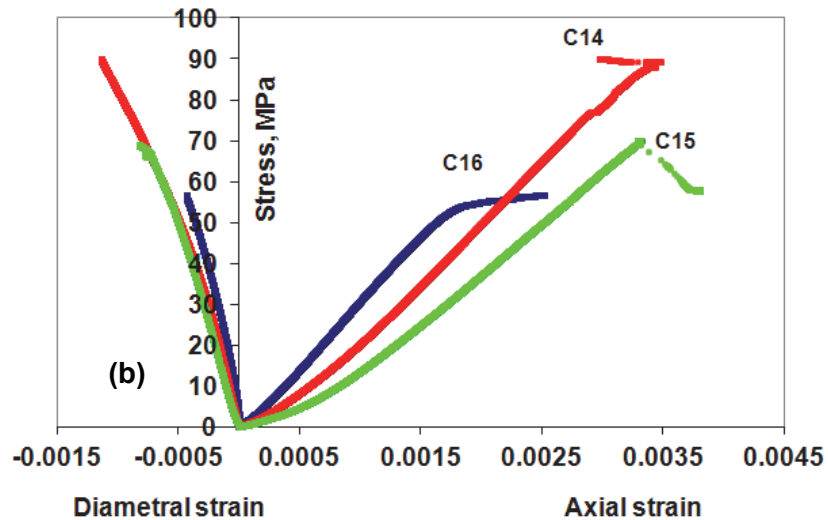


Figure 21: Volumetric strain of saturated Specimens C21, C22 and C24, thermally treated at 75°C



(a)



(b)

Figure 22: (a) A photo showing heterogeneous and anisotropic nature of Specimens C14, C15 and C16, thermally treated at 100°C and (b) Stress-strain plots of the three specimens

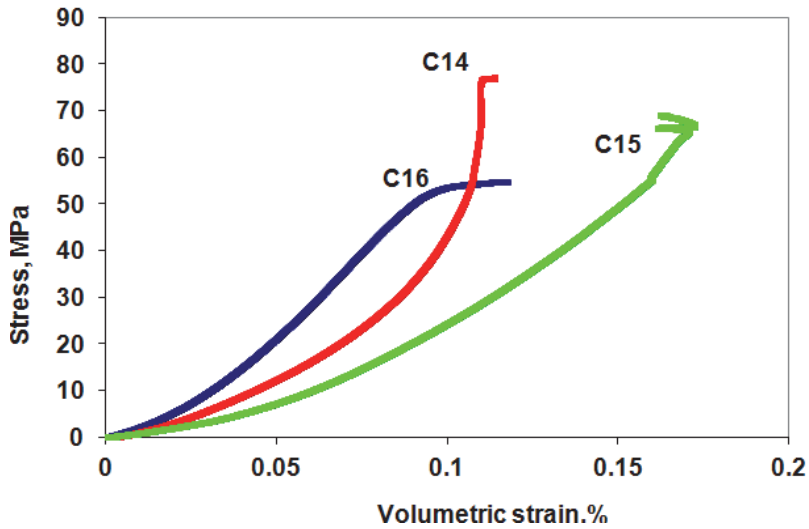


Figure 23: Volumetric strain of saturated Specimens C14, C15 and C16, thermally treated at 100°C.

2.3.3 Strength Anisotropy of Samples

The Cobourg limestone is characterized with shale/argillaceous interbeds of irregular width that at times make various angles with respect to the length of the specimens that were selected for uniaxial compressive strength determination. It was noted that these shaly partings do not systematically and repeatedly maintain a certain angle with the longer axis of the specimens (Figure 24). In this study, two specimens were found to have failed along such planes that randomly made various orientations ($\beta = 45$ and 75 degrees, Figure 24) with the main principal stress direction during uniaxial compressive testing. Figure 25 compares the orientations of the failure planes of these two specimens, which happened to have $\beta = 45$ and 75° . The third specimen in the figure has shaly partings horizontally bedded ($\beta = 90^\circ$, Figure 25) and is shown for reference purposes; the shale partings make a maximum orientation angle with the long axis of the specimen. A close look at the failure planes of these specimens shows the generation of wing cracks running parallel to the direction of loading or the direction of maximum principal stress. This graph shows that the specimen with $\beta = 45^\circ$ has the lowest UCS of 54 MPa. The UCS increases to 91 MPa, when the orientation changes to 90° .

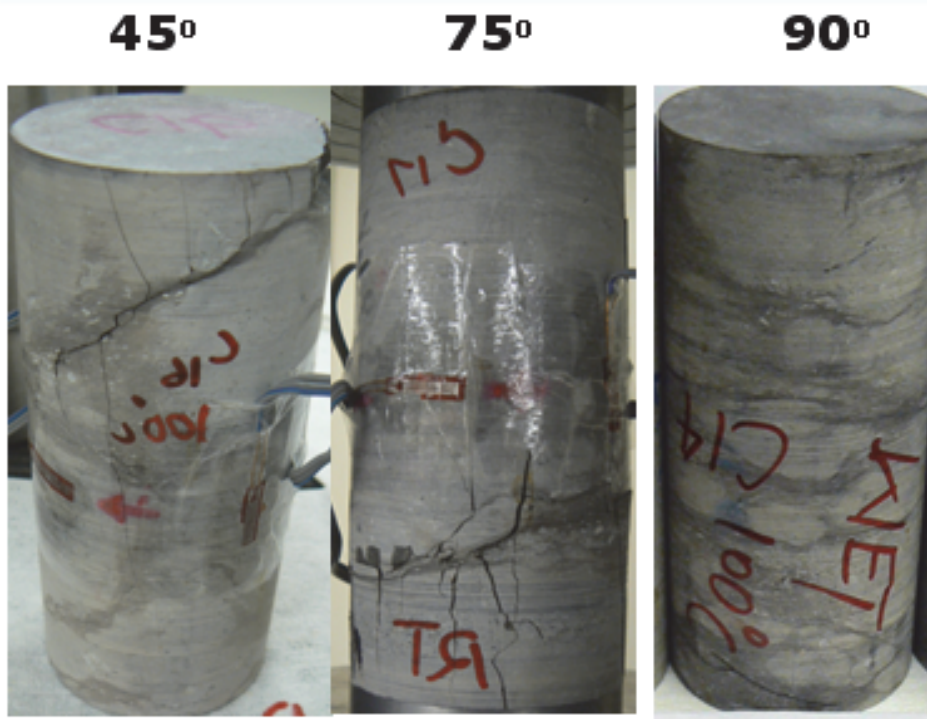


Figure 24: Cobourg specimens characterized with inclined features at different orientations (C16 and C17 – after tests and C14 – before test)

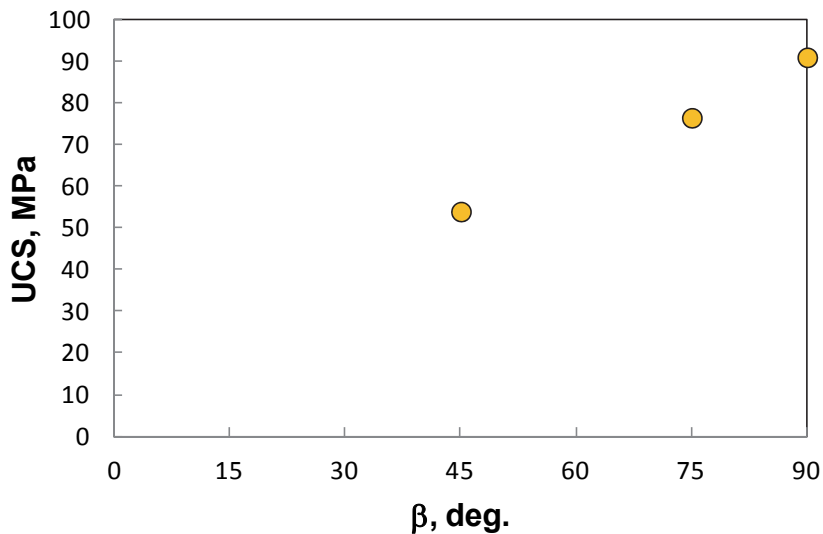


Figure 25: Variation of UCS with inclined feature orientation (β) in Cobourg specimens

2.3.4 Evolution of Seismic Velocity with Stress

In this section, the results of the evolution of seismic wave velocities, compression and shear wave velocity (V_P and V_S), as a function of hydrostatic stress increments up to 12.5 MPa is reported for three 37-mm-diameter specimens (S0, S2 and S3) of saturated Cobourg

specimens. Figures 26 and 27 show the seismic wave velocity hysteresis for S0 specimen. V_P and V_S both increase about 100 and 150 m/s respectively as hydrostatic stress is increased up to 12.5 MPa. During unloading, seismic wave velocities recorded a higher value compared to the loading path, indicating the poroelastic or viscoelastic responses of pore spaces in Cobourg limestone. The pore spaces do not quickly reopen during unloading and, as a result, wave velocities record a higher value than during loading.

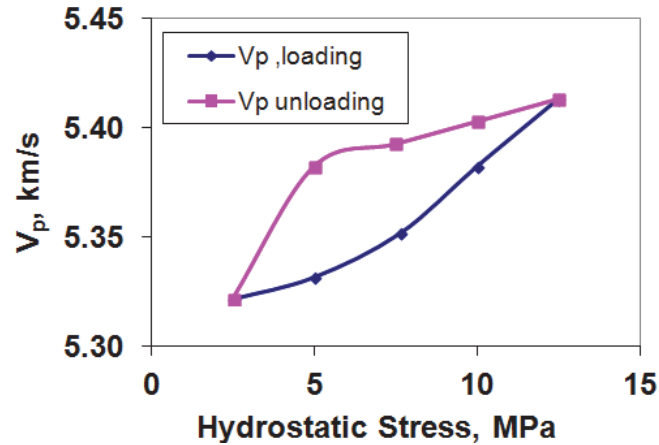


Figure 26: Variation of V_p , with hydrostatic stress during loading and unloading of Specimen S0

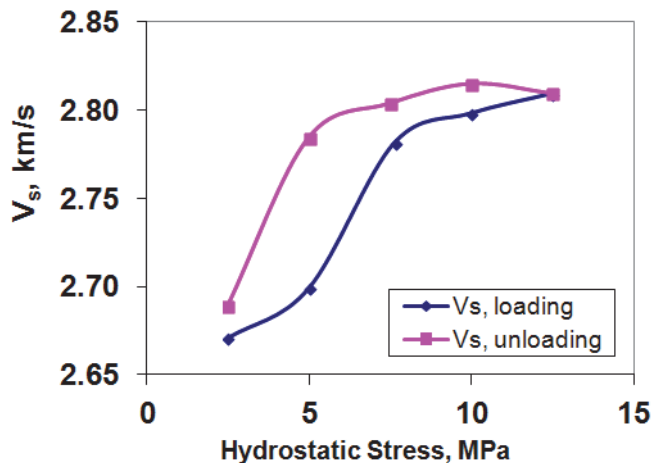


Figure 27: Variation of V_s , with hydrostatic stress during loading and unloading of Specimen S0

Figures 28 and 29 show the variation of seismic wave velocities for three saturated Cobourg specimens. In comparison, these specimens do not show identical responses to hydrostatic stress increments. This can be related to their heterogeneous nature from one specimen to another despite the fact that they were cored from the same sample block. S3 specimen does

not show much increase in V_P and V_S during loading whereas S0 in particular shows significant increase in velocities.

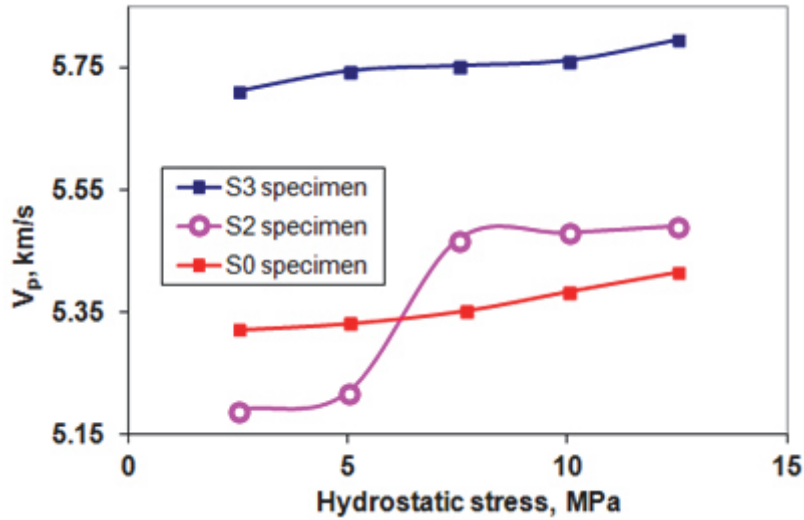


Figure 28: Evolution of V_P with hydrostatic stress increments up to 12.5 MPa of Specimens S0, S2 and S3

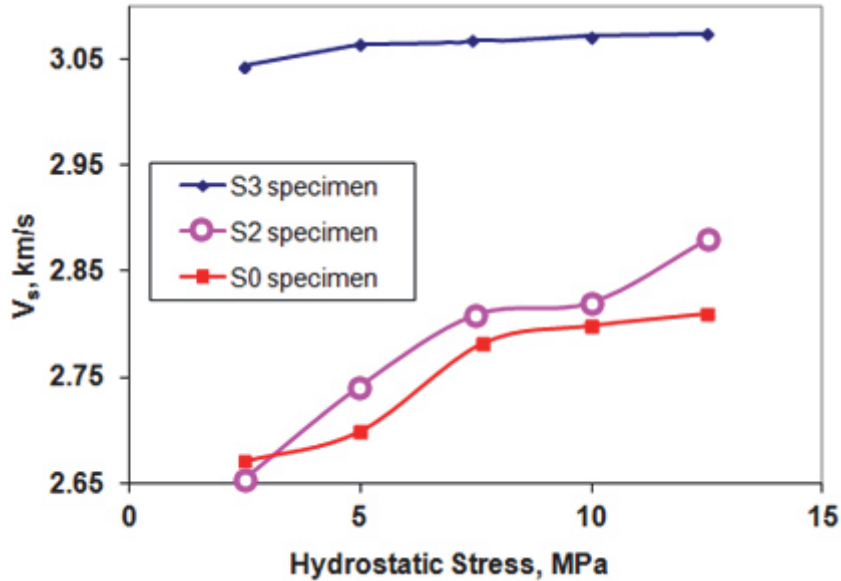


Figure 29: Evolution of V_S with Hydrostatic Stress Increments up to 12.5 MPa of Specimens S0, S2 and S3

2.3.5 Evolution of Seismic Velocity with Temperature

Figures 30 and 31 show the evolution of V_P and V_S of S0, S2 and S3 specimens with temperature increments while hydrostatic stress was kept constant at 12.5 MPa. The rates of decrease in seismic wave velocities for the three specimens are not the same, whereas all three specimens experience a more or less similar amount of seismic wave velocity reduction as a

function of temperature. Figure 33 shows the variation of dynamic Young's modulus (E_d) at various temperatures for these three specimens. All three specimens show an increase of dynamic Young's modulus (Equation 4) during hydrostatic load, up to 12.5 MPa during initial loading stage. In the second stage, when the hydrostatic stress is maintained at 12.5 MPa and temperature is raised systematically up to 100°C, the specimens' Young's modulus reduces as a result of thermal expansion as shown in Figure 33. The rate of increase and decrease in the specimen's Young's modulus is shown to be unequal, following the trend of V_p and V_s variation during various stages of loading and in-situ heating of these specimens.

$$E_d = \rho V_s^2 \frac{3V_p^2 - 4V_s^2}{V_p^2 - V_s^2} \quad (4)$$

where ρ is the density of the rock in g/cc, V_p is the compression velocity in km/s and V_s is the shear wave velocity in km/s.

2.3.6 Evolution of Permeability with Stress

The study of permeability was carried out on three 37 mm diameter samples of Cobourg limestone.

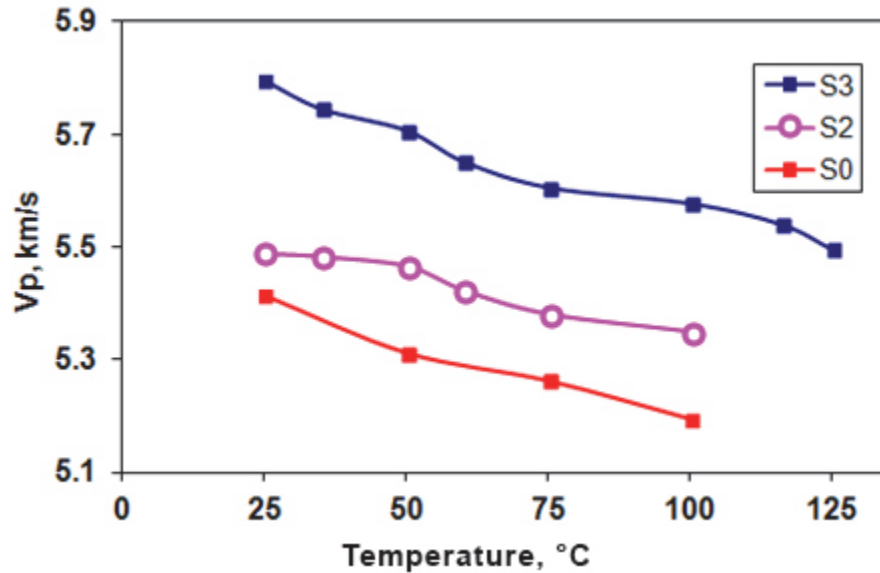


Figure 30: Evolution of V_p with Temperature Increments up to 125°C of Specimens S0, S2 and S3.

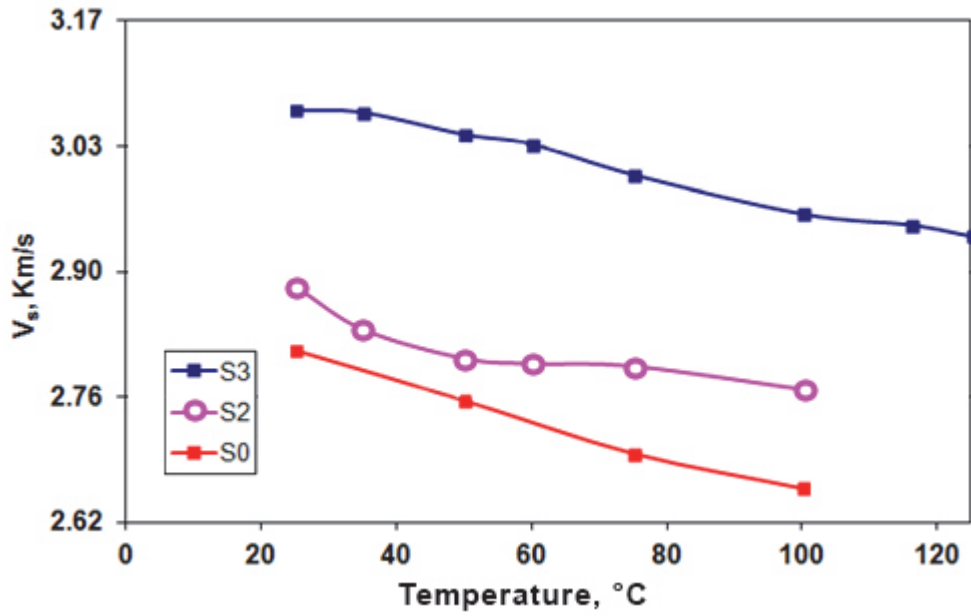


Figure 31: Evolution of V_s with hydrostatic stress increments up to 125°C of Specimens S0, S2 and S3

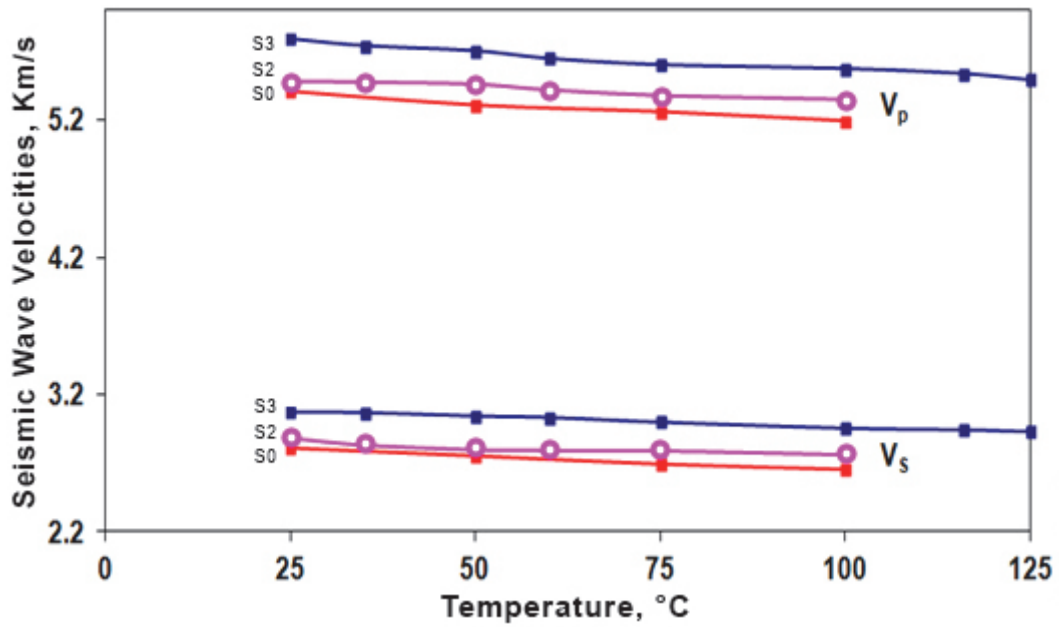


Figure 32: Decrease in elastic-wave velocities as temperature increase in Specimens S0, S2 and S3

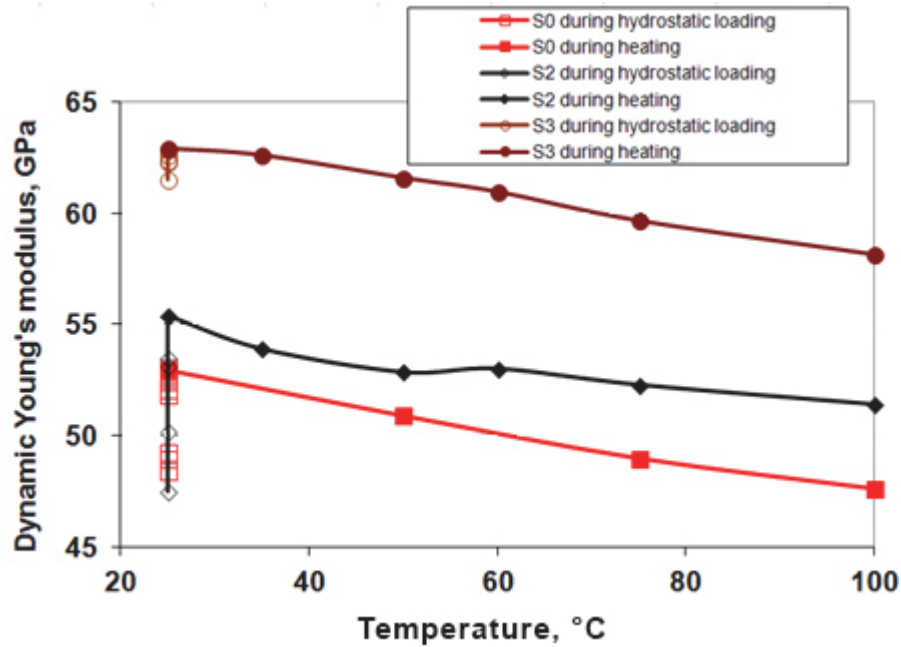


Figure 33: Variation of dynamic Young's modulus as a function of hydrostatic stress at a constant temperature up to 12.5 MPa and of temperature at constant stress up to 100°C

The pulse decay method was applied at each new hydrostatic stress increment up to 12.5 MPa. The first series of permeability measurements at various hydrostatic stress levels were performed at ambient temperature. Similar experiments were performed on all three specimens. Next, the same procedure of pulse decay method was applied at a constant hydrostatic stress of 12.5 MPa under various temperature increments up to 125°C. Measurements of permeability under ambient temperature were carried out as hydrostatic stress was kept at various constant levels (2.5, 5, 7.5, 10 and 12.5 MPa). The pulse decay method was implemented to calculate permeability using equations 2 and 3 shown in section 2.2. With this method, first the two ends of the specimen within the cell were connected to a quizix pump applying 1 MPa of pore pressure while hydrostatic stress was maintained at 2.5 MPa. At the effective stress of approximate 1.5 MPa, a pulse was introduced from the upstream side of the specimen towards the downstream side. Once the downstream and upstream reservoir pressure at the quizix pump level is maintained at approximate 1 MPa, the downstream valve is closed and the pore water pressure introduced by quizix pump connected to the top of the specimen is regulated at 1.5 MPa with the top valve still open. Once the pore water pressure at the quizix pump and the water pressure sensor close to the top of the specimen show the pressure reached 1.5 MPa, the top valve is closed. As a result, a hydraulic pulse is now generated from the upstream side, into the specimen towards the downstream side. Its decay is measured with time. Similar procedure is repeated for higher constant hydrostatic stresses up to 12.5 MPa. Figure 34 shows one such decay with time, while Figure 35 shows the response of the Cobourg limestone's permeability as a function of hydrostatic stresses during loading and unloading procedures of the same specimen. Permeability was found to decrease during loading by an order of magnitude. Permeability was not recovered to its original level during unloading steps, reflecting the viscoelastic nature of pores and their lack of response to unloading stages.

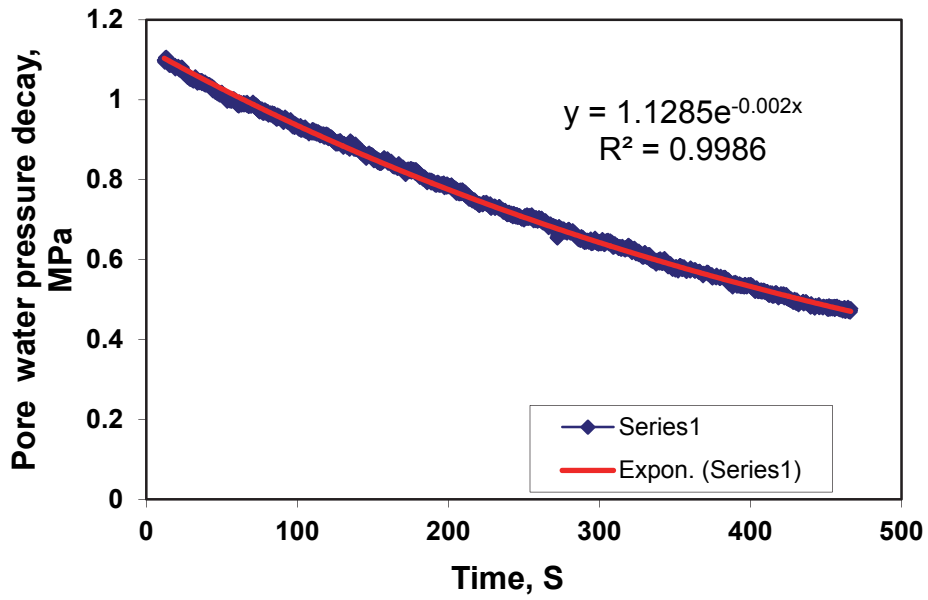


Figure 34: Decay of pore pressure with time in a typical pulse decay measurement used for permeability determination

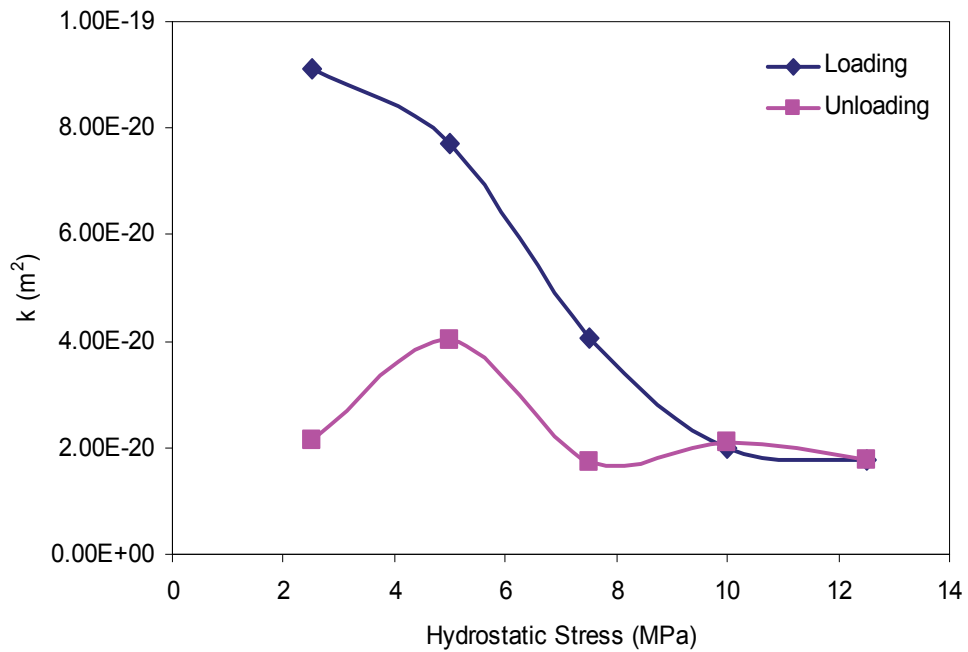


Figure 35: Permeability decreases with increase in hydrostatic pressure, indicating the closure of well-connected pores

2.3.7 Evolution of Permeability with Temperature

Using the pulse decay method, the permeability of the Cobourg limestone was measured under constant hydrostatic stress of about 12.5 MPa (simulated 500 m depth) at various increments of 50, 75, 100 and 125°C. At each in-situ heating stage, enough time was given for the system to achieve temperature equilibrium on activation of the automatic temperature control implemented through the software. Next, the two ends of the specimens within the cell were connected to the quizix pump, which applied 4 to 5 MPa of pore pressure before introducing a pulse into the specimen which was hydrostatically stressed at 12.5 MPa. Therefore, a differential stress of 7 to 8 MPa was maintained during the permeability measurement of the limestone under in-situ elevated temperature up to 125°C. Figures 36 and 37 show the variation of permeability as a function of temperature for S4 and S2 specimens.

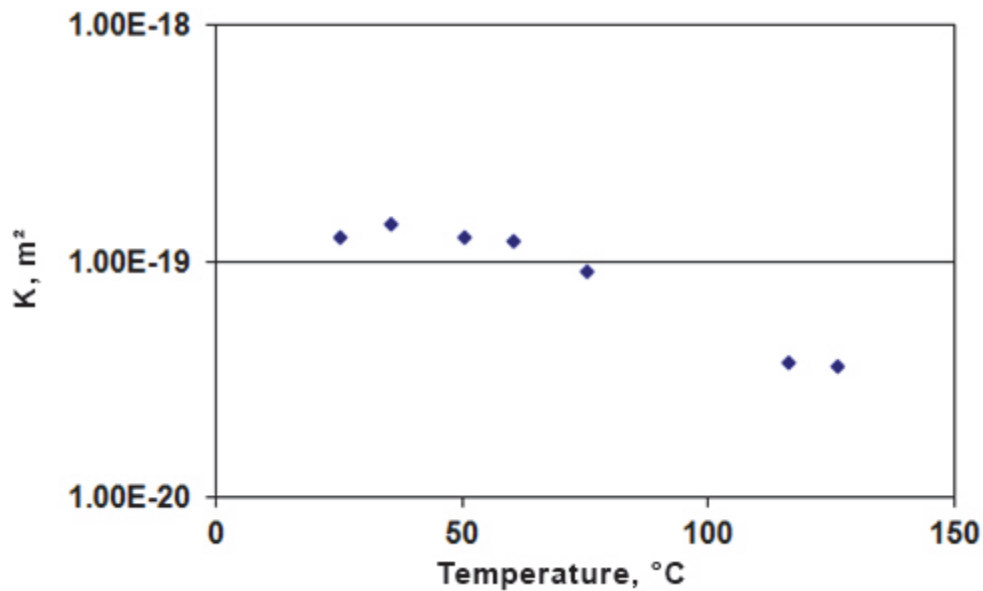


Figure 36: Evolution of permeability with temperature up to 125°C for Specimen S4

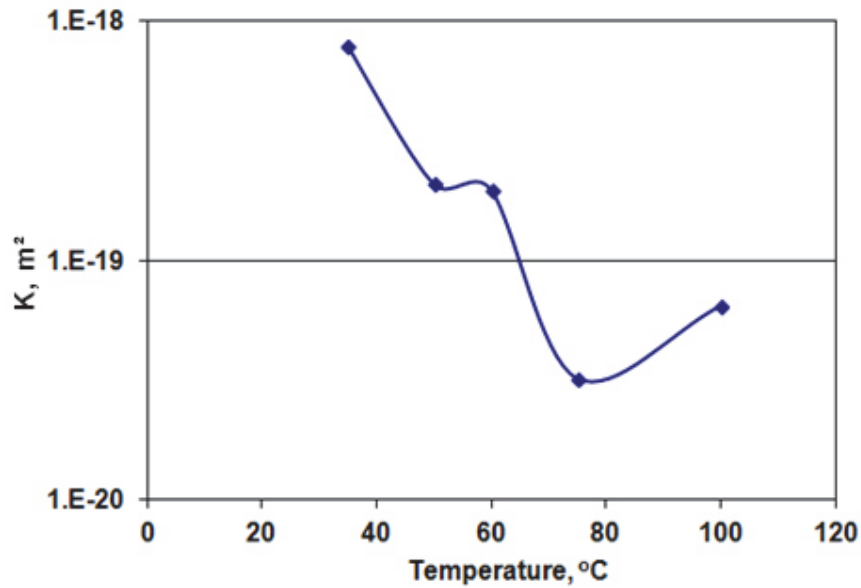


Figure 37: Evolution of permeability during temperature increase at a constant stress Specimen S2

2.3.8 Effect of Thermal Expansion on Test Results

Since the coefficient of thermal expansion of liquid is much higher than that of solid, the presence of water in porous rocks can have a mechanical effect on the solid matrix with increases in temperature. Figure 38 shows that water expands non-linearly with temperature between room temperature and 90°C.

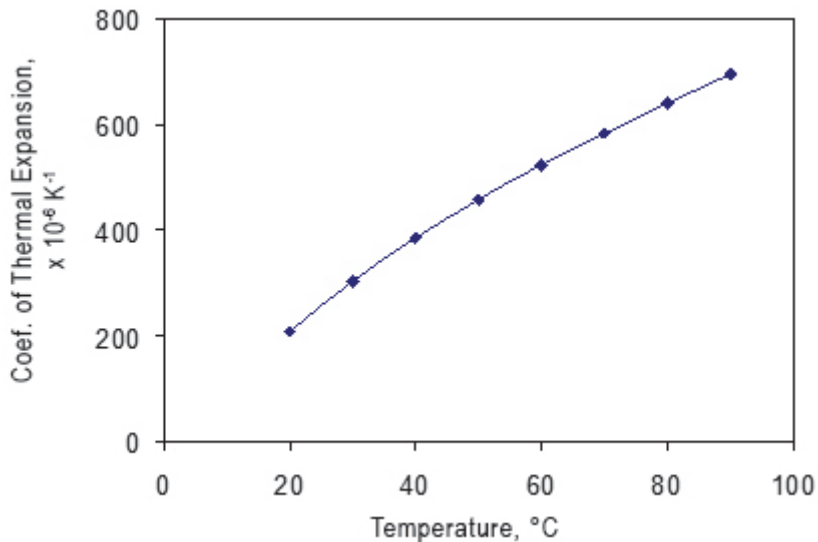


Figure 38: The evolution of the coefficient of thermal expansion of water with increase in temperature (Horseman and McEwen, 1996)

Seismic wave velocities were measured at each hydrostatic stress increment and under constant hydrostatic stress (12.5 MPa) at various temperature levels from ambient up to 125°C. Figures 39 and 40 show the evolution of V_p and V_s for the aforementioned situations for S3 specimen. At ambient temperature, V_p was found to increase from 5.71 km/s to 5.8 km/s and V_s increased from 3.05 to 3.5 km/s when hydrostatic stress was raised from 2.5 MPa to 12.5 MPa. This increase is due to the closure of micro flaws and pores, which makes the sample stiffer. During heating phases, V_p was found to decrease from 5.8 to 5.5 km/s whereas V_s decreased from 3.5 to 2.94 km/s. During hydrostatic loading, dynamic Young's modulus increased from 61 GPa to 63 GPa for S3, whereas dynamic Young's modulus for this specimen was found to decrease from 63 to 58 GPa as a function of temperature increase from ambient to 125°C. Similar trends were observed for S0 and S2 specimens. Figure 41 shows the amount of expansion and seismic wave velocity reduction as a result of the specimen's thermal expansion with temperature increments combined. The S3 specimen expands approximate 0.2 mm over its original length of 79.49 mm. This is to emphasize that the thermal expansion of the steel loading platens have a coefficient of thermal expansion coefficient of 2.4×10^{-4} . Based on the total length of platens (20cm) being exposed to heating, the net amount of both platens' expansion is 0.05438 mm of the total expansion of 0.2 mm registered by axial LVDTs. Based on this calculation, the true or net expansion of the specimen is 0.15 mm over its original length of 79.49 mm.

Permeability of Cobourg limestone as a function of temperature increments up to 125°C and the thermal expansion of the specimen are shown in Figure 42. The specimen experiences the highest level of expansion above 50°C. This is reflected in the permeability values, which show a sudden decrease from 1×10^{-19} to 5×10^{-20} m². This decrease of permeability becomes more evident as higher temperatures were approached, due to further expansion of the sample (0.2 mm for a 100°C increase) and the decrease in viscosity.

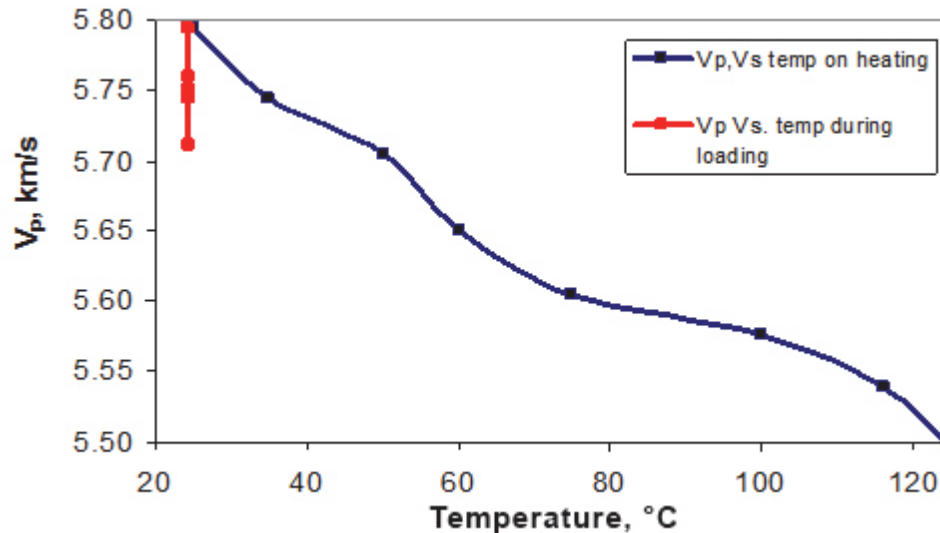


Figure 39: Evolution of V_p under a constant 12.5 MPa hydrostatic stress under ambient temperature (the red line), and during temperature increase (the blue line) of Specimen S3

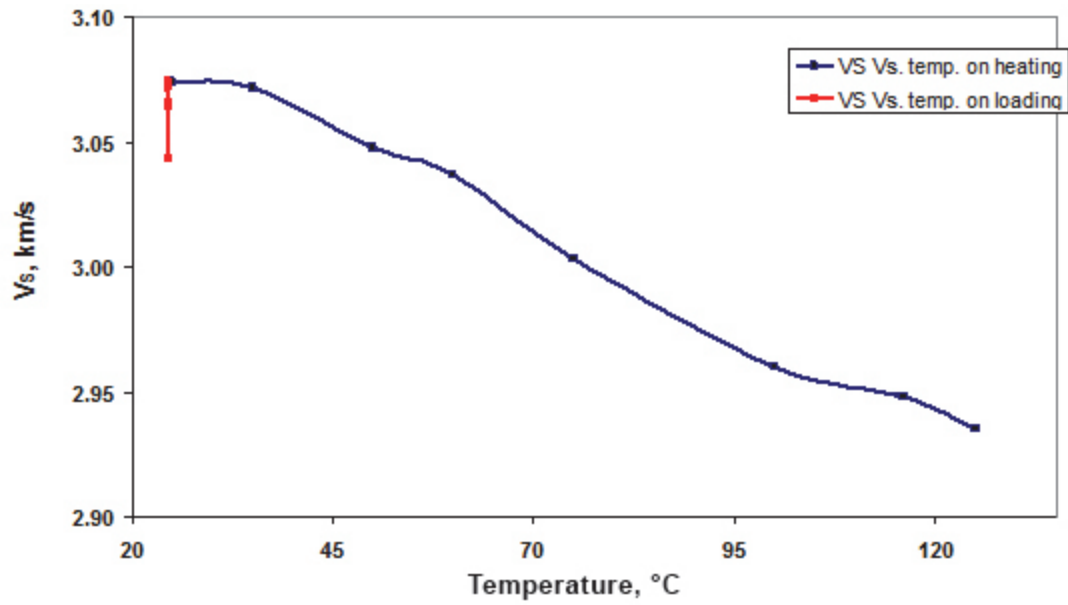


Figure 40: Evolution of V_s under a constant 12.5 MPa under ambient temperature (the red line), and during temperature increase (the blue line) of Specimen S3

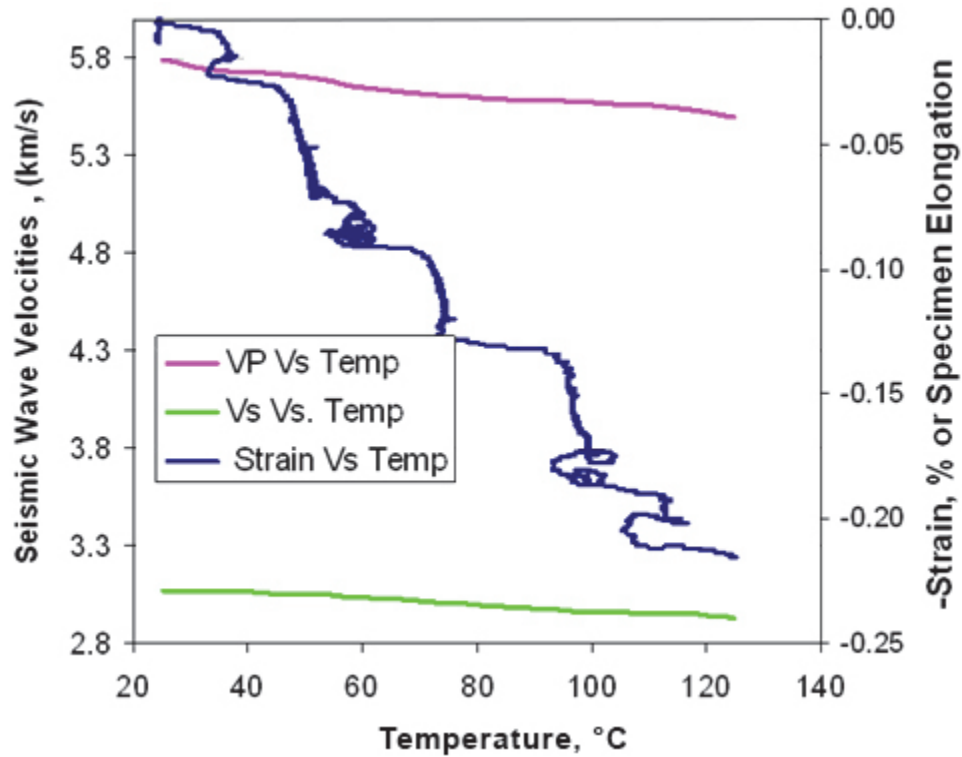


Figure 41: Variation of axial strain (%) and seismic wave velocities with temperature, Specimen S3

Overall, the permeability for the S3 specimen changes from $2 \times 10^{-19} \text{ m}^2$ at ambient temperature to $2.5 \times 10^{-20} \text{ m}^2$. It seems that the expansion of calcite and other clay minerals in Cobourg limestone are responsible for reducing pore interconnectivity resulting in an order of magnitude decrease in matrix permeability. This finding is in agreement with the experimental study results of Zhang et al. (2007). Figure 43 shows the same variation with strain converted to percentage. There exists a trend between the thermal expansion of the specimen and its permeability reduction as a function of temperature increase. Figure 44 shows overall strength, deformational, seismic and permeability evolution during loading of Cobourg limestone hydrostatically up to 12.5 MPa of stress at ambient temperature and its further responses to temperature increase under constant hydrostatic stresses.

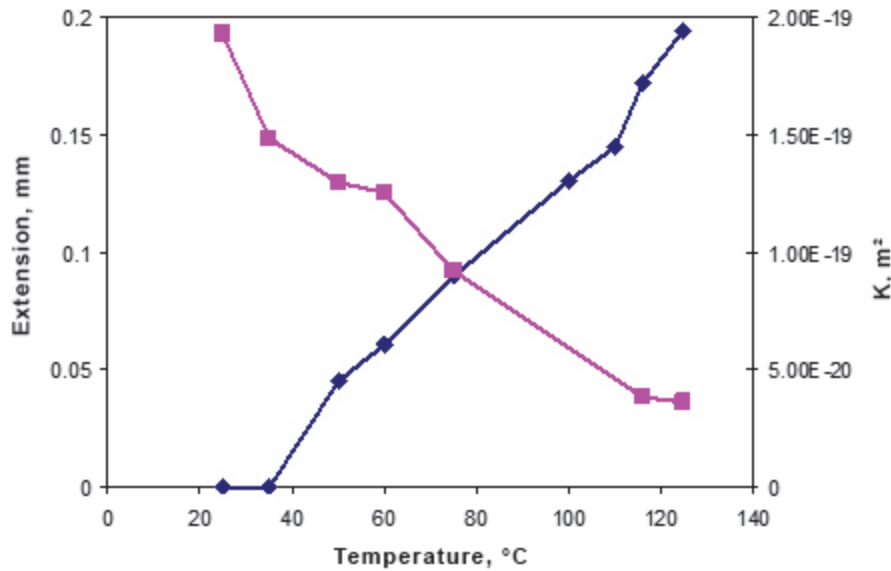


Figure 42: Axial elongation (blue) due to sample expansion and permeability (pink) reduction with temperature in Specimen S3

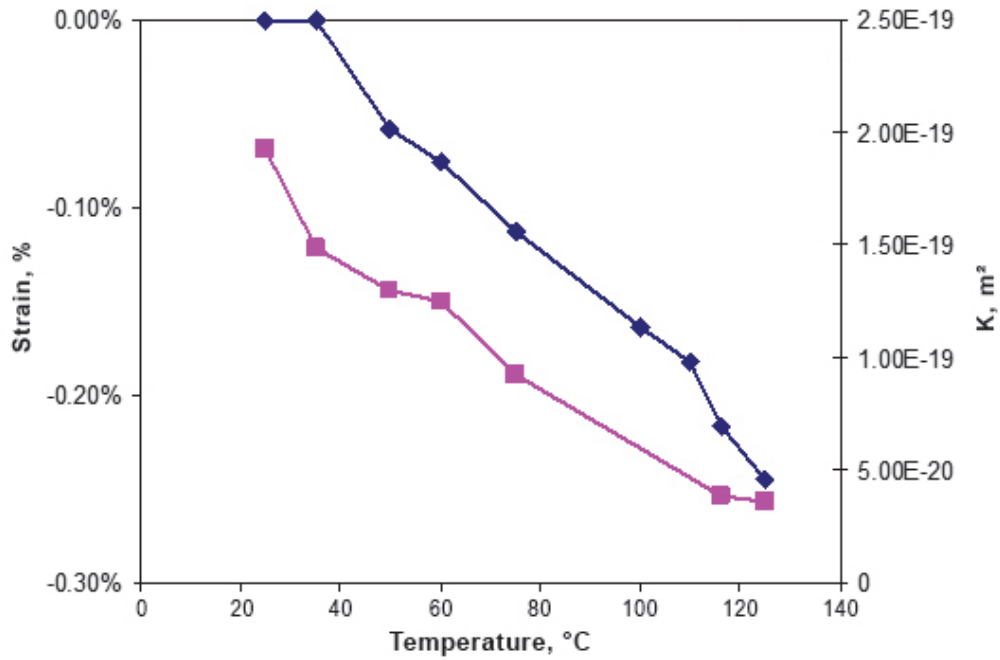


Figure 43: Axial strain (blue) decrease and permeability (pink) decrease with temperature in Specimen S3

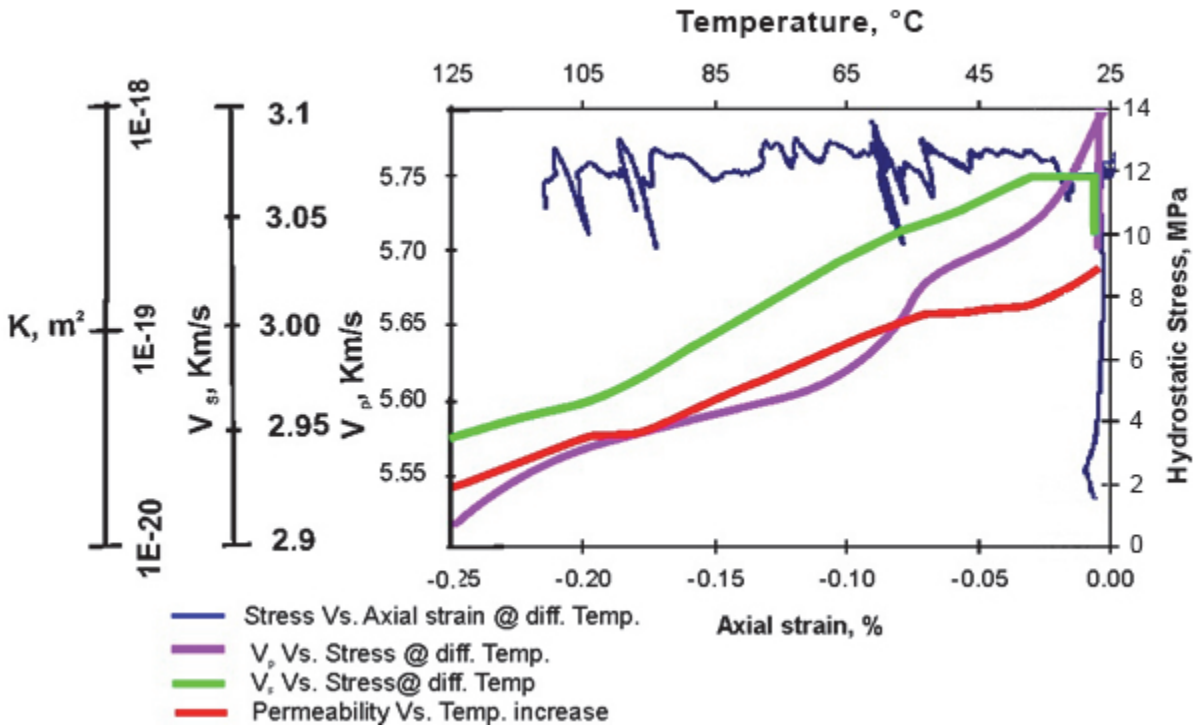


Figure 44: Variation of seismic wave velocities, permeability, axial strain and hydrostatic stress with temperature for Cobourg limestone

2.4 DISCUSSION OF PHASE 1 RESULTS

The Phase 1 experimental investigation consists of three groups of experiments. The first group of experiments is on physical property measurements, using dry and saturated samples. The second includes uniaxial compressive strength tests on dry and saturated samples, with and without thermal treatment. The samples were tested at room temperature and at 50°C, 75°C and 100°C. The last group of experiments were carried out to measure the ultrasonic wave velocity, axial strain and permeability changes at ambient and elevated temperatures for confining hydrostatic loads from 2.5 up to 12.5 MPa.

The results from physical properties determination indicate that Cobourg limestone has a porosity of 1%, dry and saturated densities of 2.64 and 2.66 g/cc. The rock shows a fair amount of heterogeneity in terms of its texture. The uniaxial compression tests suggest that the Cobourg limestone is fairly strong, with an average uniaxial compressive strength (UCS) of 121 MPa and a standard deviation of 20 MPa for dry samples. Average saturated UCS for this rock is 83 MPa with standard deviation of 18 MPa. The average Young's modulus for a dry specimen is 67 GPa with a standard deviation of 24 GPa. Saturated specimens show the average Young's modulus of 37 GPa with a standard deviation of 18 GPa. Based on the test results, saturation lowers the range of variation of UCS and Young's modulus values in the specimens. The effect of pre-heating up to 100°C does not appear to have affected the strength and deformational properties of the samples in comparison to untreated specimens. The effect of pre-heating on the properties could be insignificant and likely be obscured due to high variability of the material.

The Cobourg limestone shows a decrease in permeability up to an order of magnitude with an increase in hydrostatic stresses (up to 12.5 MPa) on the three specimens tested. Temperature increment in the short-term tests under constant hydrostatic stress of 12.5 MPa and an effective stress ranging 7 to 8 MPa caused a thermal expansion of 0.2 mm in the limestone. It is important to mention that the effect of thermal expansion of loading platens (hardened steel) due to heating up to 125°C was found to cause an elongation of 0.054 mm out of the total expansion of 0.2 mm which was registered by axial LVDTs in the triaxial cell. Therefore, a negative axial strain of 0.2% is due to net specimen elongation. Specimen expansion or elongation reduces the specimen stiffness reflecting the reduction of seismic wave velocities and dynamic Young's modulus. Reduction of the dynamic modulus indicates that micro-cracking or expansions of pore spaces take place with temperature increments.

The permeability of the Cobourg limestone was found to be reduced by an order of magnitude due to the thermal expansion of carbonaceous minerals and the reduction of interconnected pore space. Cooper and Simmons (1977) found that the length of a rock sample, measured at room temperature, was larger after the thermal treatment than before. These mechanisms explain the behaviour of permeability and porosity against temperature. In the low temperature range, mineral expansion is only active: minerals expand towards the porous spaces. As a result, the apertures of the pre-existing cracks or interconnected pore spaces are clogged and, consequently, permeability and porosity decrease.

3. THM PROPERTIES OF COBOURG LIMESTONE: PHASE 2

3.1 INTRODUCTION

This chapter of the experimental work presents laboratory results from Phase 2 of the study to investigate coupled thermo-hydro-mechanical (THM) effects of Cobourg limestone under uniaxial and triaxial conditions. Samples of the limestone used in the experiments were retrieved at the St. Mary's cement's quarry in Bowmansville, Ontario. Twenty centimetre (20 cm) diameter specimens from the quarry were sub-cored into 50 mm diameter samples (Figure 45). Specimens were prepared according to ISRM (1977). Based on Phase 1 results, the Phase 2 testing plan was developed and is shown in Table 5 detailing the experimental investigations on freshly drilled Cobourg limestone samples.



Figure 45: St. Mary's cement's quarry in Bowmansville and cored samples

Table 5: Summary of Testing in Phase 2

Experiment	No. of Test Total	Room Temp.	50°C	100°C	150°C
Uniaxial Compression Test	12	4	3	3	3
Triaxial Compressive Strength Test	8	2	2	2	2
Uniaxial Compressive Strength Test with Thermal Treated Specimen	12	3	3	3	3
Triaxial Compression Test in Geophysical Imaging Cell	8	2	2	2	2

3.2 EXPERIMENTAL METHODS

3.2.1 Physical Properties Measurement

The sample preparation and the physical property measurements were determined using the ISRM (1981); this included the water saturation porosity technique. Dry and saturated weights of a number of representative samples from the UCS samples (ISRM 1977) and nine triaxial compressive strength specimens were measured for physical properties. First, the room temperature weight of all samples was measured. Then, the samples were saturated under vacuum for at least for two weeks (to ensure full saturation), and then fully saturated weights were taken. The difference between the dry and saturated weights of the samples was used to calculate the effective porosity of the samples. The porosities of the samples were calculated using equation (1) and ranged from 0.53% to 0.86%. Based on the same approach, dry density, saturated density and void ratio of the specimens were measured (Table 6).

3.2.2 Permeability Measurement

Cores with an approximate length of 125 mm and a diameter of 50 mm were tested for permeability evaluation within a geophysical Hoek type imaging cell during triaxial compressive strength tests. First, permeability of the limestone samples was measured as a function of hydrostatic stress of 12.5 MPa and at room temperature of about 25°C. A transient method (pulse decay method) suggested by Brace et al. (1968) was used for the measurement of permeability. The method involves a small-step change of pore pressure imposed at one end of the sample; then, the pore pressure decay at the other end of the sample is measured. The pressure gradient decays exponentially to zero, and the pressure P_1 in reservoir 1 is given by equation 2 and Figure A 10 in the Appendix.

The next step involved increasing of the sample temperature to various target values of 50°C, 100°C, and 150°C at a rate of 0.8°C/min. Once the target temperature was achieved, pulse decay method was applied to measure permeability. Based on the experimental procedure, after this step the targeted temperature and confining pressure (12.5 MPa) was kept constant, and differential stress was raised at a strain rate of 1.6×10^{-6} until failure and beyond failure regimes.

3.2.3 Uniaxial Compressive Strength (UCS) Tests

Thirteen cylindrical samples with 1:2 length-to-diameter ratios, i.e., 50 mm in diameter and 100 mm in length, were prepared (ISRM 1977) and treated at different temperatures prior to the uniaxial compressive strength tests. The samples were divided into four groups. In the first group, four samples remained untreated (i.e., at ambient temperature). Out of these, two specimens were tested in dry condition and the other two were tested under saturated condition. For the second group, three samples were treated at 50°C and were tested under dry condition. The third group included three samples, which were treated at 100°C. The fourth group included three samples, which were treated at 150°C and then tested under dry condition.

Uniaxial compression tests were carried out according to the ISRM suggested methods (1977) for determining the uniaxial compressive strength and deformability of rock materials. Based on the Phase 1 testing, it was evident that due to the heterogeneous nature of the rock, use of strain gauges to measure the axial deformation will not measure the true axial values of deformation.

Micro-CT scans were performed on selected specimens. Figure 46 shows CT scanning images shaly partings randomly distributed throughout the length of the specimens.

During the Phase 2 testing, two linear variable deformation transducers (LVDT) were also used for measuring the total axial deformation of a specimen instead of relying only on two strain gauges which can only capture the strain locally on the specimen. For diametral strain measurement, two electrical resistance strain gauges were used. Figure 47 shows the test setup with LVDTs and gauges. A discussion on the comparison of the measurements made by LVDTs and strain gauges is presented in Section 3.3.2.

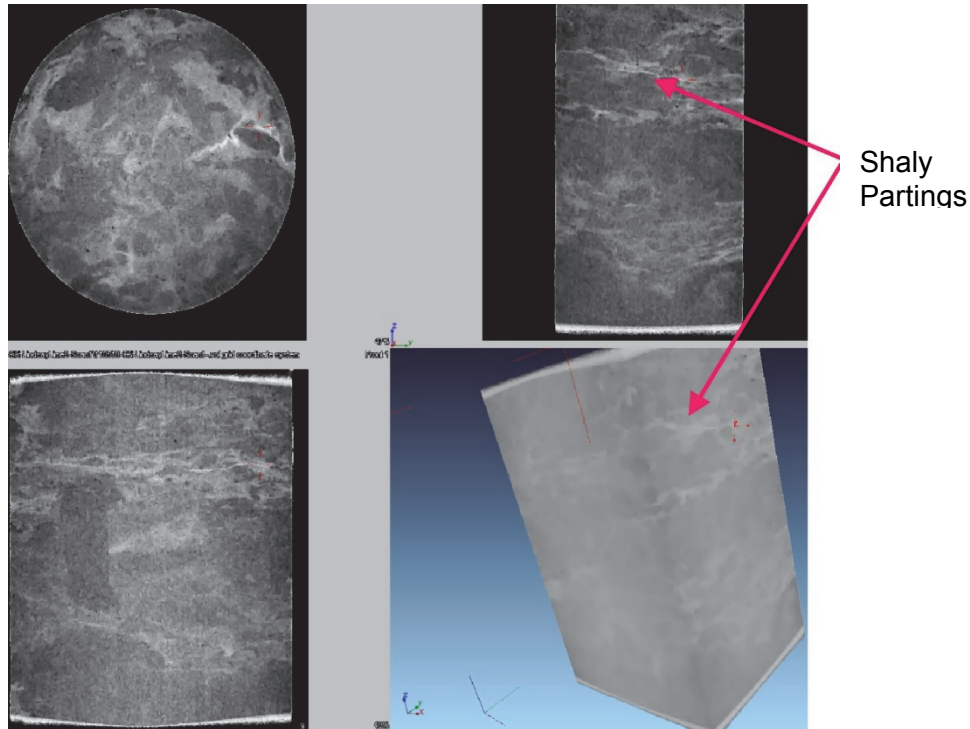


Figure 46: Micro-CT images of a Cobourg specimen (carried out by the U. of Toronto's Geomechanics group)

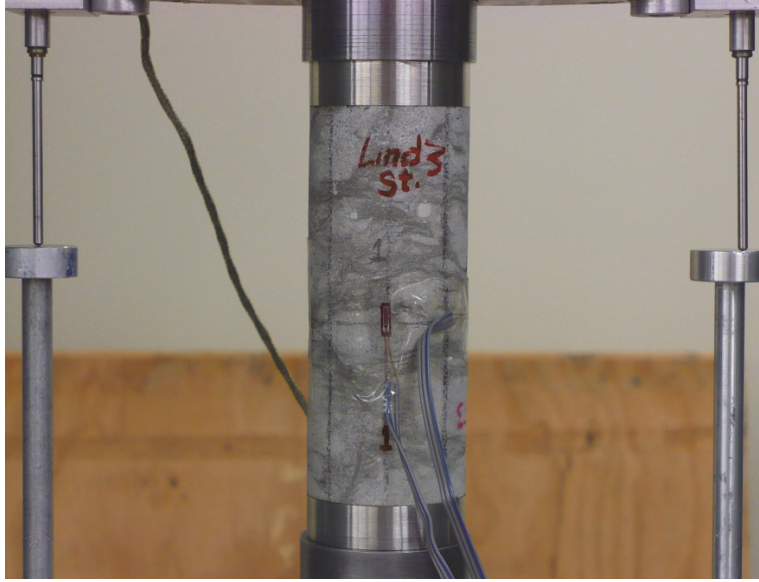


Figure 47: Setup for the comparison of axial measurements by LVDTs and strain gauges

3.2.4 Triaxial Thermo-Hydro-Mechanical Experiments

Nine samples of 50 mm in diameter and 125 mm in length were tested under differential stresses with a confining pressure of 12.5 MPa and a pore pressure of 5 MPa. This mimics the pressure conditions of approximately 500 m underground. The geophysical imaging cell (Figure 50) is equipped with ultrasonic wave velocity sensors oriented along three orthogonal axes of X, Y and Z, enabling the measurement of the evolution of compression and shear wave velocities as a function of in-situ heating and differential stresses. The test specimen sits within a special heat resistant rubber sleeve hosting 12 lateral acoustic emission (AE) pinducers of dual nature (active and passive). The top and bottom loading platens each have 3 AE pinducers, which come in contact with the top and bottom of the specimen. Each of these pinducers can be used as a passive or active source for determining wave velocity evolution during the experiment.

During a triaxial experiment, the saturated specimens were first gradually loaded to 12.5 MPa hydrostatic pressures, after which the pore water pressure was raised to 5 MPa. MTS axial actuator was held under constant displacement control mode once the axial stress reached around 12.5 MPa. For in-situ heating of specimens, a servo-control Teledyne system working with special oil capable of being heated up to 200°C was used. Seismic wave velocity measurements were also made at equal stress intervals prior to the 12.5 MPa of hydrostatic stress. This was done in conjunction with measuring the permeability of the specimen at ambient temperature using the pulse decay method around 12.5 MPa of hydrostatic stress. A servo-control Quizix pump (two-pump system) under independent constant control mode was used to regulate the top and bottom pore pressures and to generate hydraulic pulses for measuring permeability under a hold position for axial load conditions at target temperatures and at various differential stresses up to post failure regions. An internal heater was turned on to regulate the temperature at a rate of 0.8°C/min to reach testing temperatures of 50°C, 100°C, and 150°C under axial displacement control mode. The confining pressure was maintained constant (12.5 MPa) by continuously regulating the additional thermal stresses caused by thermal expansion of the confining fluid using a snorkel as a drainage outlet within the cell. The

MTS actuator's axial displacement control mode helped in measuring the thermal pressurization caused by thermal expansion of the limestone sample during in-situ heating. As the specimen expands, the MTS actuator's load cell (under constant displacement control, restricting axial expansion of the specimen) records only the axial thermal stresses and the in-built cantilever system within GIC (measuring the diametral strain of the specimen) continues to monitor the diametral expansion of the specimen as a function of heat treatment under constant confining stress.

The L8 specimen was tested for two heating cycles, under constant displacement and constant load control modes at the temperature of 150°C, following aforementioned testing procedure. During the first heating cycle, the maximum axial thermal stress was recorded under constant displacement control mode. The specimen was cooled down over night under ambient stresses, after which reheating was performed in constant load control mode. During the second heating cycle, the MTS axial actuator measured the axial expansion of the specimen, while the diametral expansion was monitored with a cantilever system within the triaxial cell (GIC).

During the experiments, in addition to the MTS axial deformational measuring unit, two separate LVDTs were used to measure axial deformation of the specimen (integrated part of GIC, Figure 48) close to the specimen outside the cell. The volumetric strain of the specimen as a function of the temperature rising up to 150°C was determined.

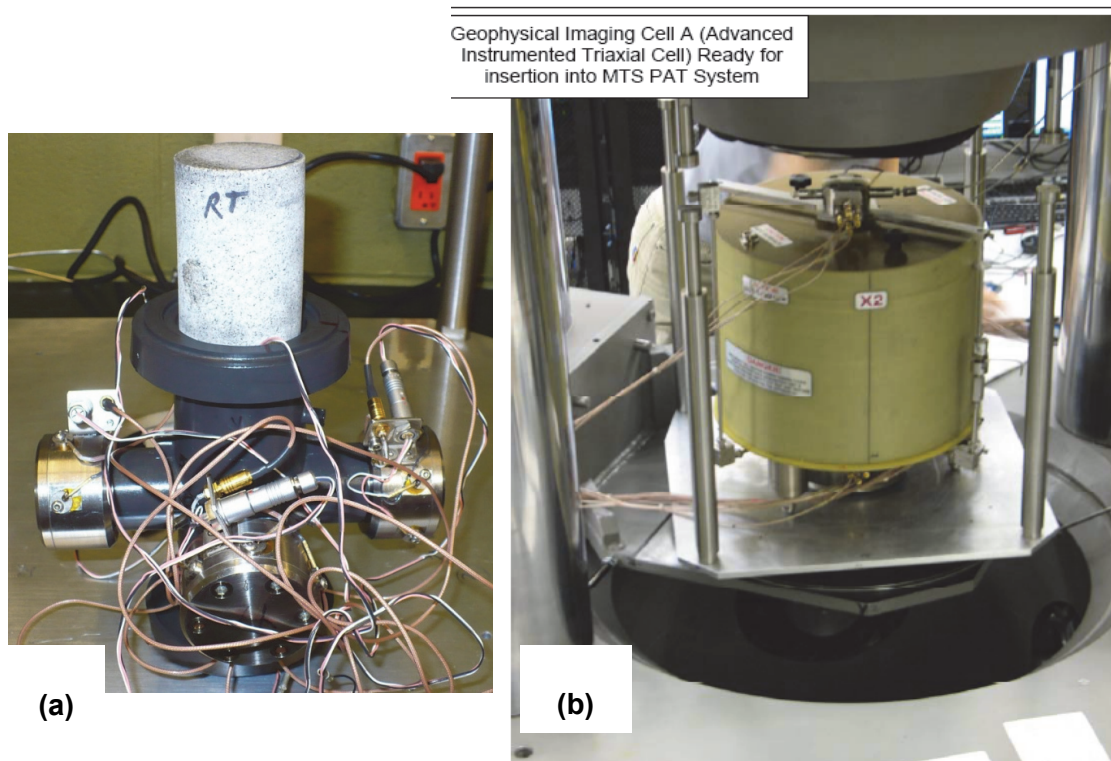


Figure 48: (a) The geophysical imaging cell's internal view of the confining rubber and the X and Y direction velocity stacks along with rock specimen and (b) the cell being setup in the MTS loading machine for testing

3.2.5 Dynamic Elastic Constants

The dynamic elastic constants of the Cobourg limestone specimens were calculated from the measured ultrasonic wave velocities (V_P and V_S) and bulk density (ρ) using the theory of elasticity (Christensen, 1990; Gueguen and Palciauskas, 1998; Tiab and Donaldson, 1996). Thus, the dynamic Young's modulus, E_d , and dynamic Poisson ratio, ν , were calculated as per Equation 4, Section 2.3.5 and as follows and is proposed for isotropic media.

$$\nu = \frac{(V_P / V_S)^2 - 2}{2[(V_P / V_S)^2 - 1]} \quad (5)$$

3.3 RESULTS FROM PHASE 2 TESTING

The experimental results are divided into four parts. The first part is the determination of physical properties of Cobourg limestone. The second part shows the uniaxial compressive strength and deformational properties for dry and saturated room temperature (RT) specimens. Also results of heat-treated dry specimens up to 150°C are reported. The third part reports on the result of the coupled THM experiments under triaxial loading at various temperatures. Finally, the evolution of ultrasonic wave velocities, dynamic elastic constant and permeability as a function of heating under triaxial stresses are presented.

3.3.1 Physical Properties

Determination of the physical properties of Cobourg limestone have been carried out based on ISRM (1981) specifications; the results are presented in Table 6. The specimens showed porosity values varying from 0.53% to 1.04%, which is considered extremely low for a carbonate rock. Since this limestone has an extremely low porosity, saturated and dry densities are close to each other, 2.54 g/cc and 2.66 g/cc, respectively. Thus, the void ratio of the rock is extremely low in the order of 0.005-0.01.

3.3.2 Uniaxial Compressive Strength Test

Uniaxial compressive strengths of dry specimens (L1-RT and L2-RT) were determined under ambient temperature. The specimens show an average UCS value of 82.7 MPa and a quasi-static Young's modulus of the order of 25 GPa. Average UCS value for two saturated samples (L3-RTS and L4-RTS) is 63 MPa, and Young's modulus is about 28 GPa (Table 7). Figures 49 and 50 show the variation of axial strain measured using LVDTs and strain gauges along with diametral strain for L1-RT and L2-RT specimens, respectively. The latter was determined by average strain registered by two strain gauges mounted circumferentially over the specimens.

Stress-strain curves in Figure 51 show that the small axial strain gauges were inadequate to capture the total axial strain during the tests. LVDT, however, could capture the total axial strain, reflecting the overall closure of numerous horizontal to sub-horizontal weak planes during the initial stage of loading and its total axial deformation up to failure. The axial deformation registered through LVDT shows higher values than those determined by axial strain gauges. Similar observation holds for the analysis of stress-strain curves obtained from UCS measurements of saturated specimens of Cobourg limestone (L3-RTS and L4-RTS) as shown in Figures 51 and 52.

Table 6: Physical properties of Cobourg limestone measured in the laboratory

Sample	Length cm	Diameter cm	Vol. Void cm ³	Porosity %	Dry Density g/cc	Saturated Density g/cc	Void Ratio
UCS RT dry							
L1	12.52	5.04					
L2	12.55	5.04					
UCS RT Saturated							
L3	12.53	5.04	1.72	0.69	2.55	2.55	0.01
L4	12.53	5.04	2.59	1.04	2.54	2.55	0.01
Triaxial Tests at RT							
L2	12.48	5.05	1.79	0.72	2.65	2.66	0.01
L6b	12.50	5.05	1.78	0.71	2.64	2.64	0.01
Triaxial Tests at 50°C							
L3	12.47	5.05	1.38	0.55	2.63	2.64	0.01
L4	12.47	5.06	1.64	0.66	2.65	2.65	0.01
Triaxial Tests at 100°C							
L5	12.51	5.15	1.38	0.53	2.55	2.56	0.01
L9	12.49	5.05	1.96	0.79	2.65	2.66	0.01
Triaxial Tests at 150°C							
L7	12.48	5.06	1.15	0.46	2.65	2.65	0.005
L8	12.51	5.11	1.54	0.60	2.59	2.59	0.01

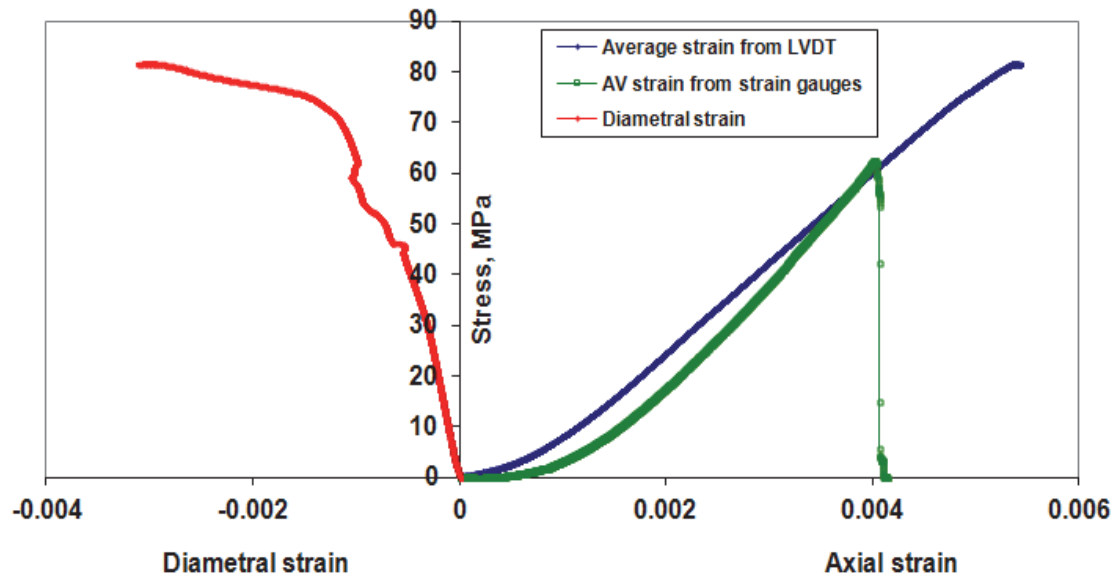


Figure 49: Stress-strain plots of dry Specimen L1-RT, UCS testing

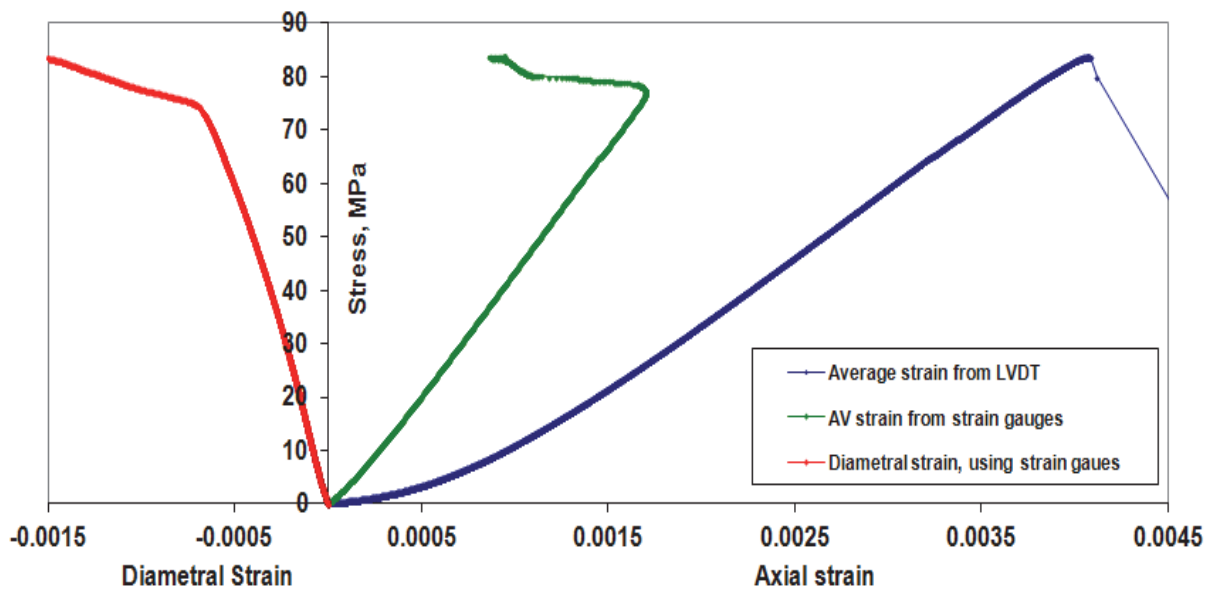


Figure 50: Stress-strain plots of dry Specimen L2-RT, UCS testing

Uniaxial compressive strength of dry specimens that were pre-heated up to 50°C, 100°C and 150°C are listed in Table 7. Three specimens for the aforementioned temperatures were tested under dry conditions. The average values of UCS for the three temperatures are 89 MPa, 91 MPa and 87 MPa, respectively, with an average Young's modulus of 29 GPa, 34 GPa and 27 GPa, respectively. Figure 53 shows tested specimens for the determination of UCS under ambient temperature. Figures 54 to 56 show the stress-strain curves for three categories of thermally treated specimens at 50°C, 100°C and 150°C, respectively. The failure patterns for these three categories of specimens are shown in Figures 57 to 59, respectively.

Table 7: UCS Values of all the Tested Specimens

Sample	Length cm	Diameter cm	Failure Load kN	UCS MPa	E _t GPa	ν
UCS RT Dry						
L1-RT	12.52	5.04	163	81.74	25.3	0.18
L2-RT	12.55	5.04	167	83.75	25.9	0.13
UCS RT Saturated						
L3-RTS	12.53	5.04	125	62.69	31.00	0.23
L4-RTS	12.53	5.04	127	63.69	25.00	0.09
UCS Tests 50°C						
L1-50C	12.48	5.05	193	96.41	24.10	0.06
L2-50C	12.50	5.05	165	82.42	35.00	0.10
L3-50C	12.50	5.05	230	114.89	26.10	0.10
UCS Tests 100°C						
L1-100C	12.51	5.05	163	81.42	36.70	0.06
L2-100C	12.47	5.05	203	101.40	32.18	0.08
L3-100C	12.47	5.05	248	123.88	34.00	0.13
UCS Tests 150°C						
L1-150C	12.48	5.15	166	79.73	22.46	0.07
L2L1-150C	12.49	5.05	191	95.41	24.90	0.10
L3L1-150C	12.49	5.05	257	128.38	34.70	0.12

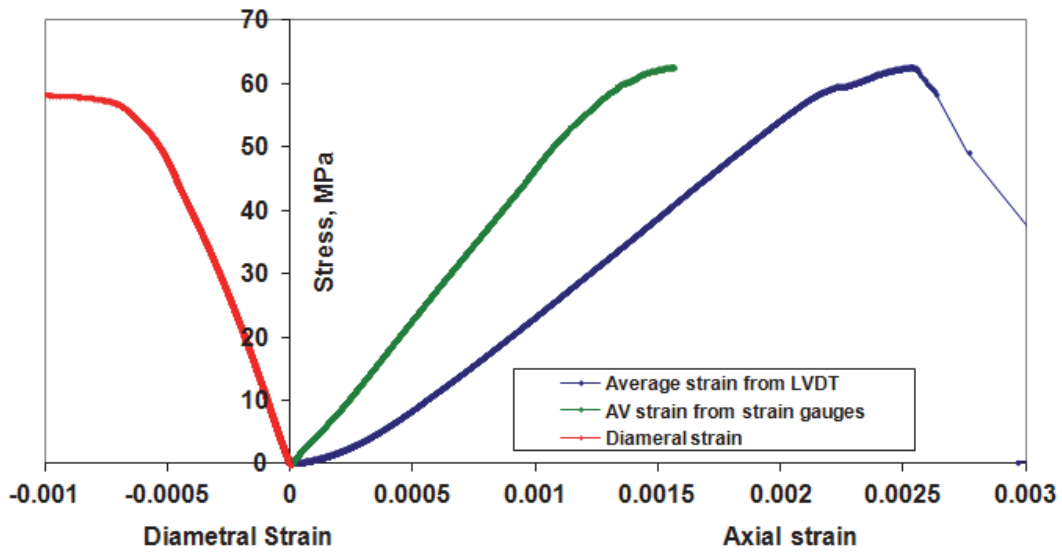


Figure 51: Stress-strain plots of saturated Specimen L3-RT, UCS testing

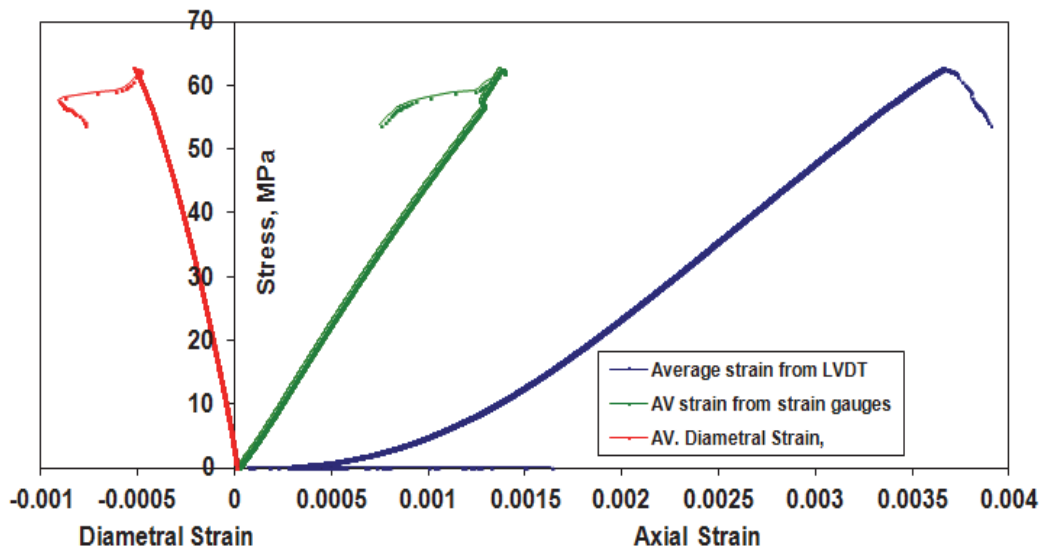


Figure 52: Stress-strain plots of saturated Specimen L4-RT, UCS testing



Figure 53: A photo of Specimens L1-RT, L2-RT, L3-RTS and L4-RTS after tests

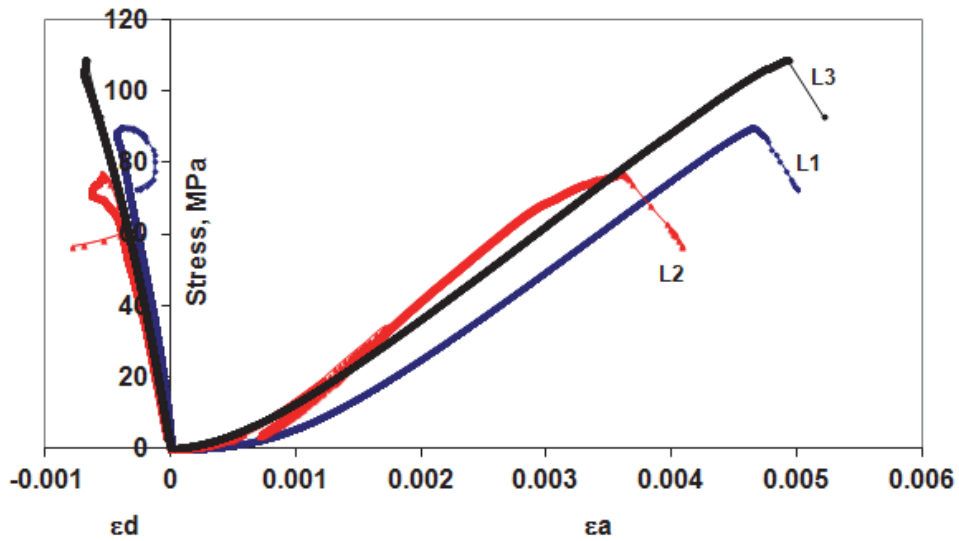


Figure 54: Stress-strain plots of Specimens L1-50 C, L2-50 C and L3-50 C, thermally treated at 50°C

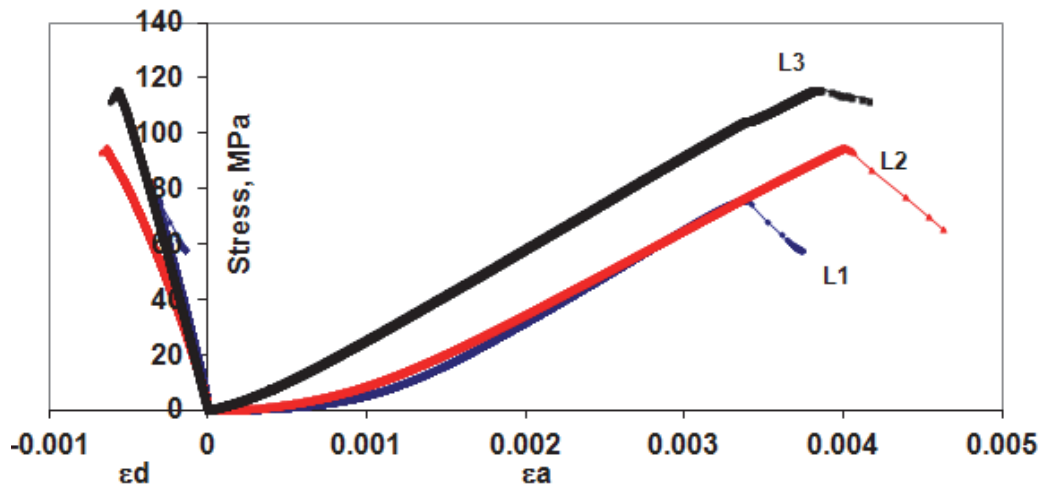


Figure 55: Stress-strain plots of Specimens L1-100 C, L2-100 C and L3-100 C, thermally treated at 100°C

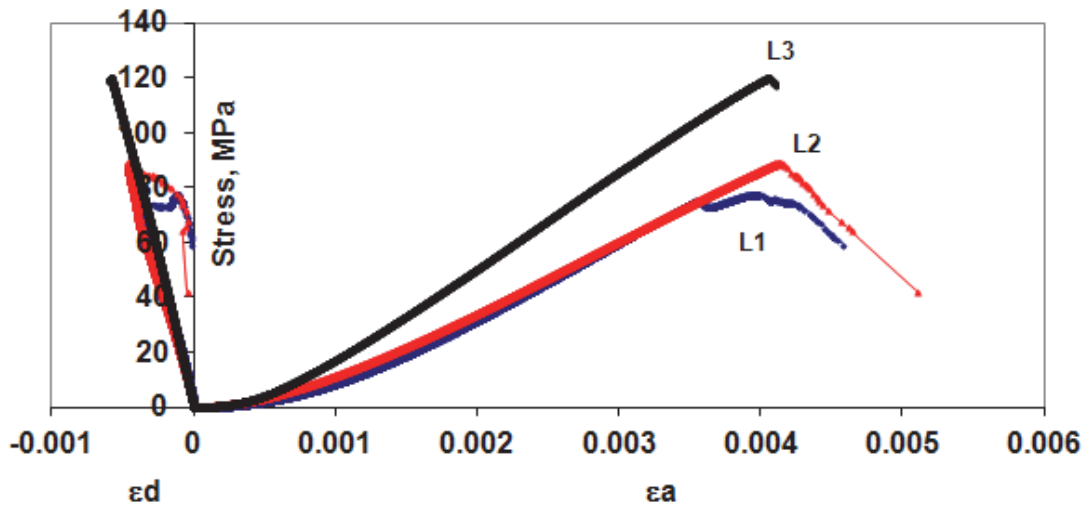


Figure 56: Stress-strain plots of Specimens L1-150 C, L2-150 C and L3-150 C, thermally treated at 150°C



Figure 57: A photo of thermally treated Specimens L1-50 C, L2-50 C and L3-50 C after tests



Figure 58: A photo of thermally treated Specimens L1-100 C, L2-100 C and L3-100 C after tests



Figure 59: A photo of thermally treated Specimens L1-150 C, L2-150 C and L3-150 C after tests

It is worth mentioning that during testing in the loading cell, the built-in AE sensors (central frequency of 1.3 MHz) could not record AE events emitted from the limestone samples, which is characterized with AE spectral peaks of about 100 kHz. Efforts are being made to replace the AE sensors with lower frequency ones for subsequent AE analysis of softer rock types. In order to delineate fracture propagation and AE events of lower frequency within the limestone, a uniaxial compression test using a larger dimension specimen (190 mm × 100 mm) was performed. Eight PAC transducers with an effective frequency range of 35 to 100 kHz were attached to the specimen. Using CA6 amplifiers having a bandwidth of 10 kHz to 10 MHz and a maximum output of 1 V_{rms} , amplified AE events were continuously acquired by an ASC Richter unit sampling at 10 MHz. Full analysis of AE investigation of this experiment is reported in the appendix of this report.

3.3.3 Triaxial Thermo-Hydro-Mechanical Tests

A total of eight specimens were tested according to the testing plan outlined in Table 5 under coupled THM in order to evaluate the effect of confining pressure and heating up to 150 °C on strength, deformation, and permeability of Cobourg limestone. Two specimens were tested under ambient temperature.

3.3.3.1 Testing at Room Temperature, HM Tests

Cobourg limestone Specimens L2b and L6b were tested under ambient temperature in the geophysical imaging cell according to the experimental method and testing procedure explained in section 3.2.4.

Figure 60 shows the stress-strain curves along with volumetric strain of this specimen at ambient temperature and confining pressure of 12.5 MPa. The L6b specimen failed at 117 MPa. The built-in cantilever within the GIC cell registered a maximum average diametral strain of 0.2% and the axial strain of 0.6% was measured using two LVDTs, attached to the top and bottom platens outside the cell.

The evolution of seismic wave velocities (V_P) as a function of differential stress increments up to failure and beyond for the L6b specimen is illustrated in Figure 61. V_P continuously increases along the Z direction, which is parallel to the axial loading direction up to a differential stress of 110 MPa. V_P measured along two horizontal directions (X and Y) initially showed a little increase up to a differential stress of 30 MPa, followed by a total decrease of about 0.2 km/s as differential stress was increased to 110 MPa. V_P for the latter directions experienced much steeper decrease just prior to the failure strength of 117 MPa.

Figure 62 shows shear wave velocity V_{S1} and its polarization (V_{S2}) as a function of differential stress along three perpendicular directions (X, Y and Z axes) for the L6b specimen. Along the axial load direction (Z axis), V_{S1Z} and V_{S2Z} show an increasing trend, whereas shear wave velocities show a decreasing trend for both horizontal directions (X and Y axes) up to 110 MPa of differential stress, beyond which the decrease rate becomes steeper.

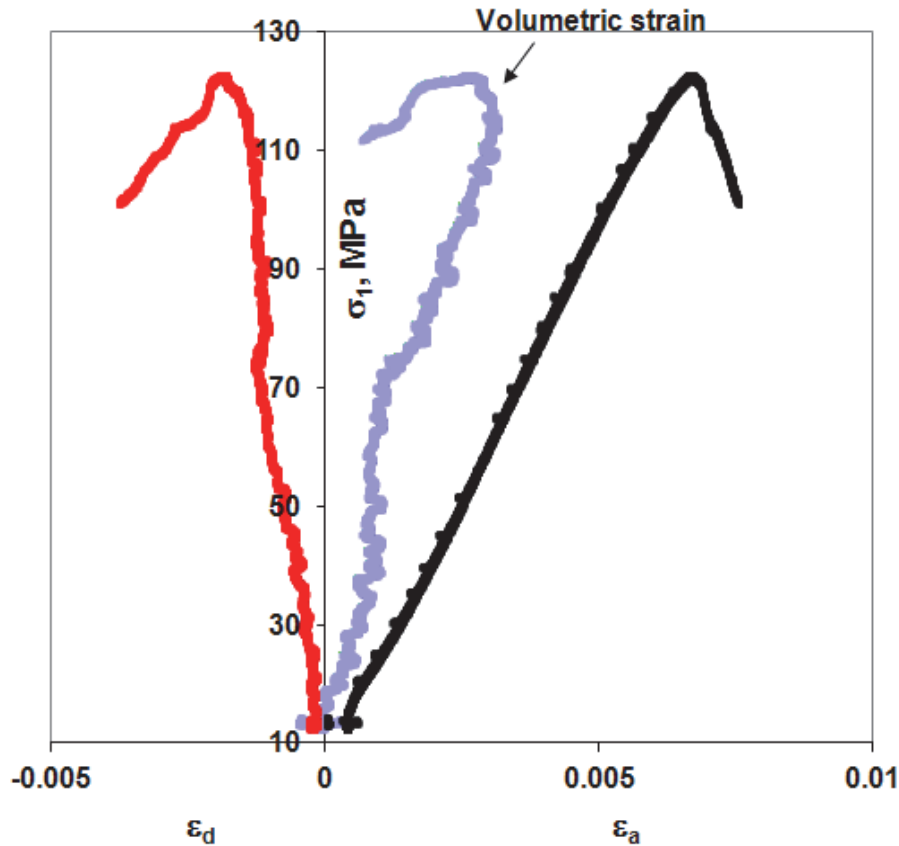


Figure 60: Axial, diametral and volumetric strain plots of Specimen L6b under HM testing

These observations show that as differential stress is increasing along the Z axis and as closure of weak shaly partings occurs, V_P , V_{S1} and V_{S2} increase, whereas V_P , V_{S1} and V_{S2} for both horizontal directions after an initial increase indicate a systematic decrease. Such a decrease can be related to the growth of microcracks and associated damage parallel to main principal stress direction. Figure 63 shows the shear wave splitting (the difference in percentages between two shear velocities propagating at right angle to each other) and its variation measured along three directions as a function of axial stress increments. The splitting percentages along horizontal axes are higher than along the vertical axis, which reflects the effect of horizontally oriented shaly partings on shear velocity changes. The sharp increase rate of such splitting prior to failure is due to an increased rate of the generation of axial microcracks parallel to the Z axis. Figure 64 shows the tested L2 and L6b specimens.

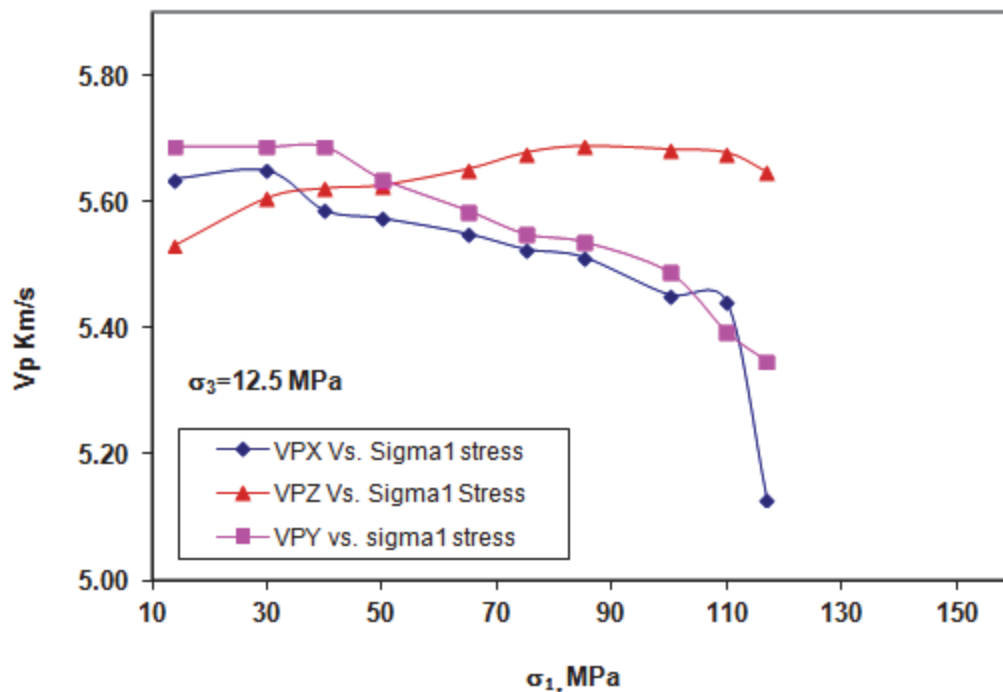


Figure 61: Evolution of V_P along two horizontal directions (X and Y axes) and the vertical direction (Z axis), with differential stresses in coupled HM testing of Specimen L6b under ambient temperature

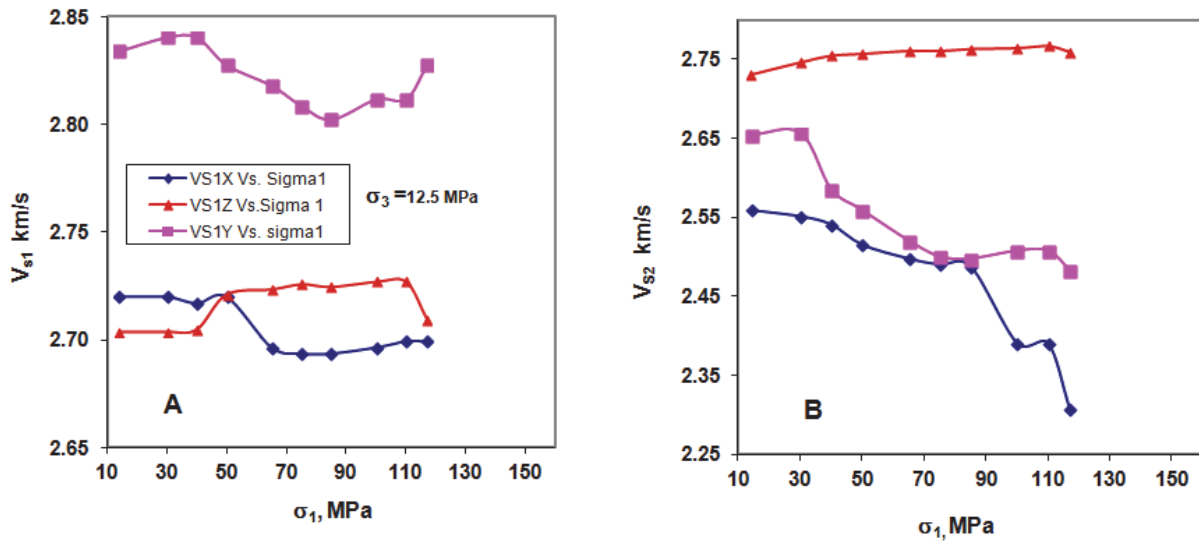


Figure 62: Evolution of (a) V_{s1} , and (b) V_{s2} with differential stresses in coupled HM testing of Specimen L6b under ambient temperature

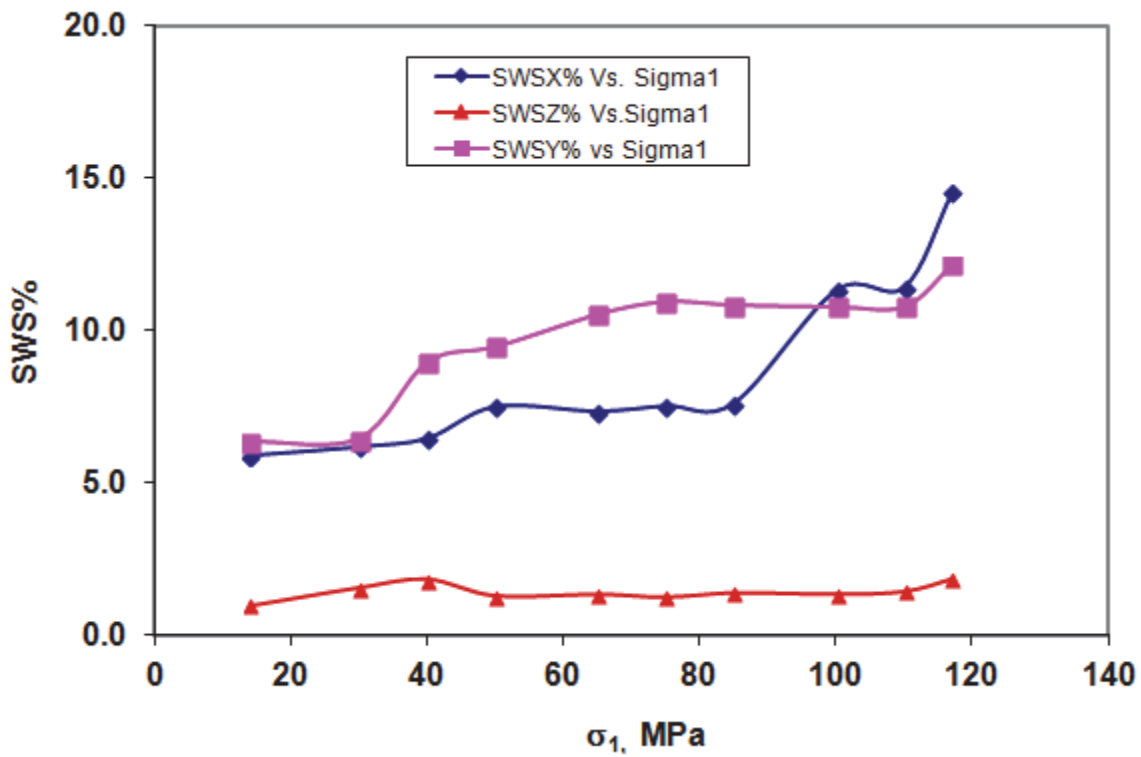


Figure 63: Evolution of shear wave splitting (SWS) with differential stresses in coupled HM testing of Specimen L6b under ambient temperature



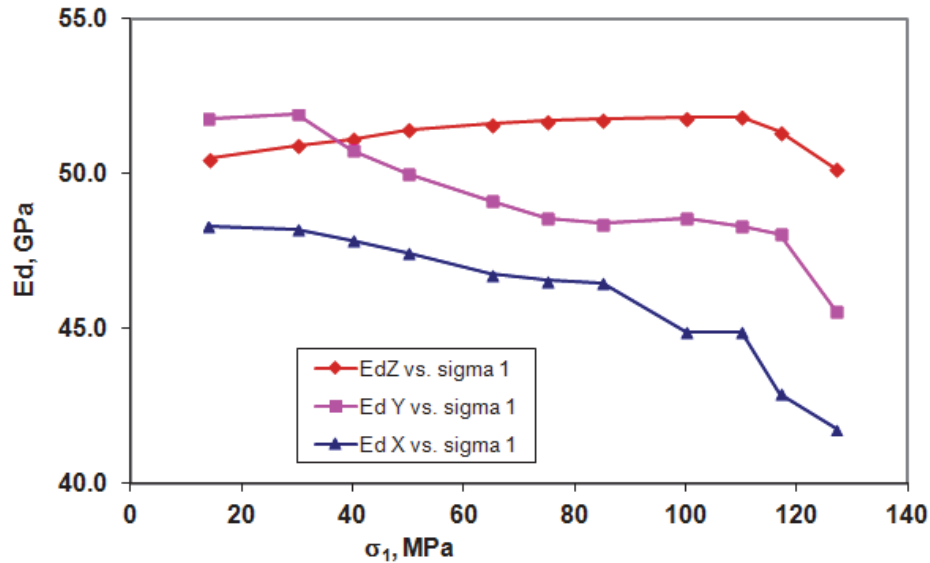
Figure 64: A photo of Specimens L2 and L6b after tests

Dynamic Young's modulus and dynamic Poisson's ratio were calculated based on the formulas presented in Section 3.2.5 (equation 5). Table 8 and Figure 65 show the evolution of the dynamic elastic constants as a function of differential stresses up to failure and post failure regimes.

The evolution of modulus with differential stress reflects similar behaviour observed in seismic wave velocities as a function of differential stresses along three axes (Figure 65). The dynamic modulus in the vertical direction, E_{dz} , shows a different trend than those in the horizontal directions. It has an increasing trend up to 110 MPa due to the closure of shaly partings following a decrease as the formation of microcracks commenced. Whereas E_{dx} and E_{dy} both show a decreasing trend (approximate 4 GPa) when axial stress reaches 110 MPa. Nucleation and coalescence of microcracks mainly parallel to Z direction affects the dynamic Young's modulus measured along two horizontal directions.

Table 8: Dynamic elastic constant calculated along three axes for Specimen RT6b

σ_1 MPa	$E_d, X \text{ axis}$ GPa	$\nu_{X \text{ axis}}$	$E_d, Y \text{ axis}$ GPa	$\nu_{Y \text{ axis}}$	$E_d, Z \text{ axis}$ GPa	$\nu_{Z \text{ axis}}$
14	48.3	0.36	51.77	0.35	50.49	0.34
30	48.21	0.36	51.92	0.35	50.94	0.35
40	47.86	0.36	50.77	0.35	51.14	0.35
50	47.47	0.36	50.02	0.35	51.45	0.34
65	46.77	0.36	49.13	0.35	51.62	0.35
75	46.56	0.36	48.57	0.35	51.73	0.35
85	46.49	0.36	48.4	0.35	51.78	0.35
100	44.9	0.36	48.58	0.35	51.82	0.35
110	44.92	0.36	48.32	0.34	51.84	0.35
117	42.93	0.34	48.05	0.34	51.36	0.35
127	41.77	0.34	45.55	0.35	50.16	0.35

**Figure 65: Variation of dynamic Young's moduli with differential stresses for Specimen L6b**

3.3.3.2 Testing at 50 °C, THM Tests

Cobourg limestone specimens L3 and L4 were tested at 50°C within the geophysical imaging cell according to the experimental method and testing procedure explained in section 3.2.4

Figures 66 and 67 show the variation of axial, diametral and volumetric strain as a function of differential stress to failure and beyond for two specimens of L3 and L4. During the test, seismic wave velocities were measured during the temperature increase. Once the target temperature was reached, differential stress was raised and wave velocities were measured at 10 MPa intervals until failure. Specimens L3 and L4 failed at 108 MPa and 80 MPa of axial stress, respectively, experiencing 0.37% of axial strain. The L3 specimen experienced 0.15% of diametral and 0.18% of volumetric strain at failure. The L4 specimen showed 0.1% of diametral and 0.11% of volumetric strain. Since the thermal pressurization experienced by these specimens was negligible, lesser volumetric strain was registered during the heating of these specimens. The thermal pressurization for these two specimens was about ~1.5 MPa as these samples were heated from ambient temperature of about 25°C to 50°C.

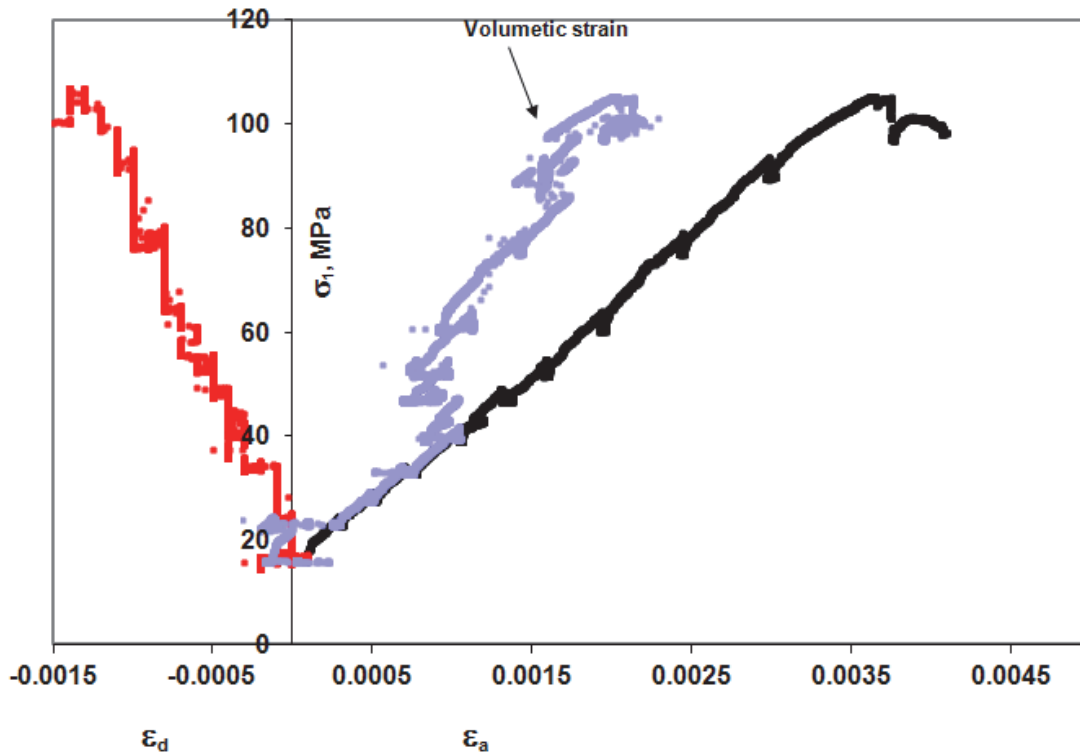


Figure 66: Stress-strain and volumetric strain plots of Specimen L3

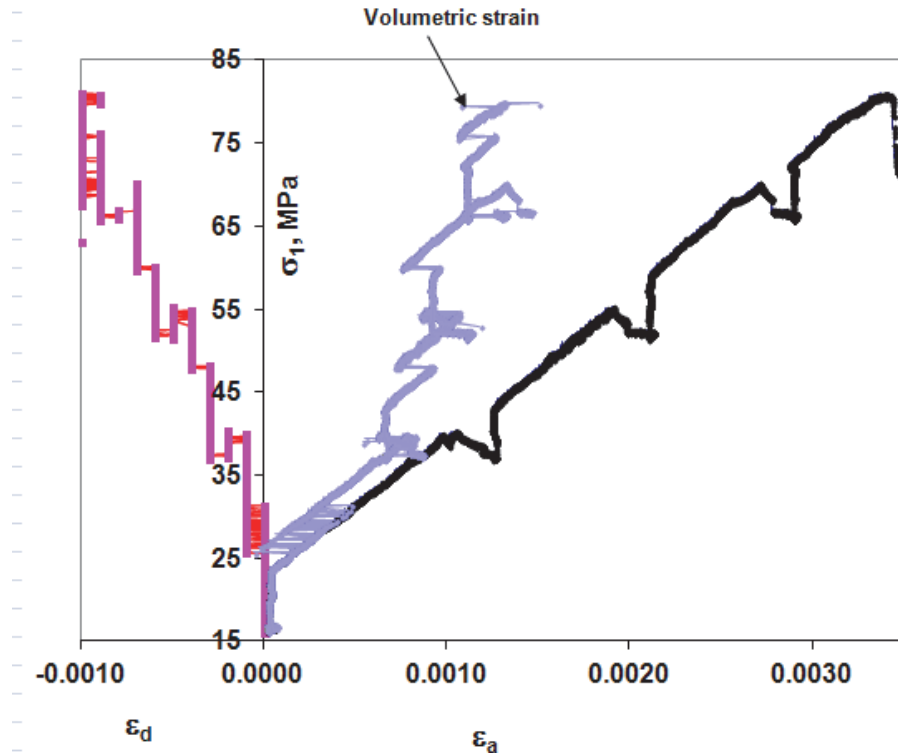


Figure 67: Stress-strain and diametral strain plots of Specimen L4

Figures 68 and 69 show the evolution of compression and shear wave velocities for the L3 specimen as a function of axial stresses along horizontal and vertical directions. Figures 70 and 71 show similar variations for the L4 specimen, measured along two horizontal (X and Y) axes and the vertical Z axis. Thermal stresses measured for both specimens were negligible during the heating process up to 50°C. The axial stress increased from 15.5 MPa to 17 MPa during heating, and thermal expansion of the specimens was captured by seismic wave velocity measurements characterized with an initial decrease of V_P for both the Y and the Z axes (marked in the green oval in Figures 70a). V_{PZ} increased along the Z axis when differential stress increased to 70 MPa. V_{PY} shows a steeper decrease before ultimate failure of the specimen occurs at 108 MPa as formation of microcracks parallel to Z axis cause the reduction of V_{PY} . The initial steep increase in V_{PZ} as a function of differential stresses is interpreted to be caused by the closure of microcracks and shaly partings oriented perpendicular to the Z axis or the loading direction.

Shear wave velocity for V_{S1Y} (Figure 68b) also shows a steep initial decline during heating, followed with a shallow decline as differential stress is increased under constant temperature prior to failure. V_{S1} velocity along the vertical Z axis does not show much variation during heating. Figure 71 shows the evolution of V_{S2} (polarized shear wave velocity with respect to V_{S1}) as a function of in-situ heating and differential stresses along the Y and Z axes. Figures 70 and 71 show the variation of seismic wave velocities as a function of temperature and differential stresses for L4 specimen. These figures confirm a similar scenario to L3 specimen and show reproducibility of coupled THM properties under similar testing environment. Figure 74 shows failed Specimens L3 and L4 recovered from the loading cell. The failed specimens

(Figure 72) are marked with fewer axial failure cracks, compared to UCS specimens in Figure 59.

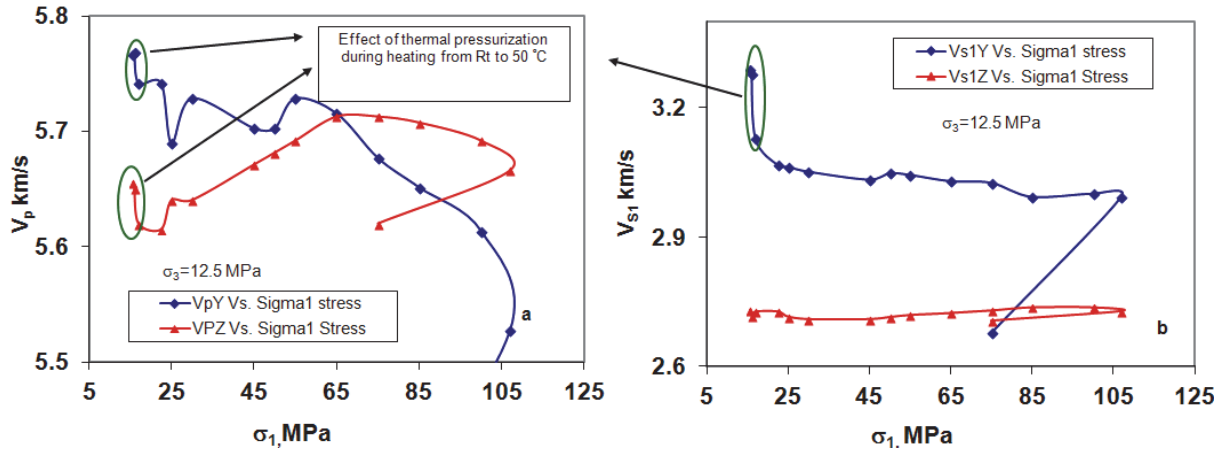


Figure 68: Evolution of (a) V_p and (b) V_{s1} along Y and Z axes of Specimen L3 during heating and differential stress increments

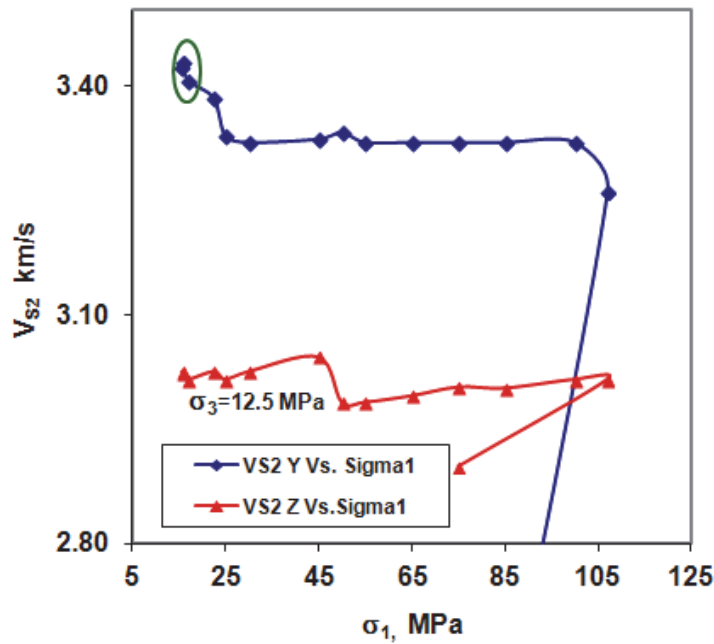


Figure 69: Evolution of V_{s2} along the Y and Z axes of Specimen L3 during heating and differential stress increments

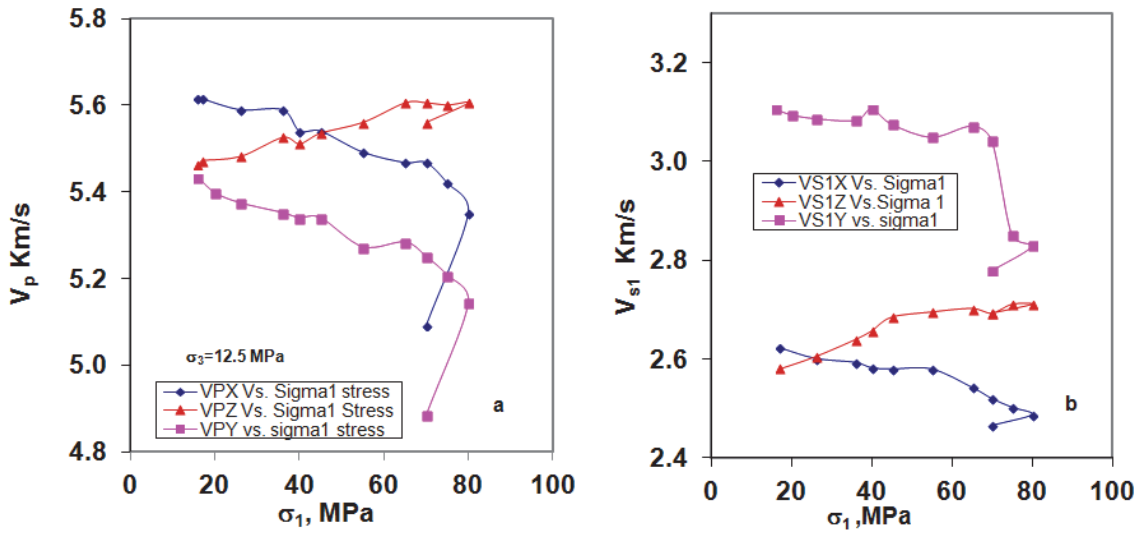


Figure 70: Evolution of (a) V_p and (b) V_s along Y and Z axes of Specimen L4 during heating and differential stress increments

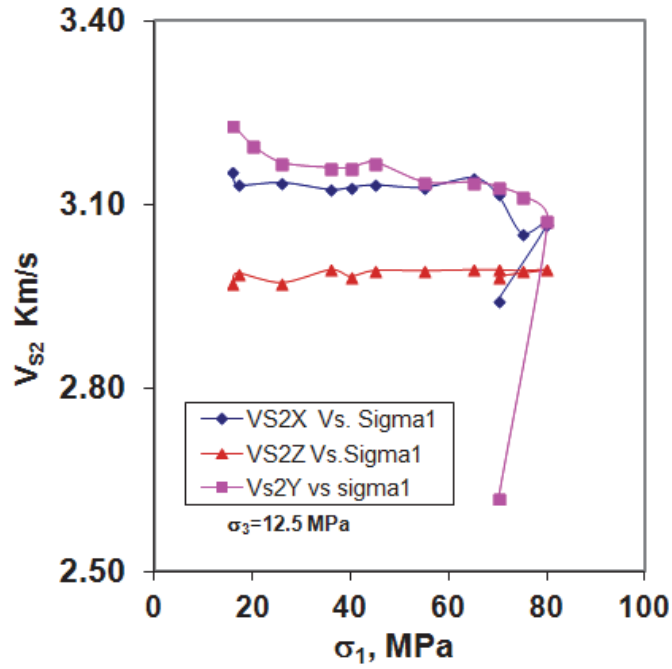


Figure 71: Evolution of V_{s2} along the Y and Z axes of Specimen L4 during heating and differential stress increments



Figure 72: A photo of Specimens L3 and L4 after tests

Table 9 and Figure 73 display evolution of dynamic elastic constants for Specimen L3. Table 10 and Figure 74 show the same for Specimen L4. Both of these specimens show an initial negligible reduction of dynamic Young's modulus due to lateral thermal expansion. This phenomenon is not noticeable along Z axis for both Specimens L3 and L4 due to the fact that thermal expansion was restricted axially in order to record the thermal pressurization. The latter caused 1.5 MPa of axial thermal stress in both the specimens. Variation of dynamic modulus with differential stresses along the axial direction in both specimens shows that the value increases in response to closure of inherent microcracks. Whereas the measurement along the horizontal directions show a progressive decline characterized with steeper decrease prior to yield strength for both the specimens. This behaviour confirms that differential stress increments beyond the elastic response leads to generation of microcracks parallel to the loading direction, coalescence of which cause final failure. Post-failure dynamic Young's modulus measured along all axes is characterized with reduced values for both specimens.

Table 9: Variation of dynamic elastic constant along three axes during heating of Specimen L3 up to 50°C.

Temp. °C	Vertical Stress MPa	Ed, Y axis GPa	ν Y axis	Ed, Z axis GPa	ν Z axis
27	15.67	71.48	0.24	55.99	0.33
31	16	71.44	0.24	55.74	0.33
50	17	68.65	0.26	55.65	0.32
50	22.5	67.37	0.27	55.79	0.32
50	25	66.24	0.27	55.53	0.33
50	30	65.94	0.27	55.60	0.33
50	45	65.72	0.27	56.01	0.33
50	50	66.08	0.27	55.16	0.33
50	55	65.82	0.27	55.27	0.33
50	65	65.60	0.27	55.56	0.33
50	75	65.54	0.27	55.84	0.33
50	85	65.05	0.28	55.92	0.33
50	100	64.70	0.27	56.05	0.33
50	107	63.10	0.26	55.83	0.33
50	75	42.08	0.37	53.47	0.33

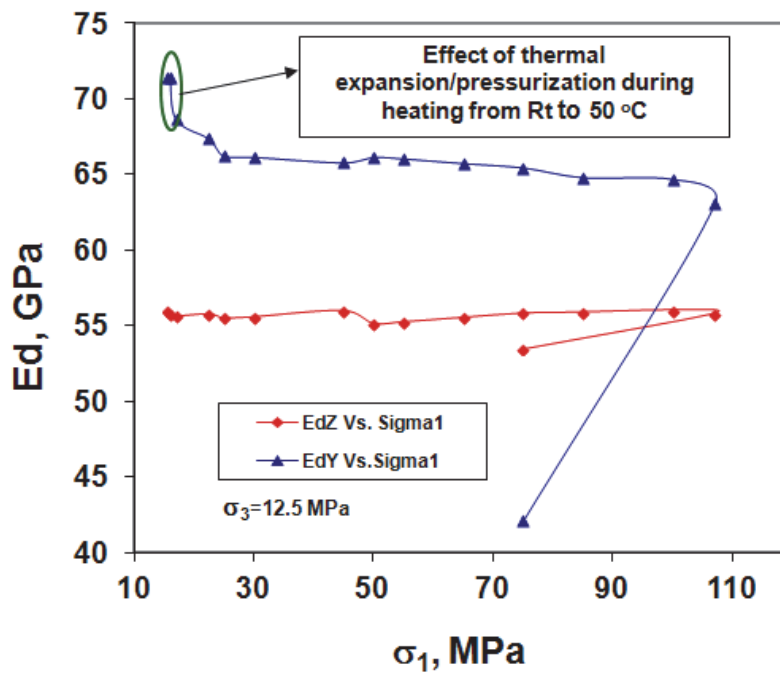


Figure 73: Evolution of dynamic Young's moduli with differential stresses in Z and Y directions for Specimen L3

Table 10: Variation of dynamic elastic constant along three axes during heating of Specimen L4 up to 50°C.

Temp. °C	Vertical Stress MPa	Ed, Z axis GPa	ν_Z axis	Ed, Y axis GPa	ν_Y axis	Ed, X axis GPa	ν_X axis
27	16	52.18	0.32	63.97	0.23	59.78	0.29
35	16	52.02	0.33	62.80	0.24	59.62	0.30
40	16	52.10	0.33	63.55	0.25	56.34	0.30
50	16	52.40	0.33	62.69	0.24	55.81	0.32
50	20	52.55	0.33	62.03	0.24	55.44	0.32
50	26	53.59	0.33	61.71	0.24	55.13	0.32
50	36	53.62	0.32	61.93	0.24	54.84	0.32
50	40	54.29	0.32	61.63	0.24	54.86	0.32
50	45	54.54	0.32	60.36	0.24	54.62	0.32
50	55	54.84	0.32	60.74	0.24	54.21	0.31
50	65	54.69	0.33	60.00	0.24	53.43	0.31
50	70	54.93	0.33	56.96	0.24	52.01	0.32
50	75	54.97	0.33	55.74	0.26	51.76	0.32
50	80	54.35	0.33	47.57	0.25	48.60	0.32

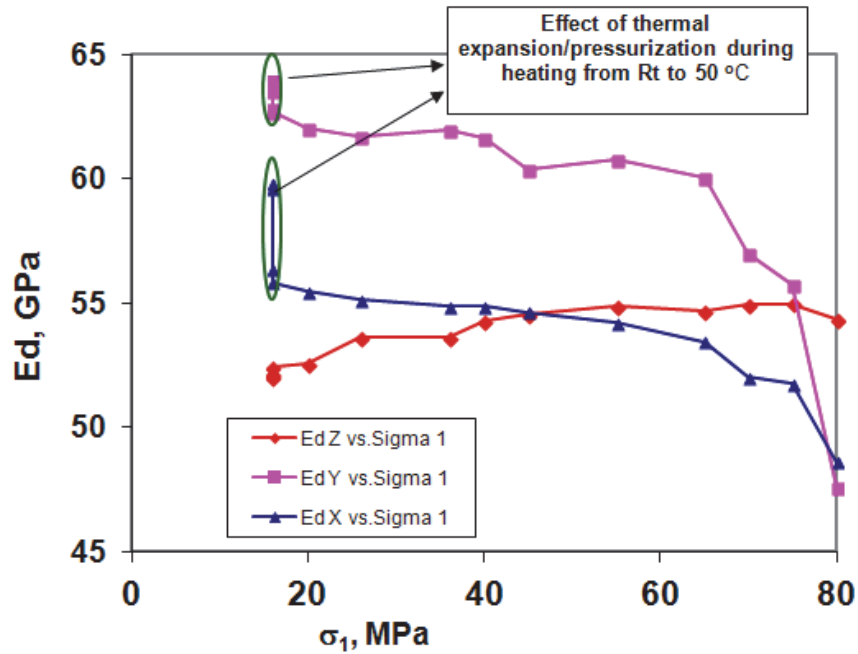


Figure 74: Evolution of dynamic Young's moduli with differential stresses in Z and Y directions for Specimen L4

As part of the THM testing, the pulse decay method was applied to calculate permeability (k) of the specimens at hydrostatic stress of 12.5 MPa, at ambient temperature. After which, specimens were heated at a rate of 0.8 °C/min to the target value of 50°C. Once the target value was reached, the pulse decay method was applied under the same lateral confinement of 12.5 MPa, as well as under additional axial stress caused by thermal expansion of the specimen. In this method, the two ends of the specimen were connected to a Quizix pump applying 5 MPa of pore pressure. At a predetermined effective stress of 7 MPa (for 50°C specimens), a pulse was introduced at the upstream side of the specimen and the specimen's pore pressure decay was measured over time. An equivalent procedure was repeated for higher differential stresses. Figure 75 and 76 show the response of permeability and V_p for Specimens L3 and L4 as a function of hydrostatic stress and at ambient temperature.

Permeability was found to decrease after heating due to thermal pressurization/expansion of the specimens. Further decrease in permeability as a function of differential stress was due to the compaction of pore spaces and closure of microcracks along shaly partings oriented perpendicular to the loading direction. The permeability value was found to increase as the load reached 60 MPa, with a sharp increase around 90 MPa, followed by a decline (not shown in the figure) in the post failure regime for Specimen L3. The evolution of permeability for the L4 specimen followed a similar trend, with the exception that it reached its lowest level when the load reached 40 MPa and showed a maximum level when the load was 70 MPa.

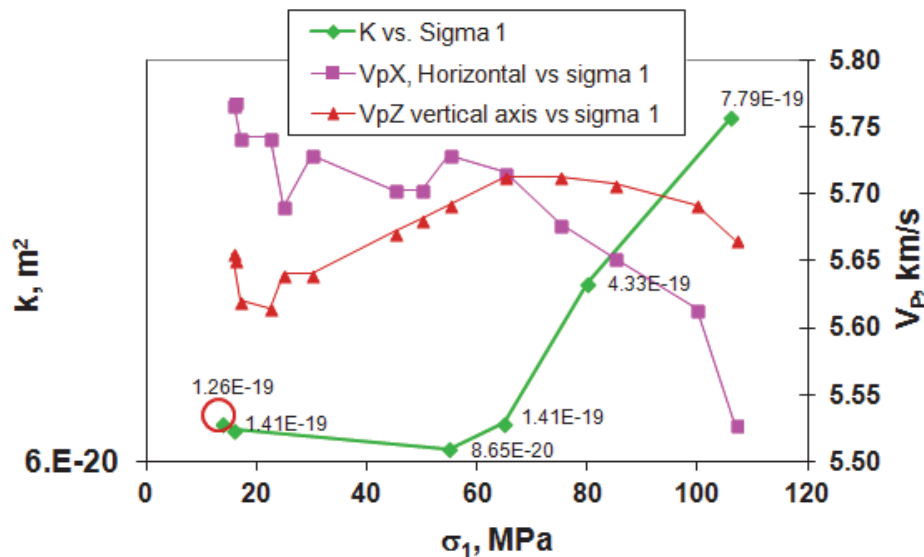


Figure 75: Evolution of permeability and V_p of Specimen L3 as a function of hydrostatic stress at room temperature (value shown in the red circle), and as a function of increased axial stress increments

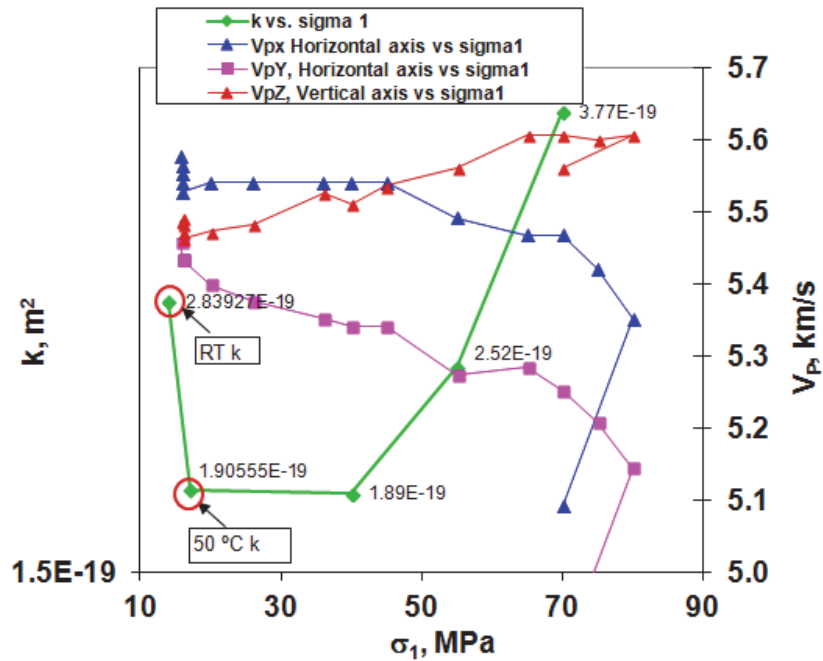


Figure 76: Evolution of permeability (RT k) and V_p of Specimen L4 as a function of hydrostatic stress at room temperature and as a function of increased axial stress increments (50°C k)

3.3.3.3 Testing at 100°C, THM Tests

Cobourg limestone Specimens L5 and L9 were tested at 100°C in-situ temperature within the geophysical imaging cell according to the experimental method and testing procedure outlined in section 3.2.4.

Figures 77 to 80 show the variation of axial, diametral and volumetric strains as a function of temperature during the heating for the L5 and L9 specimens. The specimens were heated in-situ up to 100°C under constant displacement control mode once a hydrostatic stress of 12.5 MPa was achieved within the load cell. Thermal stresses were recorded as the specimens were not permitted to expand axially due to constant displacement control mode. Once the target temperature was reached, differential stress was increased, while temperature and confining pressure were maintained at constant levels. During differential stress increments, wave velocities and permeability were measured at certain stress intervals until failure and beyond.

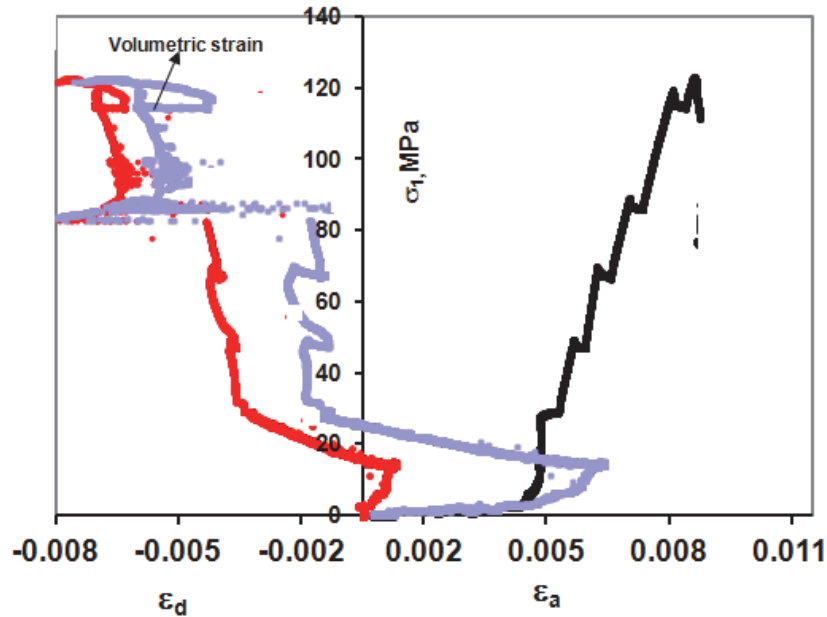


Figure 77: Stress-strain and diametral strain plots of Specimen L5

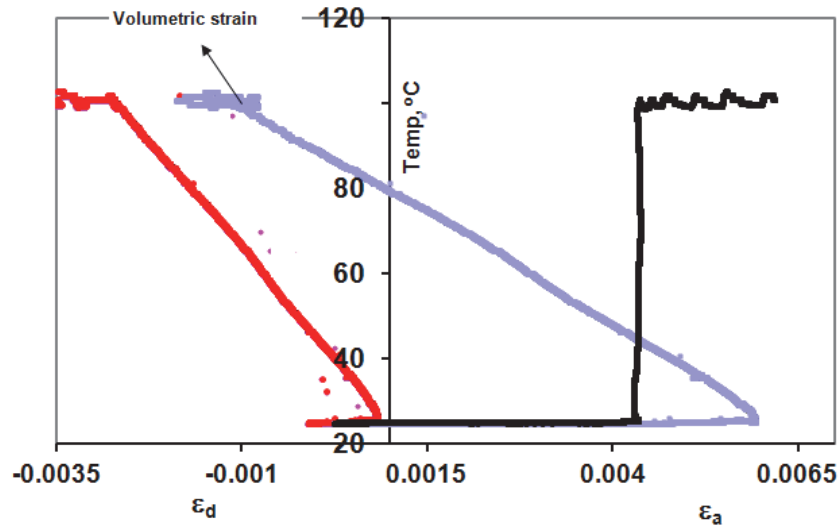


Figure 78: Axial, diametral and volumetric strain during in-situ heating of Specimen L5 under the MTS displacement control mode

The L5 specimen (100°C, Figure 77) experienced higher axial, diametral and overall volumetric strain than the L3 and L4 specimens (50°C) during heating and failure. The L5 specimen failed at around 120 MPa of axial stress, and experienced a total 0.65% of diametral strain, 0.7% of axial strain, and a total of ~1.3% volumetric strain up to failure during the test. The specimen registered 0.25% of diametral strain, no axial strain, and 0.1% of volumetric strain during the heating procedure under constant confining pressure of 12.5 MPa (Figure 78).

The L9 specimen failed at higher strength (140 MPa, Figure 79), experiencing 0.4 % axial strain, 0.25% diametral strain excluding the diametral strain due to heating, and 0.6% of volumetric strain. During heating the L9 specimen experienced 0.3% of diametral strain and no axial strain, since heating was carried out under the displacement control mode, restraining axial expansion of the sample in order to measure the axial thermal pressurization (Figure 80). Thermal stress of 16 MPa was registered by the axial actuator during the heating procedure, at a rate of 0.22 MPa/°C. A similar rate was observed for the L5 specimen tested under similar conditions as Specimen L9. Figure 81 shows failed Specimens L5 and L9 recovered from the loading cell.

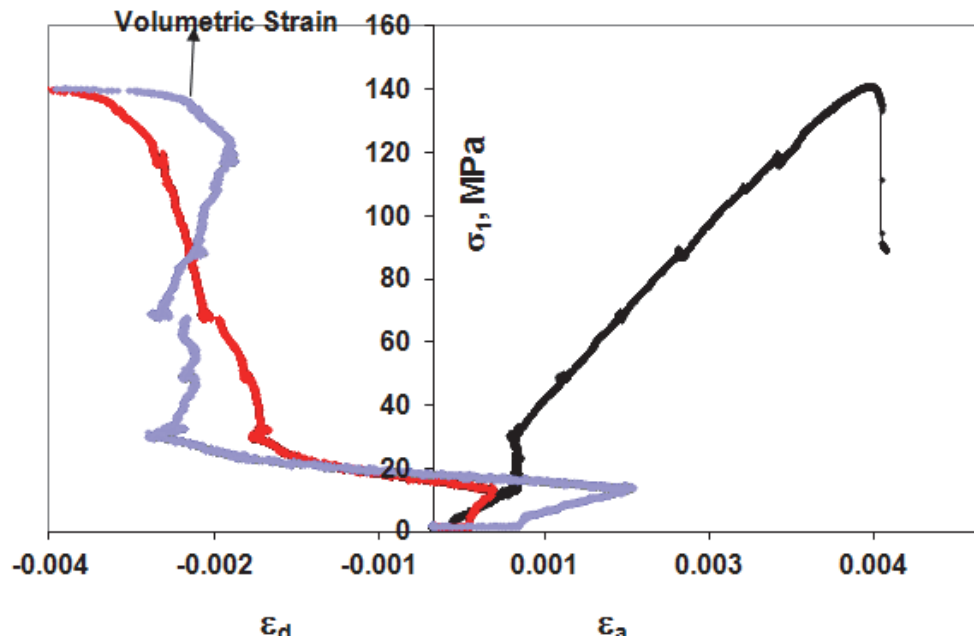


Figure 79: Stress-strain and diametral strain plots of Specimen L9

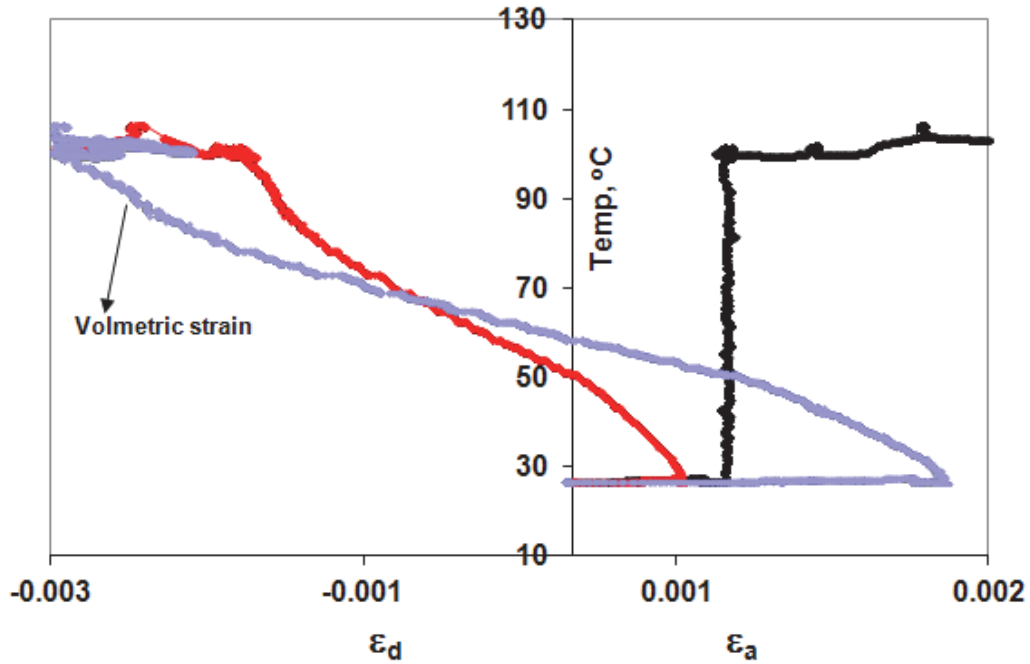


Figure 80: Axial, diametral and volumetric strain during in-situ heating of Specimen L9 under the MTS displacement control mode.



Figure 81: A photo of Specimens L5 and L9 after testing

This section reports on the evolution of in-situ heating of the L5 and L9 specimens up to 100°C on seismic wave velocities under constant confining pressure of 12.5 MPa and a constant axial displacement control. Figure 82a shows the evolution of V_P for horizontal directions (X and Y

axes) and along the vertical direction (Z axis) during heating up to 100°C and as a function of differential stress increments up to failure. Figure 82b shows the same for shear wave velocity evolution. The axial stress rose from 14.5 MPa to 30 MPa during heating. The thermal pressurization (due thermal expansion) of both specimens was captured by seismic wave velocity measurements showing an initial decrease in V_P along the X, Y and Z axes. For both samples, V_P measured along the Z axis increased when differential stress increased to 110 MPa, followed by a decline in velocity before ultimate failure of the specimens. The initial steeper V_{PZ} increments as a function of axial stress were interpreted to be due to the closure of microcracks and weak shaly partings oriented perpendicular to the Z axis (loading direction). Compression wave velocities measured along the two horizontal axes (X and Y) decreased due to the growth of axial microcracks due to increased axial stresses before failure (V_{PX} and V_{PY} , in Figures 82a and 84a). The evolutions of shear wave velocities as a function of in-situ heating under constant lateral stress and later on as a function of differential stresses along three directions follow a similar trend to that of compression wave velocities observed for both the L5 and the L9 specimens (Figures 82b, 83, 84b and 85). The variation of shear wave velocities during heating and differential stress increments captures the thermo-mechanical responses of the rock.

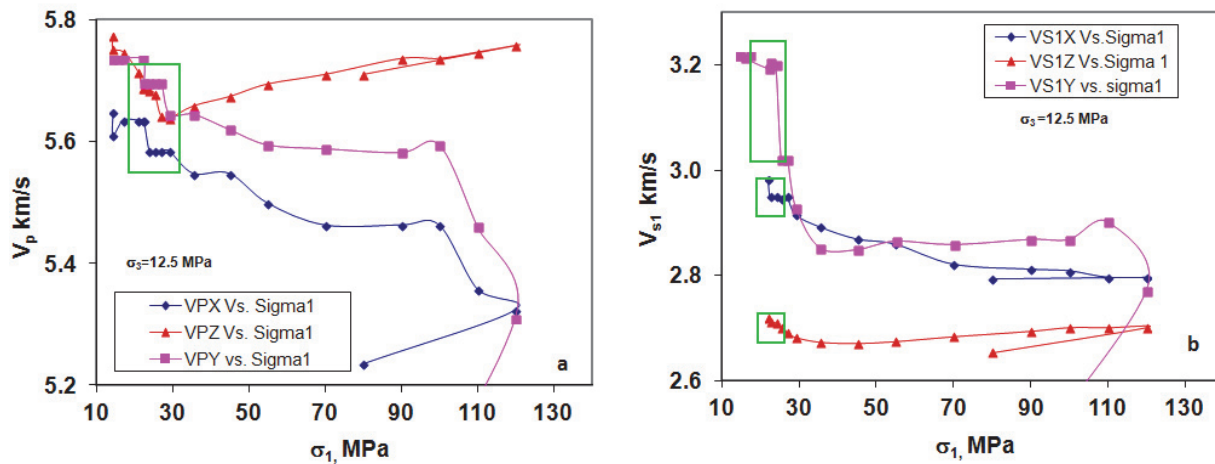


Figure 82: Evolution of (a) V_P and (b) V_S along the X, Y and Z axes of Specimen L5 during heating and differential stress increments. The points in the box show the effect of thermal heating

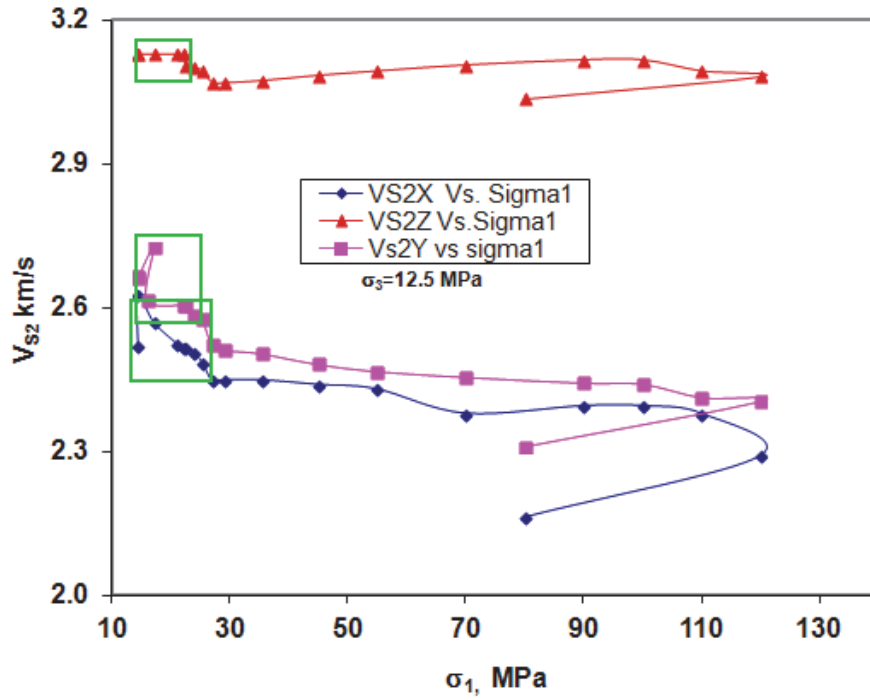


Figure 83: Variation of V_{s2} along the X, Y and Z axes of Specimen L5 during heating and differential stress increments. The points in the box show the effect of thermal heating

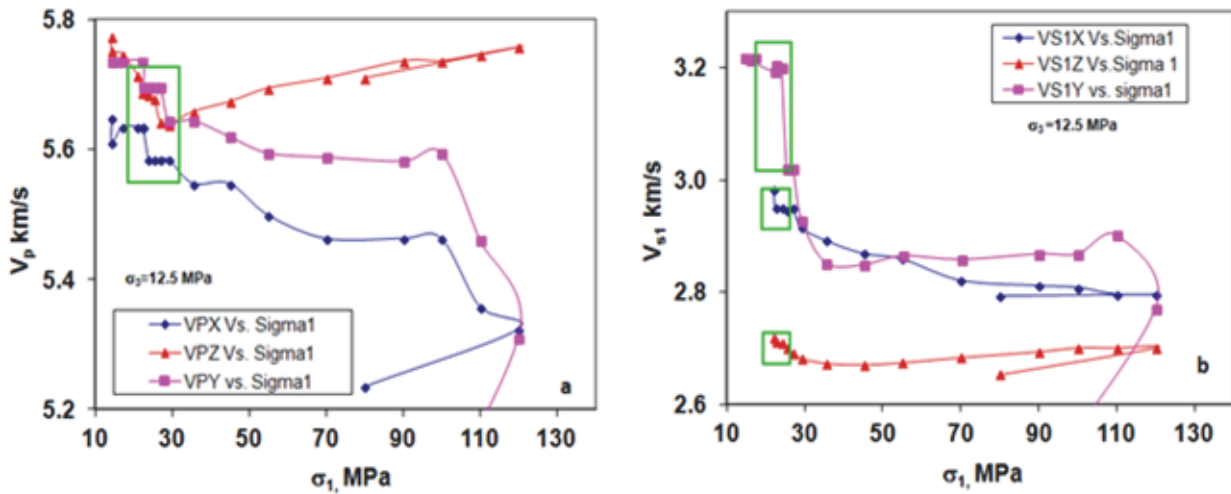


Figure 84: Variation of (a) V_p and (b) V_{s1} along the X, Y and Z axes of Specimen L9 during heating and differential stress increments. The points in the box show the effect of thermal heating

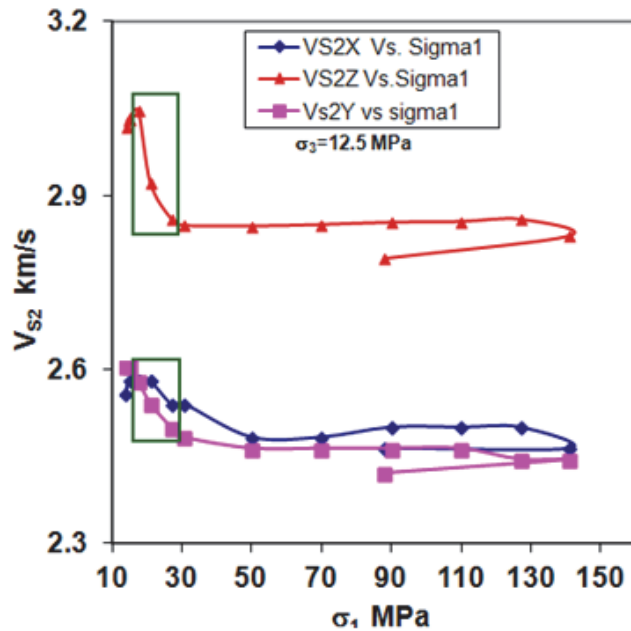


Figure 85: Variation of V_{s2} along the X, Y and Z axes of Specimen L9 during heating and differential stress increments

Table 11 and Figure 86 show the evolution of dynamic elastic constants measured during in-situ heating up to 100°C and differential stress up to failure and beyond for Specimen L5. Calculated dynamic modulus along X and Y axes show a reduction of 1.7 and 7 GPa respectively as the temperature is raised from 25°C to 100°C. Specimen L5 shows anisotropy in the modulus as a function of heating. This reduction is related to the lateral expansion of Specimen L5. The reduction for vertical direction for the same specimen is 4 GPa during heating. Calculated modulus along two horizontal (X and Y axes) directions show a reduction of 2 GPa and 4 GPa for Specimen L9 heated in the same way up to 100°C (Table 12 and Figure 87). Dynamic modulus calculated along vertical direction (Z axis) show a reduction of 5 GPa for Specimen L9. The thermal pressurization for both specimens record a value of 15 MPa as the temperature is raised to 100°C.

Table 11: Variation of dynamic elastic constants along three axes during the heating up to 100°C for Specimen L5

<i>Temp.</i> °C	<i>Vertical Stress</i> MPa	<i>Ed, Z axis</i> GPa	<i>ν_Z axis</i>	<i>Ed, Y axis</i> GPa	<i>ν_Y axis</i>	<i>Ed, X axis</i> GPa	<i>ν_X</i>
25	14.5	58.34	0.34	58.27	0.32	51.72	0.35
35	14.5	57.84	0.34	58.24	0.32	53.18	0.33
46	17.16	57.92	0.33	59.27	0.32	52.07	0.34
68	16	57.65	0.33	57.46	0.33	52.16	0.34
72	22.11	57.53	0.33	56.95	0.33	51.77	0.34
76	22.6	57.08	0.32	57.01	0.32	51.31	0.35
80	24	56.98	0.32	56.6	0.33	50.97	0.34
84.6	25.4	56.69	0.32	53.54	0.34	50.6	0.35
92.5	27	56.02	0.32	52.7	0.34	50.08	0.35
100	29.19	55.85	0.32	50.89	0.35	49.54	0.35
100	35.5	55.85	0.33	49.55	0.35	49.07	0.35
100	45	56.04	0.33	47.93	0.36	48.56	0.35
100	55	56.31	0.33	49.3	0.35	48.13	0.35
100	70	56.71	0.33	48.72	0.35	46.66	0.35
100	90	57.15	0.33	48.53	0.35	46.76	0.35
100	100	57.26	0.33	48.68	0.35	46.71	0.35
100	110	56.92	0.33	48.41	0.34	46.02	0.35
100	120	56.76	0.33	45.9	0.34	44.59	0.35
100	80	55.07	0.34	37.58	0.35	42.42	0.36

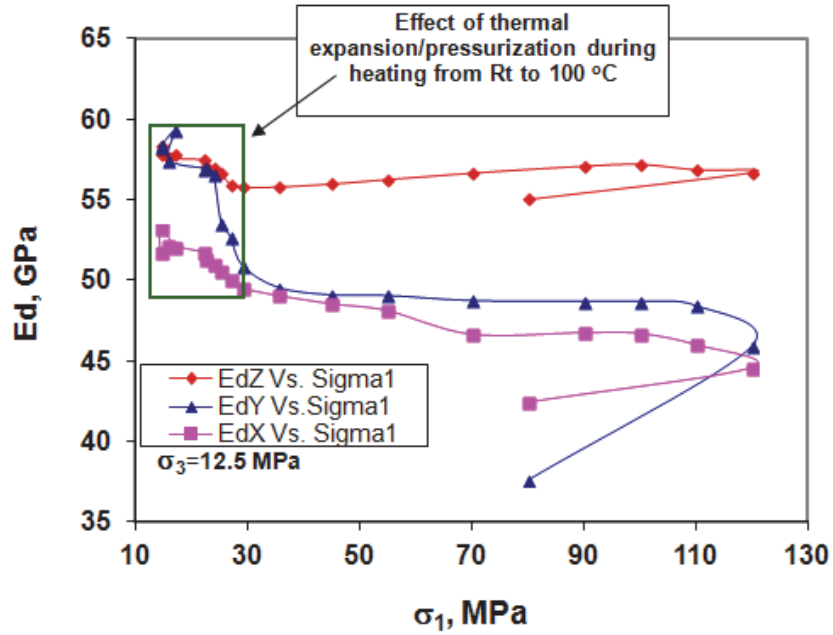


Figure 86: Evolution of dynamic moduli of Specimen L5 with differential stresses along X, Y and Z directions

Table 12: Variation of dynamic elastic constants along three axes during heating up to 100°C of Specimen L9

Temp. °C	Vertical Stress MPa	Ed, Z axis GPa	ν_Z axis	Ed, Y axis GPa	ν_Y axis	Ed, X axis GPa	ν_X axis
26	14	59.13	0.32	55.11	0.31	54.55	0.32
35	14.9	58	0.32	55.11	0.31	55.26	0.32
50	17.6	58.2	0.32	54.41	0.31	54.76	0.32
70	21.1	55.96	0.33	53.16	0.31	53.64	0.31
90	27	54.59	0.33	51.77	0.32	52.47	0.32
100	30.78	54.18	0.33	51.15	0.31	52.47	0.32
100	50	54.03	0.33	50.58	0.32	50.99	0.32
100	70	54.36	0.34	50.58	0.32	50.24	0.32
100	90	54.5	0.34	50.5	0.32	50.6	0.32
100	110	54.65	0.34	50.03	0.32	49.23	0.32
100	127	54.74	0.34	49.09	0.32	47.92	0.32
100	141	53.85	0.34	47.41	0.31	46.94	0.31
100	88	52.38	0.35	45.94	0.31	44.15	0.31

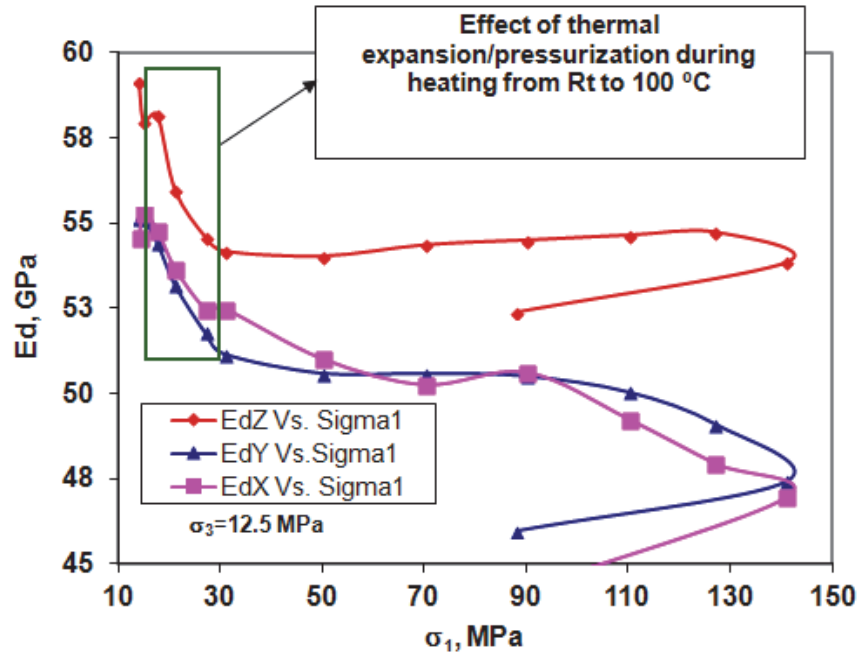


Figure 87: Evolution of moduli of Specimen L9 with differential stresses along X, Y and Z directions

Figure 88 and 89 show the response of the permeability of the Cobourg limestone Specimens L5 and L9 as a function of hydrostatic stress under ambient temperature. The figures also show permeability at the raised temperature (100°C) and at increased differential stresses. Permeability was found to decrease after heating due to thermal stress/expansion and the thermo-mechanical effect of the specimens. Both specimens experienced additional 15 MPa of axial stress during heating and such an additional thermal stress leads to compaction of the specimen under loading platens. The compacted zones become less permeable, and the hydraulic pulses are introduced into newly compacted zones, take a longer time for decay. Further decrease of permeability as a function of differential stress increments (up to 50 MPa) is due to the closure of microcracks along weak shaly partings oriented perpendicular to the loading direction. The permeability was found to increase when the load was increased from 50 MPa to 90 MPa. The changes in permeability with differential stress are stronger for the L5 specimen. The increase is related to the development of new microcracks parallel to the load. V_p measured along both horizontal directions (X and Y) for both specimens shows a further decrease corresponding to axial stresses and development of new microcracks oriented parallel to the loading direction.

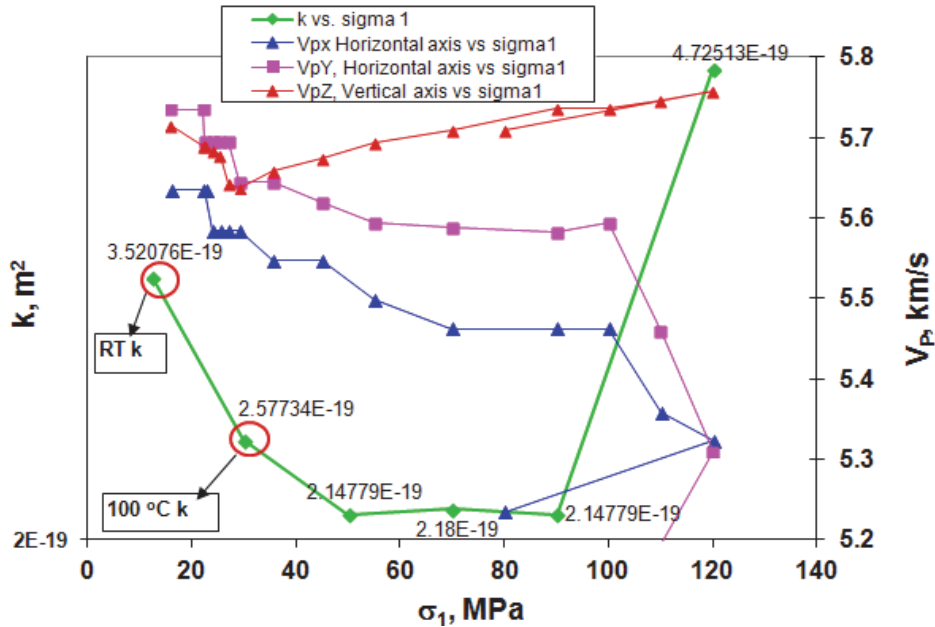


Figure 88: Evolution of permeability and V_p of Specimen L5 as a function of hydrostatic stress, and as a function of increased temperature, and differential stress increments

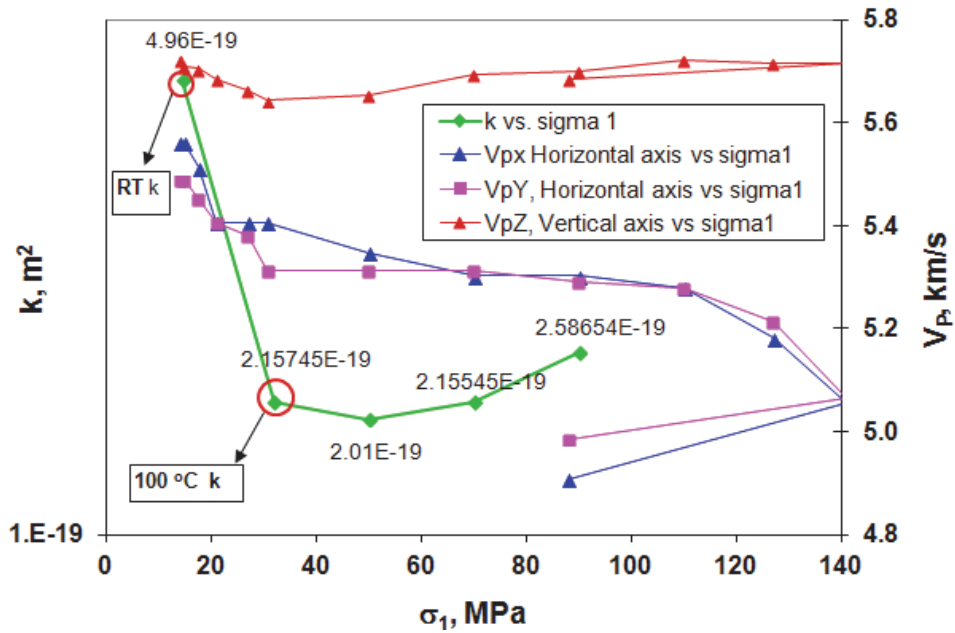


Figure 89: Evolution of permeability and V_p of Specimen L9 as a function of hydrostatic stress, and as a function of increased temperature, and differential stress increments

3.3.3.4 Testing at 150°C, THM Tests

Specimen L7 has been tested at 150°C within the geophysical imaging cell up to failure and beyond according to the experimental method and testing procedure described in section 3.2.4. Specimen L8 was subjected to two cycles of heating. First, the specimen was heated in-situ under confined lateral stress and constant displacement control. Then the sample was unloaded to ambient pressure and cooled overnight in the cell. The second cycle of heating to the target temperature of 150°C was carried out under constant load control to evaluate its volumetric expansion (axial and diametral expansion both were permitted), and to evaluate any thermal damage during the first cycle of heating. The results from this test are presented in the following section.

Figure 90 shows the variation of axial, diametral and volumetric strain as a function of axial stress up to failure for Specimen L7. Figure 91 shows the same as a function of temperature during the heating process.

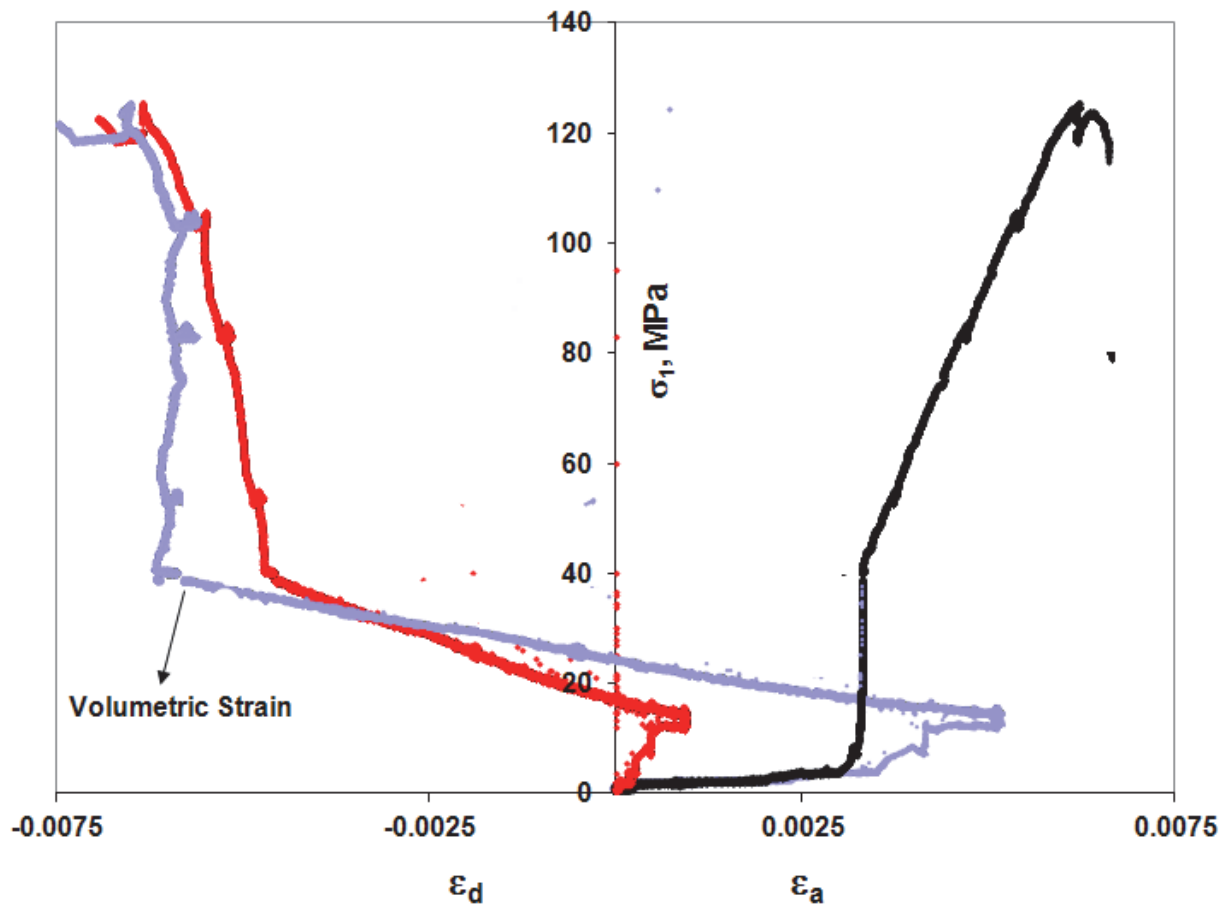


Figure 90: Stress-strain and diametral strain plots of Specimen L7

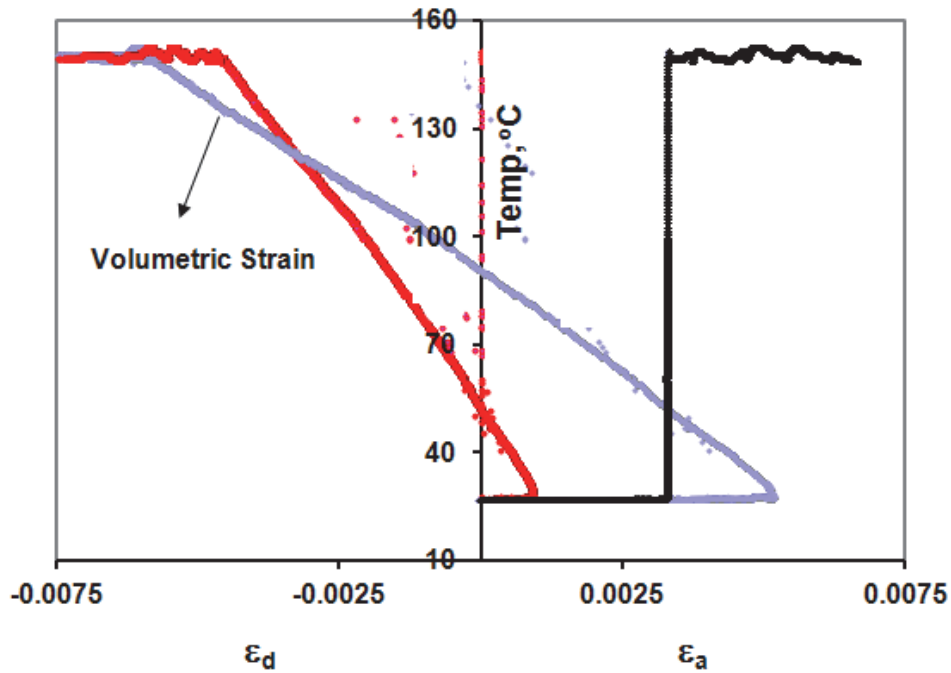


Figure 91: Axial, diametral and volumetric strains of Specimen L7 during in-situ heating under the displacement control mode.

The specimen has a failure strength of 125 MPa under coupled THM conditions, and experienced an axial strain of 1.25%, lateral strain of 0.63% (including the thermal expansion part), and total volumetric strain of 0.6% up to failure. During the heating the axial strain was 0%, diametral 0.5% and volumetric strain of 1.2% measured under constant displacement control mode.

3.3.4 Specimen L7

Figures 92 and 93 show the evolution of compression and shear wave velocities during the THM experiment for the L7 specimen. Both compression and shear wave velocities decreased as temperatures reached 150°C. Later the velocity increased as the differential stress increased during the loading until the failure. The microcracks and weak shaly partings closed during the axial loading. Velocities showed a large decline during heating but did not show any decline in the initial stages of differential stress increments. The velocities started to decrease when the axial stress reached a value of 110 MPa, showing the initiation of axial microcracks. Figure 93b shows the variation of shear wave splitting with differential stress. And Figure 94 shows the failure pattern for specimens L7 and L8.

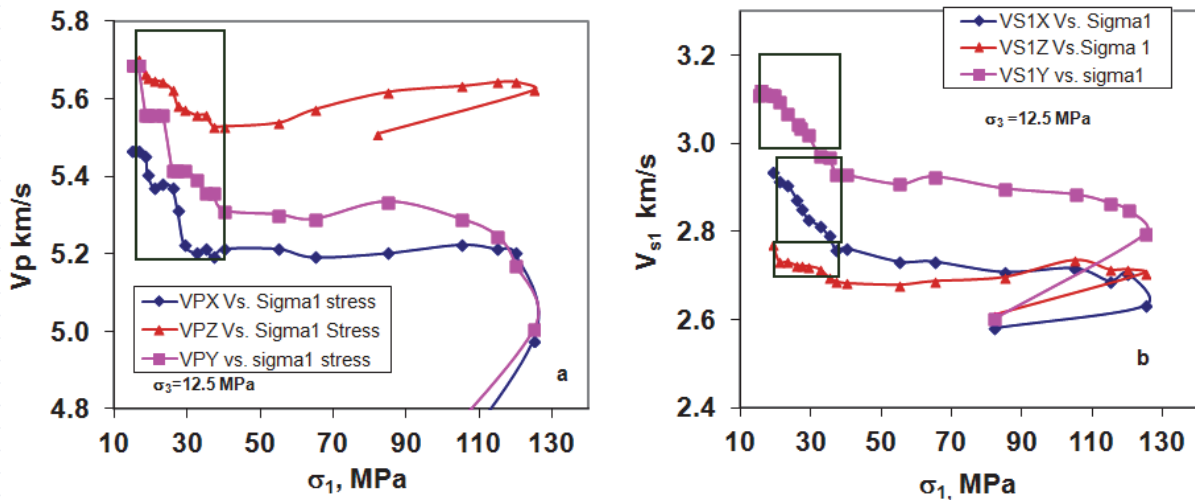


Figure 92: Evolution of (a) V_p and (b) V_{S1} along the X, Y and Z axes of Specimen L7 during heating and differential stress increments

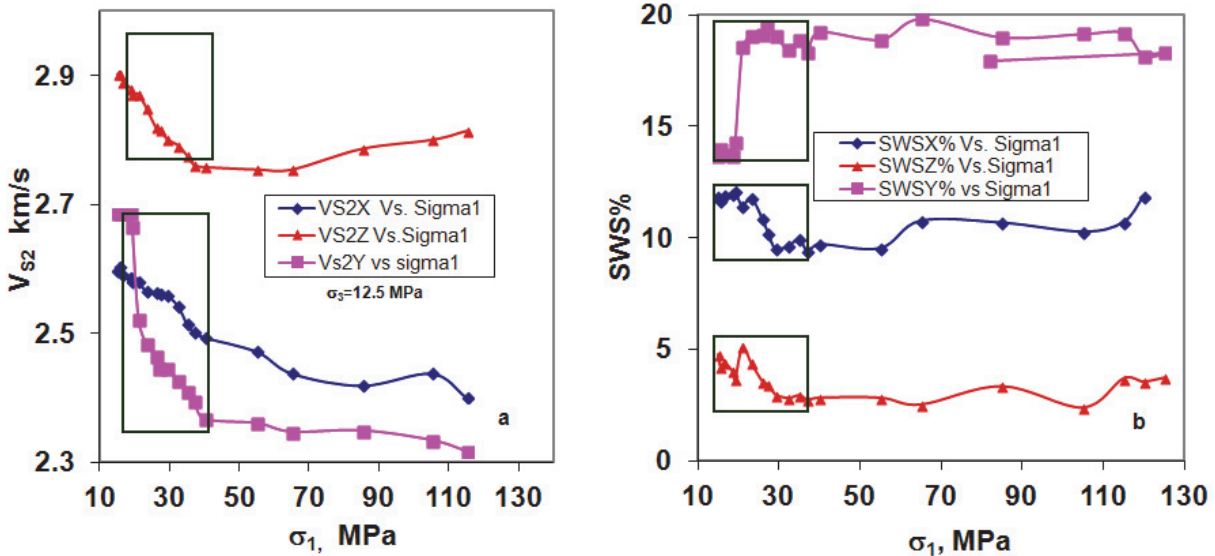


Figure 93: Evolution of (a) V_{S2} along the X, Y and Z axes of Specimen L7 during heating (value shown with the green rectangle) and differential stress increments and (b) shear wave splitting as a function of heating and thermal expansion.

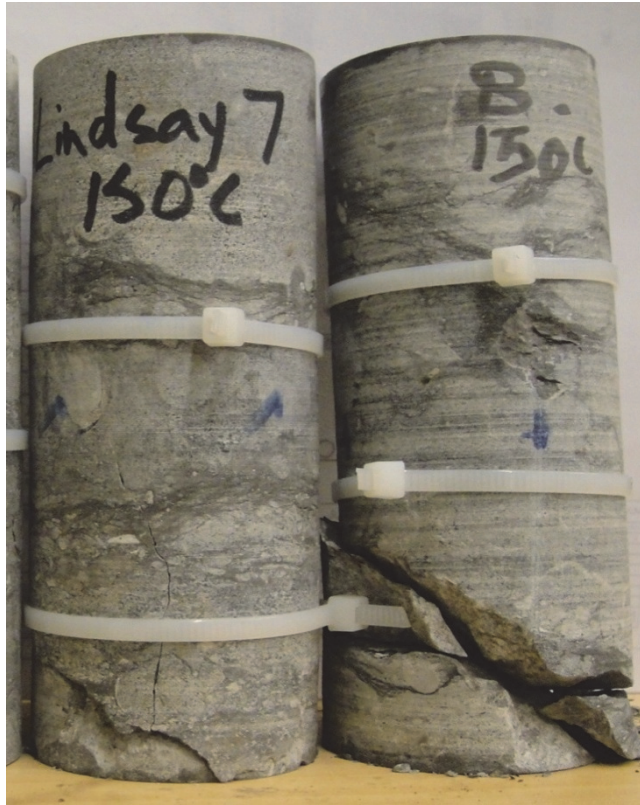


Figure 94: A photo of Specimens L7 and L8 after testing

Table 13 and figure 95 show the evolution of dynamic Young's modulus and Poisson's ratio during heating and loading up to the failure under constant temperature and confining pressure. Dynamic modulus shows a reduction along X,Y and Z axes in response to lateral sample expansion. E_{dY} shows highest reduction of 10 GPa and E_{dX} and E_{dZ} both show a reduction of 4 GPa as the temperature is raised to 150°C. The two horizontal axes do not reveal a similar reduction in E_d during the heating process, suggesting an anisotropic thermal expansion of the specimen. E_{dZ} increases during further loading whereas the other two lateral Young's modulus values (E_{dX} and E_{dY}) decrease as the vertical stress approaches the failure strength.

Table 13: Variation of dynamic elastic constants along three axes during heating up to 150 °C and as a function of vertical stress for Specimen L7

<i>Temp.</i>	<i>Vertical Stress</i>	<i>Ed, Z axis</i>	<i>νZ axis</i>	<i>Ed, Y axis</i>	<i>νY axis</i>	<i>Ed, X axis</i>	<i>νX axis</i>
°C	MPa	GPa		GPa		GPa	
25	15	54.7	0.33	56.72	0.32	51.95	0.33
30	15.58	54.96	0.33	56.91	0.32	52.04	0.33
42	16.54	54.58	0.34	56.79	0.32	51.81	0.33
50	18.6	54.29	0.33	56.25	0.31	51.64	0.33
60	19.2	54.11	0.33	55.94	0.32	51.35	0.32
70	20.97	53.49	0.34	53.42	0.33	50.92	0.32
80	23.2	52.86	0.34	52.41	0.33	50.61	0.33
90	25.9	52.48	0.34	51.29	0.33	50.02	0.33
100	27	52.37	0.34	50.83	0.33	49.47	0.33
110	29.19	52.06	0.34	50.6	0.33	48.81	0.32
120	32.4	51.69	0.34	49.53	0.33	48.24	0.32
130	35	51.14	0.34	49.12	0.33	47.54	0.33
140	37.1	50.68	0.34	48.33	0.34	46.83	0.33
150	40	50.57	0.34	47.34	0.33	46.44	0.33
150	55	50.48	0.34	46.9	0.34	45.68	0.33
150	65	50.71	0.34	46.93	0.33	45.13	0.34
150	85	51.49	0.34	46.68	0.34	44.54	0.34
150	105	52.37	0.34	46.13	0.34	45	0.34
150	115	52.28	0.34	45.46	0.34	44	0.34
150	120	52.22	0.34	45.26	0.33	43.99	0.34
150	125	51.97	0.34	43.3	0.33	41.82	0.33
150	82	50.05	0.34	37.22	0.31	35.74	0.31

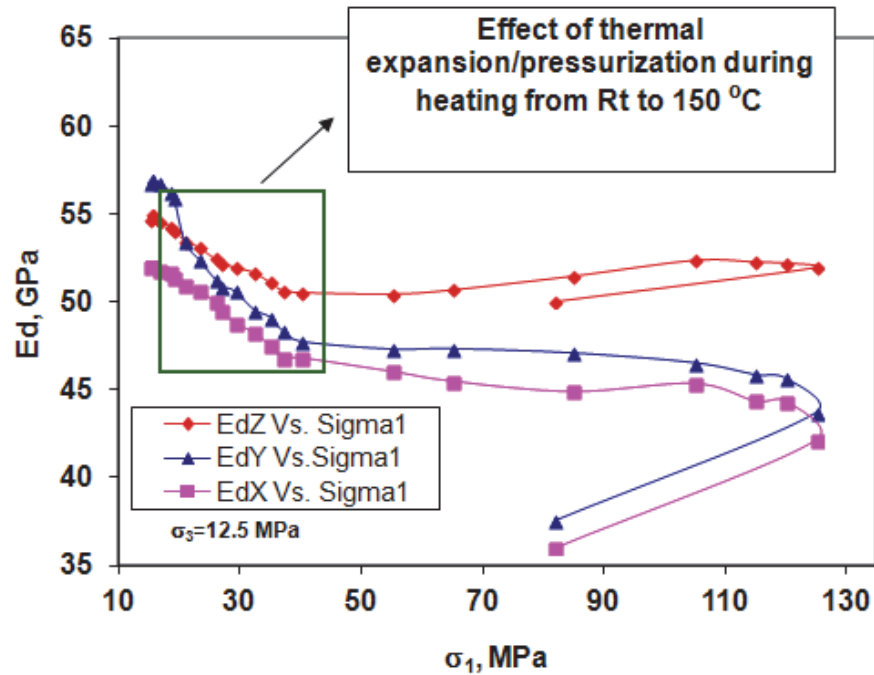


Figure 95: Evolution of moduli with differential stresses along X, Y and Z directions of Specimen L7

Figure 96 shows permeability and seismic velocity measured at hydrostatic stress under ambient temperature. The variation of permeability is also shown as a function of raised temperature and its consequential thermal pressurization. The variation of permeability as a function of differential stresses up to failure is shown to decrease initially, and then to increase prior to the failure. Further decrease of permeability as a function of differential stress increments (up to 55 MPa) occurred when axial stress caused further compaction of weak shaly partings. The load was increased from 50 MPa to 125 MPa, making the L7 specimen more permeable due to the formation of axial cracks. V_p measured along the horizontal directions (X and Y axes) for both specimens showed a decrease corresponding to axial stress and the development of microcracks parallel to the loading. Evolution of permeability for the specimens as a function of differential stresses follows a trend similar to what was observed previously at lower temperatures. Figure 96 shows the failure pattern for the L7 and L8 specimens.

The specimen experienced an additional 30 MPa of axial stress during the heating process, due to the thermal expansion of the specimen. This caused closure of microcracks and clogging of pore spaces due to throat effect. Permeability of the specimen further decreases as a function of differential stresses due to closure and compression of microcracks and pore spaces along σ_1 direction when differential stress increases up to 90 MPa. This evolution in permeability is confirmed by an axial decrease in seismic wave velocities along all three directions during the heating, and later by an increase along the axial loading direction (Figure 92 and 93).

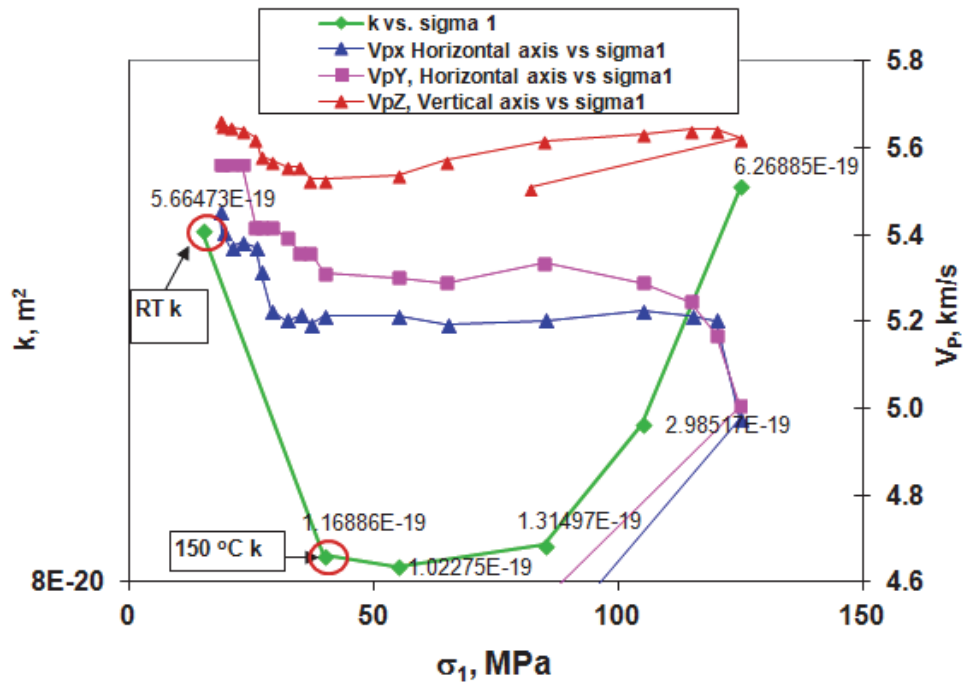


Figure 96: Evolution of permeability of Specimen L7 as a function of hydrostatic at ambient temperature, as a function of thermal stress measured at 150 °C temperature and differential stress increments

3.3.5 Specimen L8

Figure 97 shows the evolution of axial, diametral and volumetric strains with thermal stresses during heating of L8 specimen. Figure 98 shows the variation of axial, diametral and volumetric strain with temperature increments during heating process for the L8 specimen. The first cycle of heating of the specimen was carried out under constant axial displacement control in order to record axial thermal pressurization similar to Specimen L7. The sample experienced a thermal pressurization of 30 MPa when the temperature increased from ambient 22°C to 150°C (Figure 99). A diametral strain of 0.5% and a volumetric strain of 1% were registered. Specimen was cooled down overnight and was re-heated to 150°C under constant load control mode during the second cycle of heating. This was to measure the possible hysteresis and, to find out if the first thermal cycle had caused any permanent damage in the specimen.

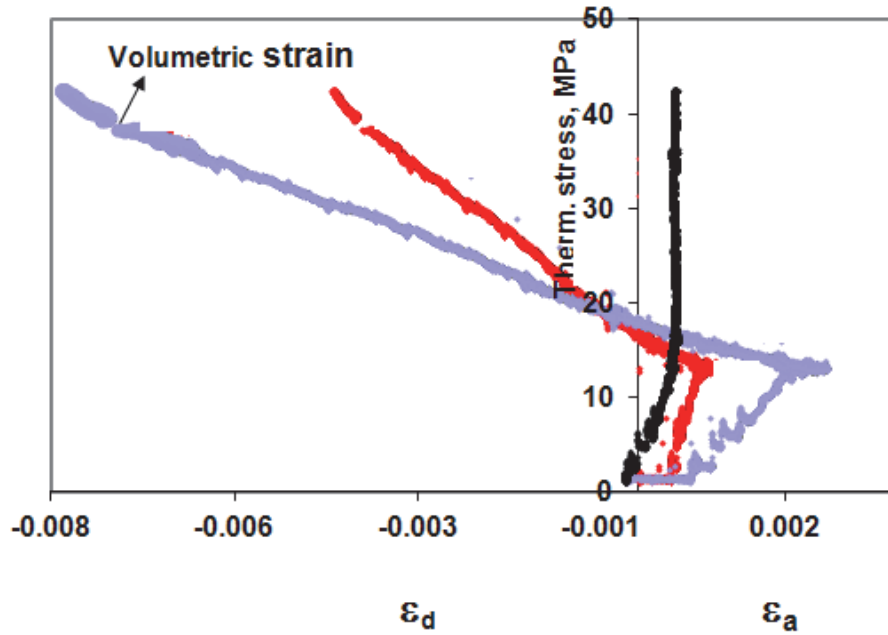


Figure 97: Stress-strain, thermal pressurization and volumetric strain plots of Specimen L8

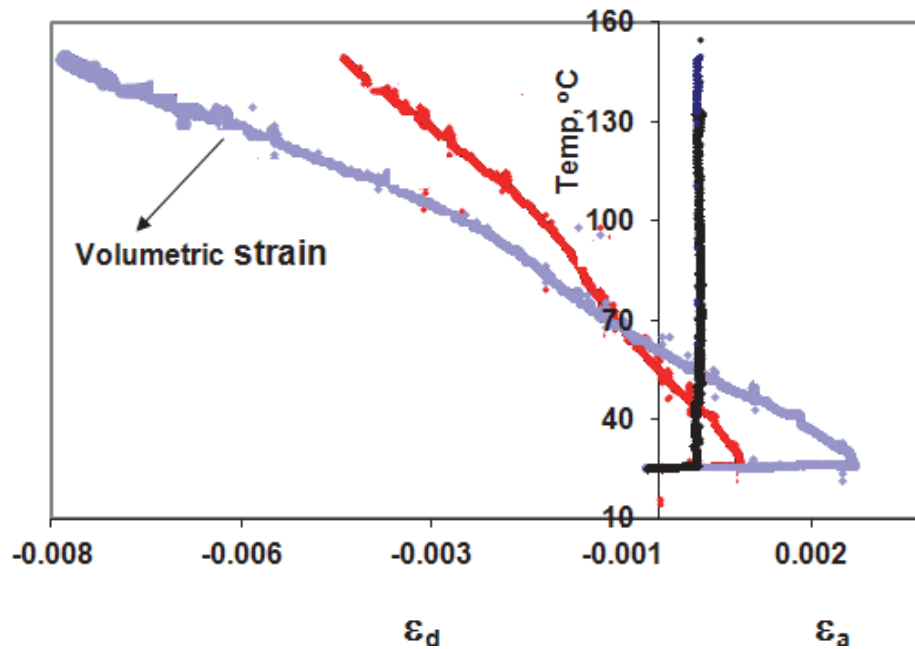


Figure 98: Axial, diametral and volumetric strain plots of Specimen L8 during in-situ heating under displacement control mode

Figures 99a and 100a show the evolution of seismic wave velocities due to thermal pressurization caused by heating of the L8 specimen to 150°C. Figure 100b shows also the variation of shear wave splitting as a function of thermal pressurization during the first cycle of heating. The effect of thermal expansion on seismic wave velocities in Cobourg limestone along the lateral directions (X and Y axes) is much stronger than what was measured in the axial direction, as the specimen is free to expand diametrically (Figure 102).

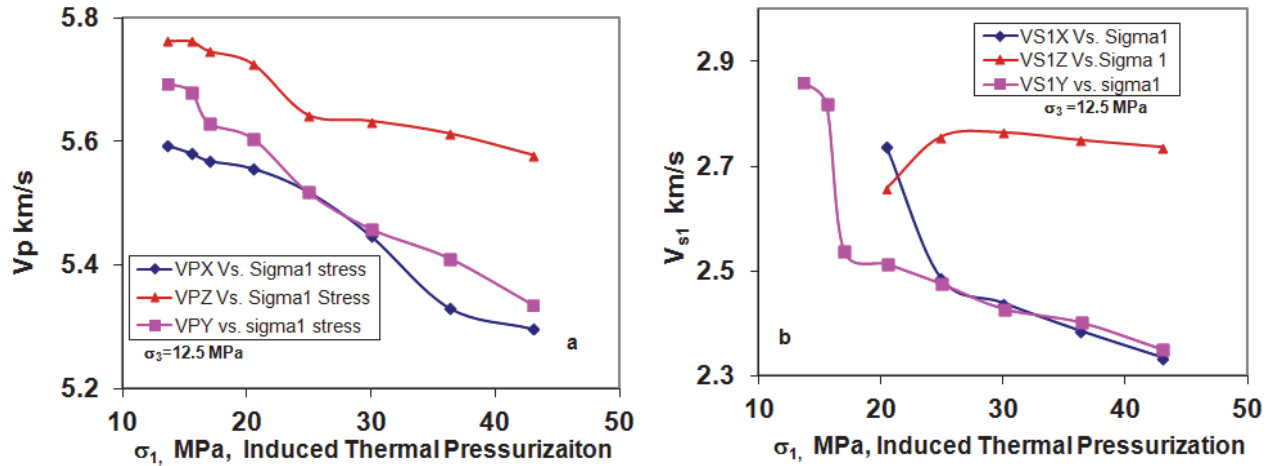


Figure 99: Evolution of (a) V_p and (b) V_{s1} along the X, Y and Z axes during heating of the L8 specimen up to 150°C

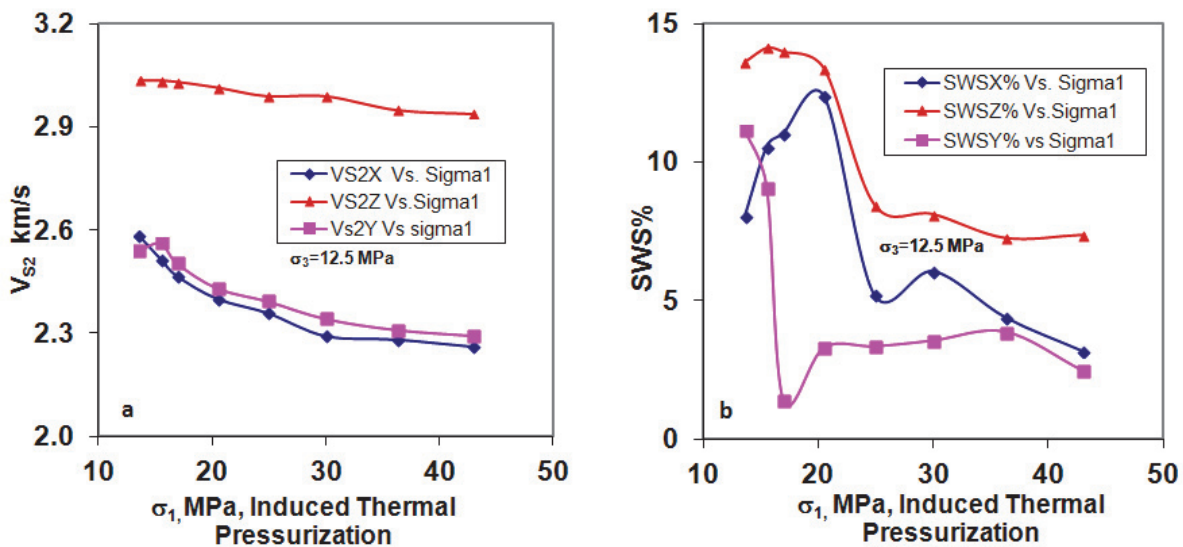


Figure 100: Evolution of (a) V_{s2} along the X, Y and Z axes as a function of thermal pressurization during the heating of Specimen L8 up to 150°C and (b) shear wave splitting as a function of heating

Table 14 and Figure 101 show the variation of dynamic elastic constants during first cycle of heating of L8 specimen to 150°C. Dynamic modulus shows a reduction along three axes of X, Y and Z in response to lateral sample expansion as the temperature is raised from 25°C to 150°C.

E_{dY} and E_{dX} show a similar trend of decreasing from 50 GPa to 38 GPa during the heating to 150°C. Dynamic Poisson's ratio decreases for X and Y axes showing a similar trend to that of dynamic Young's modulus whereas the latter for Z axis does not show such a trend as observed for X and Y axes.

Table 14: Variation of dynamic elastic constant along three axes during first cycle of heating up to 150°C for Specimen L8

Temp. °C	Vertical Stress MPa	E_d , Z axis GPa	ν_Z axis	E_d , Y axis GPa	ν_Y axis	E_d , X axis GPa	ν_X axis
25	13.6	55.49	0.34	50.4	0.35	49.99	0.35
30	15.5	55.27	0.34	50.03	0.36	48.94	0.35
50	16.95	55.16	0.34	44.55	0.37	47.5	0.36
70	20.5	54.84	0.34	42.97	0.38	45.91	0.36
90	24.9	55.75	0.33	41.69	0.38	41.36	0.38
110	30	55.85	0.32	40.08	0.38	39.5	0.38
130	36.3	54.92	0.33	39.14	0.38	38.38	0.38
150	43	54.42	0.33	38.02	0.38	37.28	0.38

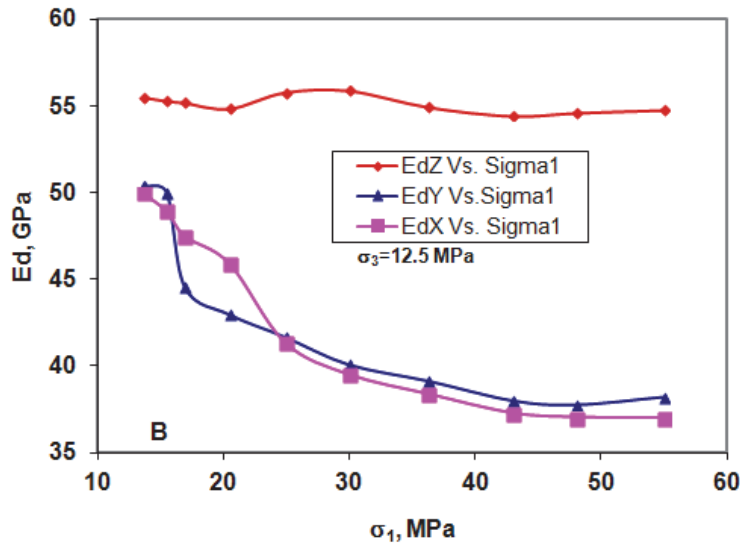


Figure 101: Evolution of moduli of Specimen L8 with temperature up to 150°C along X, Y and Z directions during first cycle of heating

Figure 102 shows the variation of permeability and V_P as a function of hydrostatic stress at ambient temperature (25°C) and as a function of induced thermal stress caused during heating. Permeability decreased after the heating. It is concluded that an overall volumetric strain increase makes the specimen more impermeable clogging the previously connected pathways. Expansion of the matrix and the calcite grains encourages the throat effect. The L8 specimen experienced an additional 30 MPa of axial stress during heating. Seismic wave velocity reduction and consequently reduction of E_d especially along lateral direction is a good indicator of sample expansion and deterioration of specimen's stiffness.

In this experiment, the same Specimen L8 was used for the second cycle of heating without removing it from the cell. The specimen cooled down overnight to 44°C from the previous cycle of heating under ambient pressure. In second cycle of heating, the MTS axial actuator was set to constant load control mode to allow the specimen to expand axially as well. The specimen was loaded hydrostatically up to 12.5 MPa of stress.

A permeability test was performed to obtain a new permeability value at hydrostatic stress levels at an ambient temperature of 45°C. The heater was then turned on to heat up the specimen to 150°C at the constant rate of 0.8 °C/min. Seismic wave velocities were measured along three axes at an interval of 10°C during the heating process.

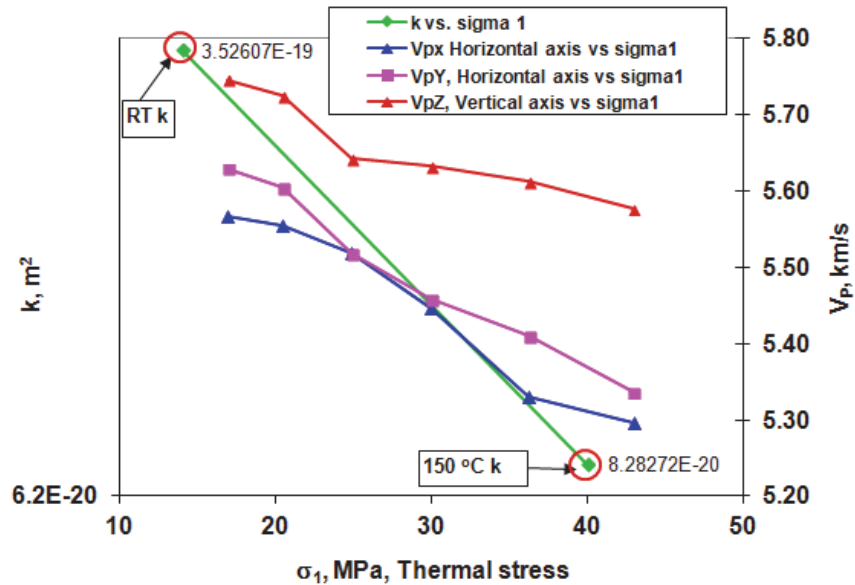


Figure 102: Evolution of permeability of Specimen L8 as a function of thermal stress

Figure 103 shows the evolution of axial, diametral and volumetric strain as a function of temperature under hydrostatic stress. The axial expansion of the specimen was permitted during the heating process. It can be observed that the specimen has expanded axially up to 0.14%, and experienced diametral strain of 0.5% and a total volumetric strain of 0.92% in the second cycle of heating.

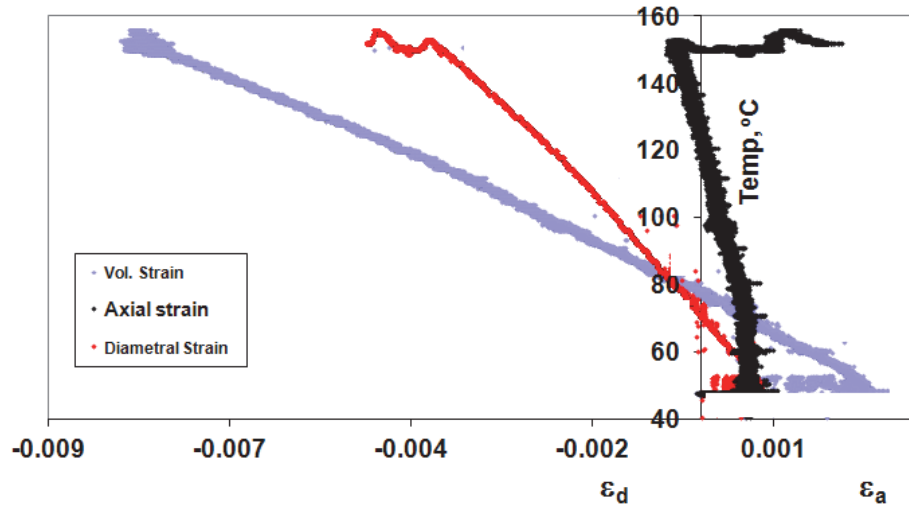


Figure 103: Axial, diametral and volumetric strains of Specimen L8 during heating up to 150 °C under load control mode

Figure 104 shows the axial, diametral and volumetric strains as a function of axial stress for the L8 specimen. The specimen has a failure strength of 135 MPa, experiencing an elasto-plastic type failure with an axial strain of 0.45%, lateral strain of 0.58%, and a volumetric strain of 1% at failure which includes the total volumetric strain (during heating and loading). The initial, flat section of the volumetric strain curve shows that the specimen undergoes 1% of volumetric strain during the heating process without causing any thermal pressurization, as the axial loading mode was changed to load control. This also shows that the specimen experiences almost identical amounts of volumetric strain in the second cycle of heating up to 150°C. This suggests that the specimen has accumulated some thermal damage as a result of first cycle of heating and cooling. Analysis of seismic wave velocities and dynamic elastic constants in the second cycle, and its comparison with the first cycle, shows that thermal cycle seems to be a reversible within the used temperature range.

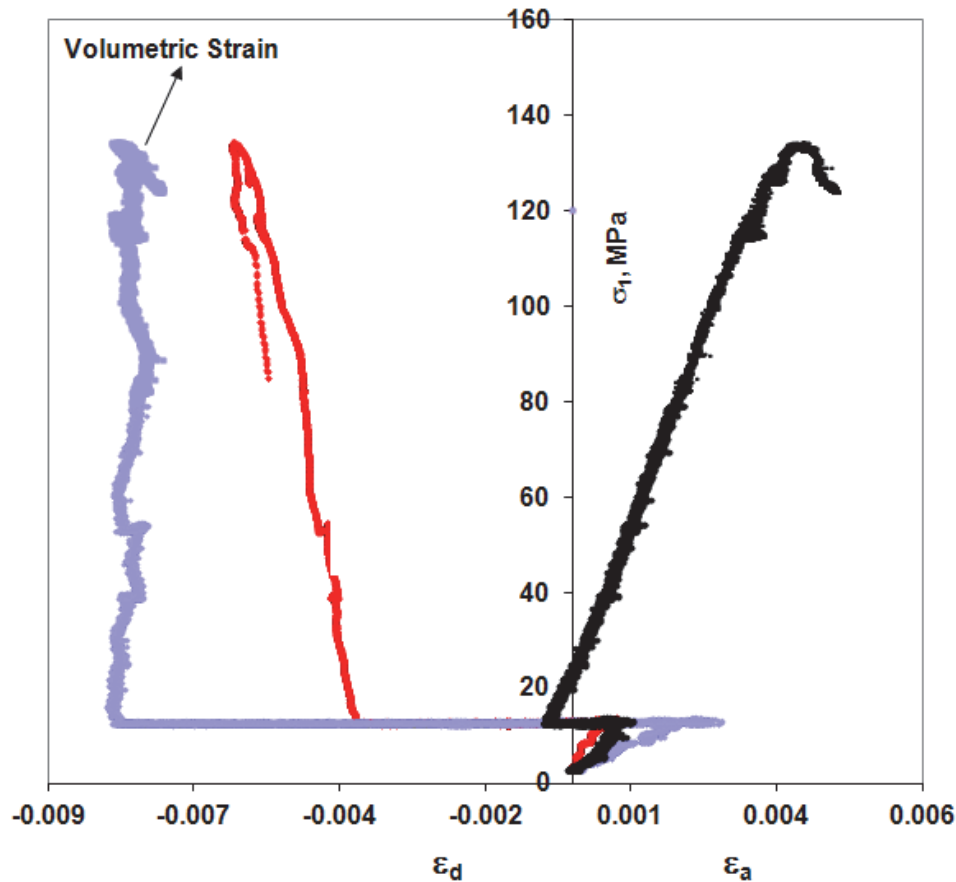


Figure 104: Axial, diametral and volumetric strain plots of Specimen L8

Figures 105 and 106 show the evolution of seismic wave velocities as a function of heating up to 150°C under constant lateral stress and constant axial force control (axial expansion is not restricted) during the second cycle of heating. Both velocities decrease as the temperature increases to 150°C. The specimen is allowed to expand axially and diametrically during the heating. The figures also show the variation of seismic wave velocities as a function of differential stress up to failure. It is evident that V_{PZ} , V_{S1Z} , and V_{S2Z} increase with initial increments of axial stresses, whereas V_{PX} , V_{PY} , V_{S1X} , V_{S1Y} , V_{S2X} and V_{S2Y} do not show an increase as a function of axial stress. Figure 108b shows the variation of shear wave splitting (SWS) as a function of the initial stage of heating, and as a function of axial stress increments. During second cycle of heating wave splitting increases from 7% to 14%, suggesting that the axial thermal expansion favours ZX axial plane direction. This anisotropy is suppressed during loading stages back to 5%. In the contrary diametral splitting shows an increase from 3% to 14% during loading stages up to failure, suggesting formation of axial planes associated with axial stress increments especially closer to the failure strength. Figures 107 to 109 show the variation of V_P , V_{S1} and V_{S2} as a function of axial expansion of the L8 specimen, as the temperature increases to 150°C.

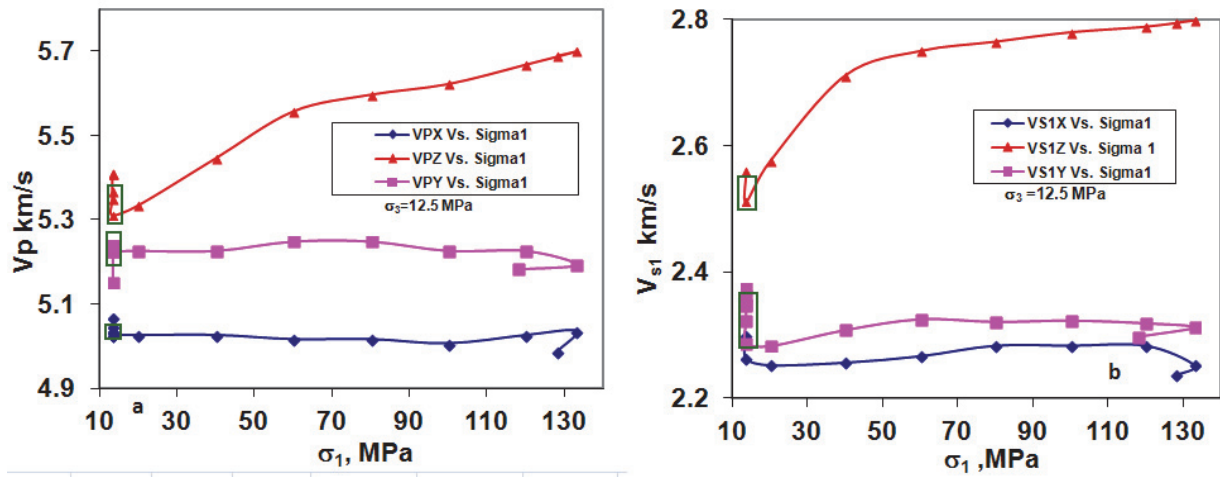


Figure 105: Evolution of (a) V_p and (b) V_{s1} along the X, Y and Z axes during heating and differential stress increments. Points in the boxes show the effect of thermal heating

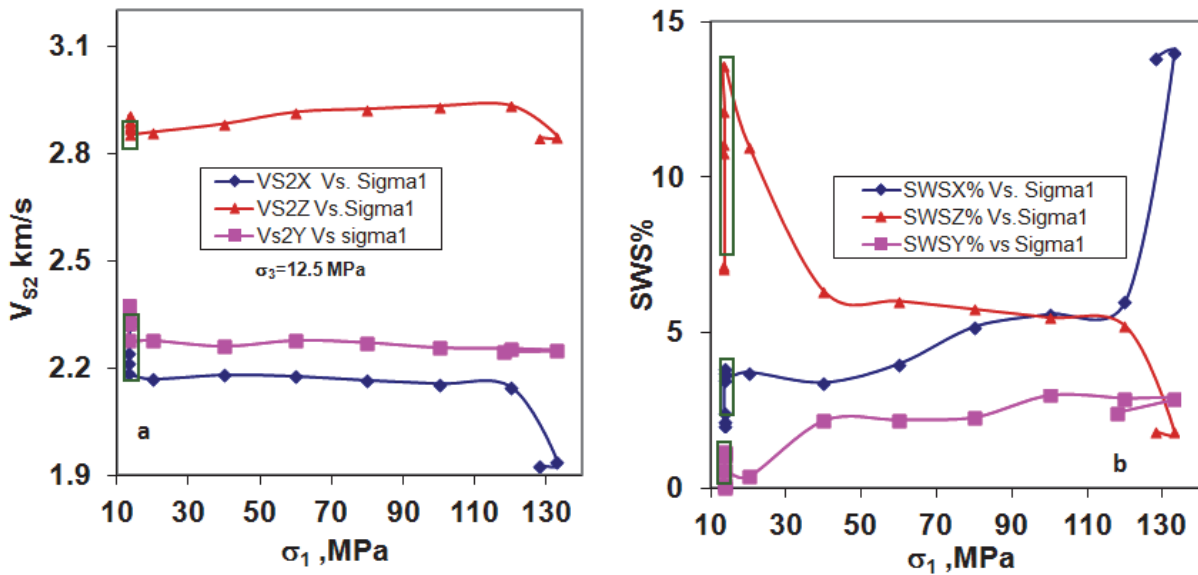


Figure 106: Variation of (a) V_{s2} along the X, Y and Z axes as a function of thermal pressurization during the heating of the L8 specimen up to 150°C and (b) shear wave splitting as a function of heating. Points in the boxes show the effect of thermal heating

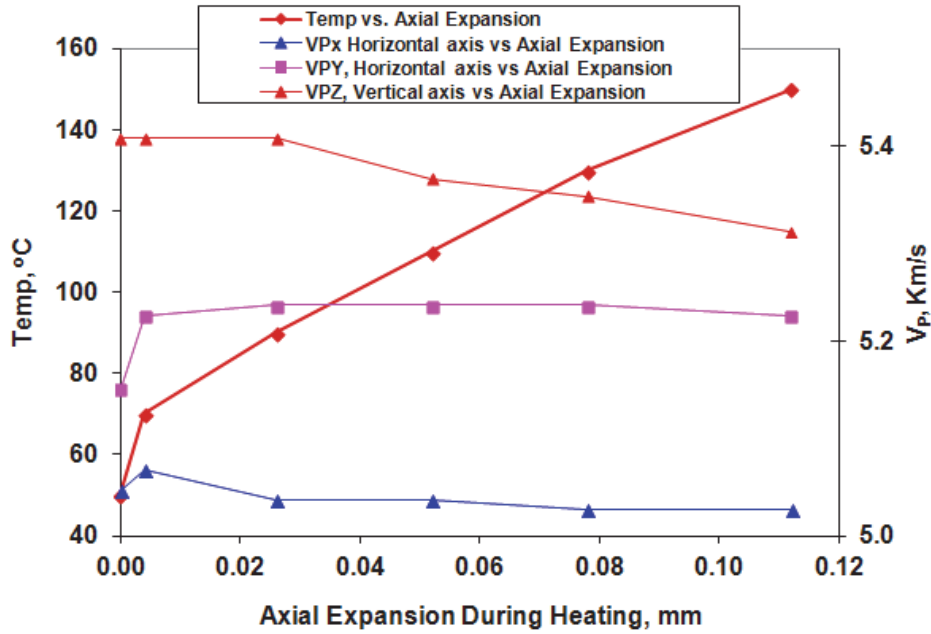


Figure 107: Variation of V_P as a function of axial expansion caused by heating (thermal expansion) for Specimen L8

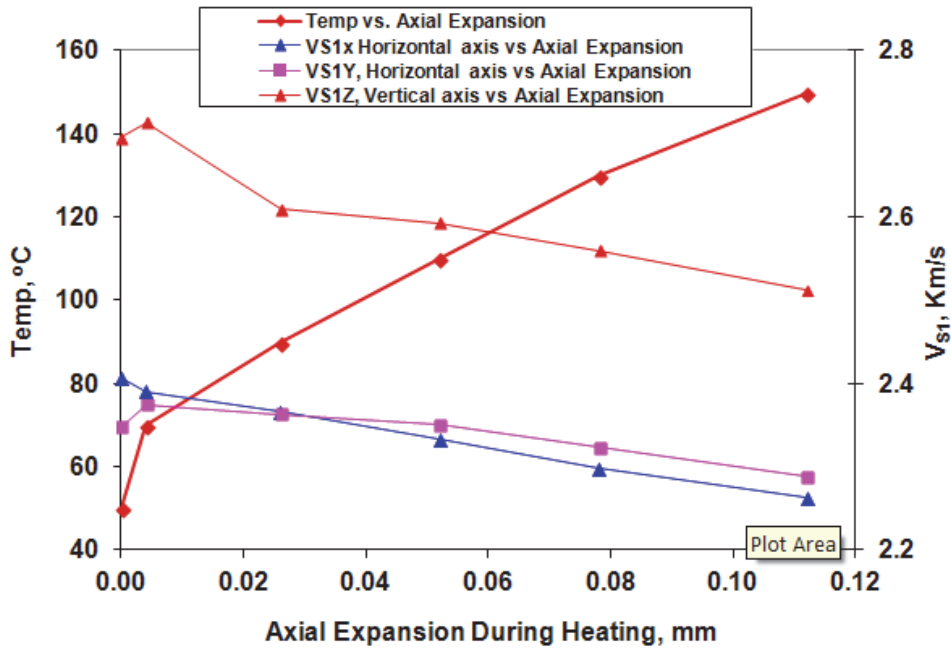


Figure 108: Variation of V_{S1} as a function of axial expansion caused by heating (thermal expansion) for Specimen L8

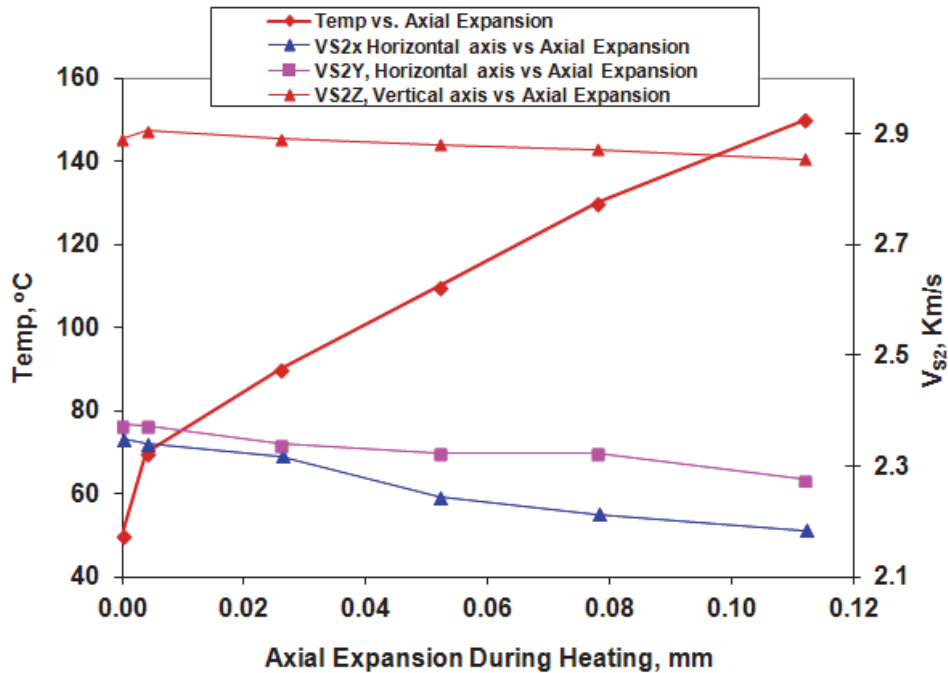


Figure 109: Variation of V_{S2} as a function of axial expansion caused by heating (thermal expansion) for Specimen L8

Heating of the specimen at 12.5 MPa of hydrostatic stress causes a volumetric expansion of 1%, which is responsible for the gradual decrease in seismic wave velocities especially the shear wave velocities. Axial expansion of the specimen affects V_{PZ} more than V_{PX} and V_{PY} , and during heating, V_{S1Z} is also more affected than V_{S1Y} and V_{S1X} in this experiment. This phenomenon could be due to the opening of weak shaly partings that are aligned perpendicular to the Z axis and run parallel to the X and Y axes.

Table 15 and Figure 110 show the variation of dynamic elastic constants during the second cycle of heating of L8 specimen up to 150°C and during loading up to failure. Dynamic modulus decreases along three axes of X, Y and Z in response to lateral sample expansion as the temperature is raised from 50°C to 150°C. E_{dY} and E_{dX} show a similar trend of decreasing from 39 GPa to 35 GPa during the process of heating whereas E_{dZ} decrease from 52 to 48 GPa as the temperature is raised from 50 °C to 150°C. Comparison of the E_d calculated for 1st and 2nd cycles of heating at 150 ° C (Table 13, third row with Table 14, first row) indicates that L8 specimen has experienced a permanent thermal damages showing that E_{dZ} dropped from 55.16 GPa to 52.43 GPa and E_{dX} decreased from 47.50 GPa to 39.12 GPa and E_{dY} decreased from 44.55 GPa to 38.87 GPa. Higher lateral decrease of dynamic Young's modulus in comparison to axial dynamic Young's modulus indicates that a higher permanent thermal damage was experienced in L8 specimen since it was allowed to expand laterally twice. E_{dZ} increases from 48.78 to 55.45 GPa when the load reaches 120 MPa prior to the peak strength (130 MPa) due to closure of fractures (Figure 110).

Table 15: Variation of dynamic elastic constant along three axes during 2nd cycle of heating up to 150 °C under load control (axial expansion was allowed) for Specimen L8

Temp. °C	Vertical Stress MPa	Ed, Z axis GPa	ν Z axis	Ed, Y axis GPa	ν Y axis	Ed, X axis GPa	ν X axis
50	13.5	52.43	0.36	38.87	0.37	39.12	0.32
70	13.5	52.94	0.36	39.37	0.37	38.81	0.32
90	13.5	51.12	0.36	38.74	0.37	38.09	0.33
110	13.5	50.57	0.37	38.32	0.38	36.56	0.32
130	13.5	49.87	0.37	37.94	0.38	35.65	0.33
150	13.5	48.78	0.38	36.7	0.38	34.75	0.33
150	20	49.92	0.38	36.64	0.38	34.4	0.32
150	40	52.7	0.38	36.77	0.38	34.61	0.32
150	60	54.19	0.38	37.28	0.38	34.69	0.32
150	80	54.68	0.38	37.13	0.38	34.76	0.33
150	100	55.14	0.38	36.92	0.38	34.62	0.33
150	120	55.45	0.38	36.83	0.38	34.52	0.33
150	133	54.36	0.4	36.6	0.38	31.23	0.34
150	118	54.2	0.39	36.32	0.38	30.82	0.34

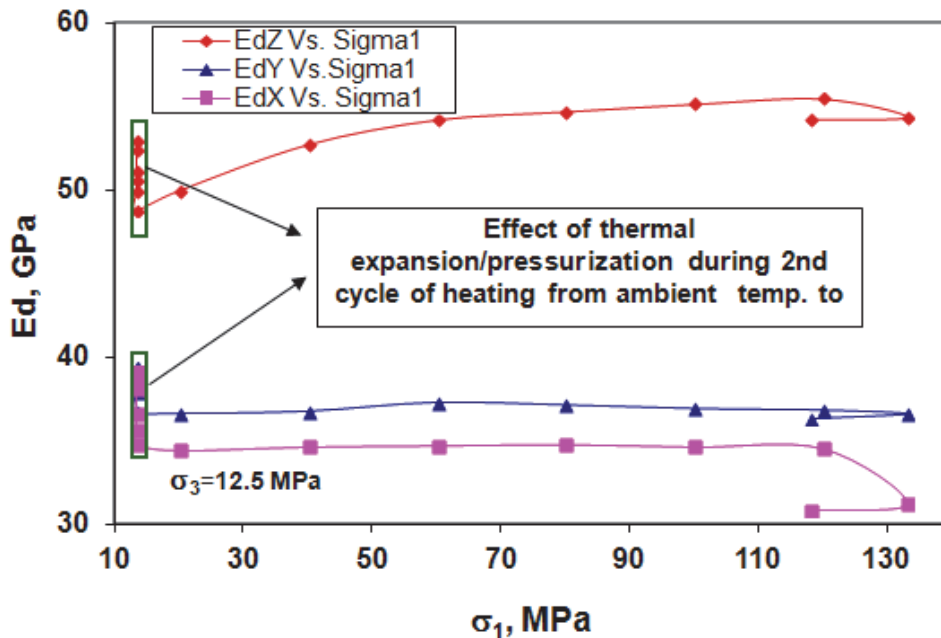


Figure 110: Evolution of moduli of Specimen L8 with temperature increase to 150 °C along X, Y and Z directions during 2nd cycle of heating under load control

Figure 111 shows the variation of permeability and V_P as a function of hydrostatic stress at ambient temperature. The figure also shows the variation of permeability and V_P as a function of raised temperature and differential stresses. Permeability was found to decrease after heating due to thermal expansion of the specimen. The permeability as a function of differential stress shows an initial decrease when axial stress reached 90 MPa, and then increases prior to failure. V_P decreases during the heating of the specimen along all three directions. V_{PZ} shows a marked increase as axial stresses reached yield strength whereas V_{PY} and V_{PX} show a decreasing trend prior to failure strength, responding to formation of microcracks parallel to the loading direction. Increase in permeability after 90 MPa of axial stress is compatible with decreasing trend in lateral compression wave velocity.

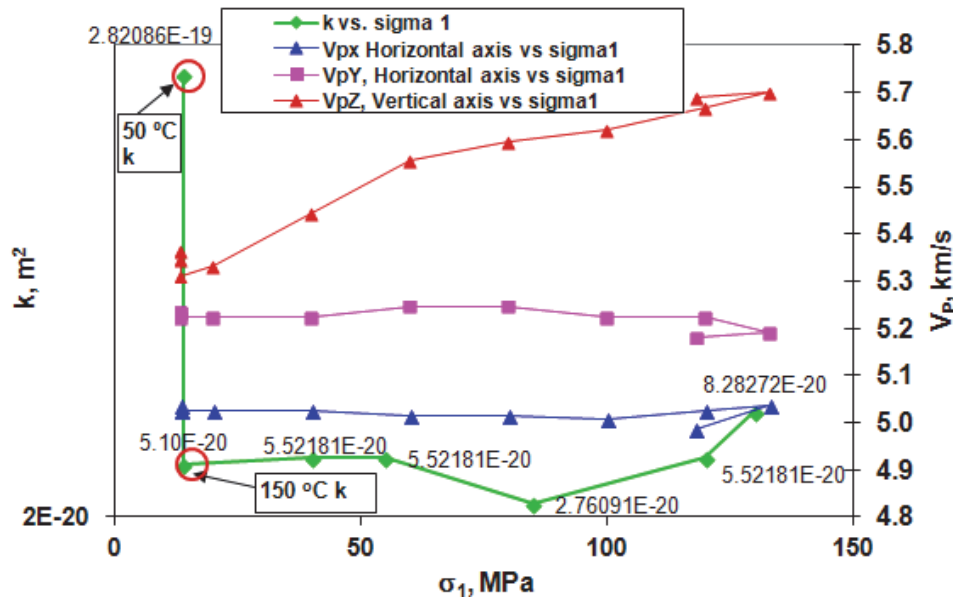


Figure 111: Evolution of permeability and V_P of Specimen L8 as a function of differential stress, tested at ambient temperature and as a function of increased temperature

3.3.6 Thermal Expansion Coefficient of Cobourg Limestone

Figure 112 shows the variation of the thermal expansion coefficient (α in 10^{-5} K^{-1}) with temperature for Specimens L9 and L5 during heating process up to 100°C as calculated according to:

$$\alpha = \frac{\Delta d / d_0}{\Delta T} \quad (6)$$

Where Δd is the diameter change of the sample, d_0 is the initial sample diameter and ΔT is the temperature interval in Kelvin. Figure 113 shows the same variation for Specimen L8 for 1st and 2nd cycle of heating. As it is shown in both figures Cobourg limestone begins to expand when the in situ temperature reaches 50°C . The L8 specimen during the second cycle of heating shows that when the temperature reaches 75°C diametral expansion is reactivated. This phenomenon can be related to hysteresis in the thermal cycle and the thermal damages that this specimen had experienced during the first cycle of heating. Similar results have been reported by Benavente et al. (2008) on cyclic heating-cooling of building stones. They

concluded that the mineral expansion operates in different temporal and spatial scales and the stresses generate by the mismatch of thermal expansion rates operates mainly at the grain scale in the long term and therefore, the consideration of bulk thermal expansion is not as important as the consideration of the processes that the rock undergoes at the grain scale. Figure 114 shows the variation of diametral strain as a function of temperature increments up to 100°C for the L5 and L9 specimens. Figure 115 shows the same for the L8 specimen (1st and 2nd cycles of heating) up to 150°C. The slope of the curves shows an average thermal expansion coefficient in the range of 3 to 3.5 × 10⁻⁵ K⁻¹ and shows that it is more or less a linear relationship.

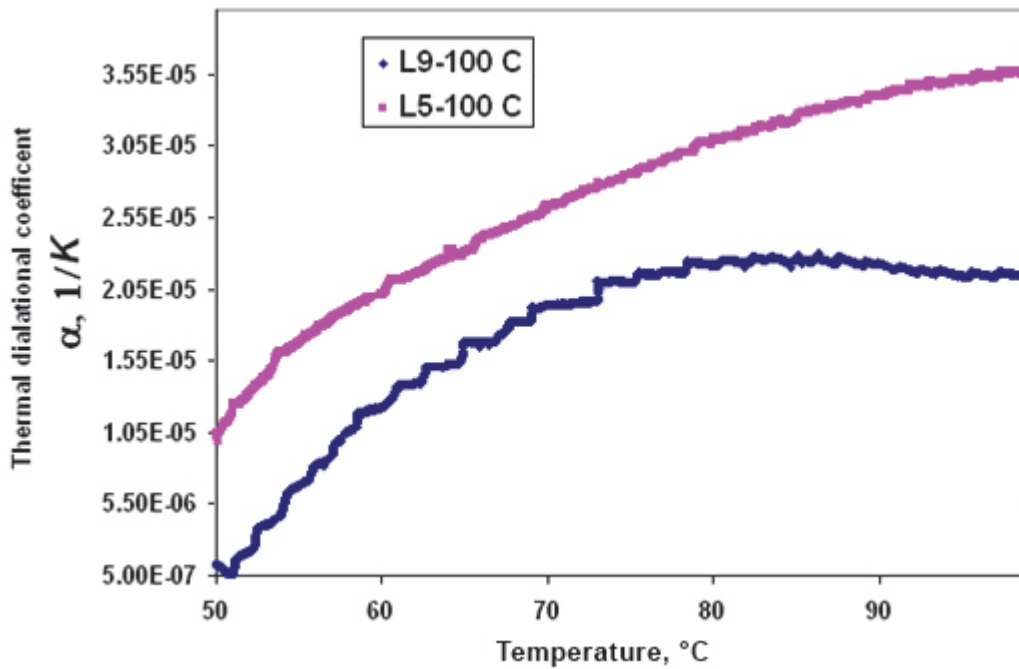


Figure 112: Variation of α (1/K) with in situ heating temperature for Specimens L5 and L9

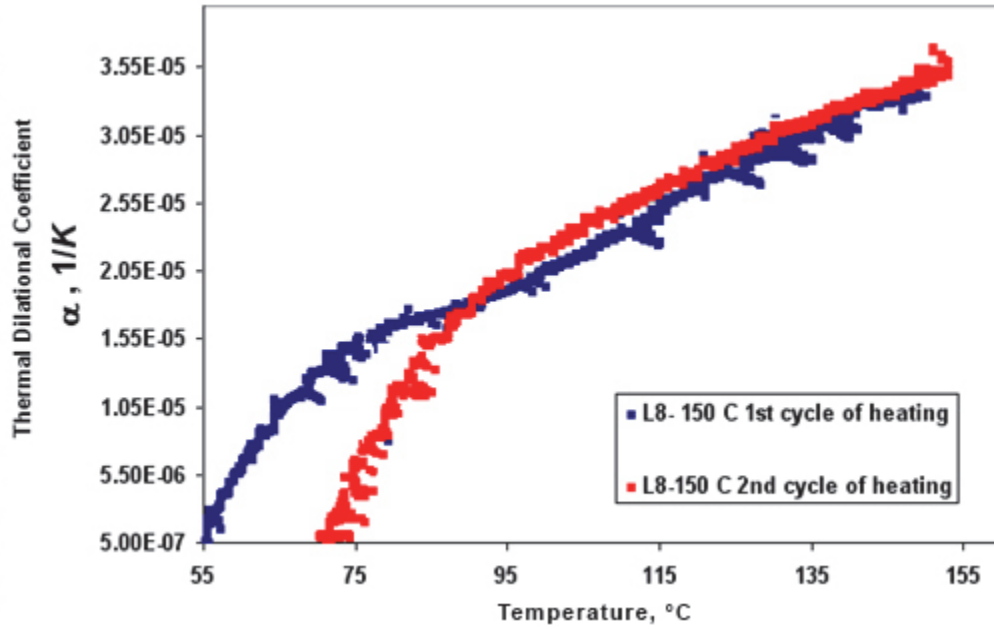


Figure 113: Variation of $\alpha(1/K)$ with in situ heating temperature for Specimen L8 during the 1st and 2nd cycle of heating.

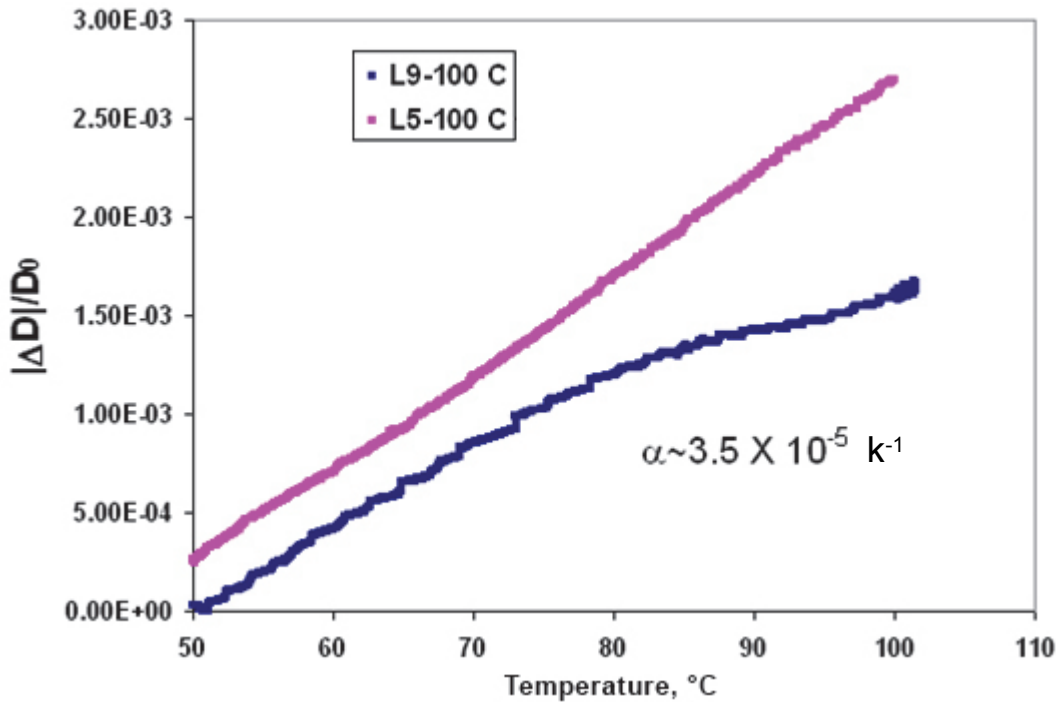


Figure 114: Thermal expansion curves for Specimens L5 and L9

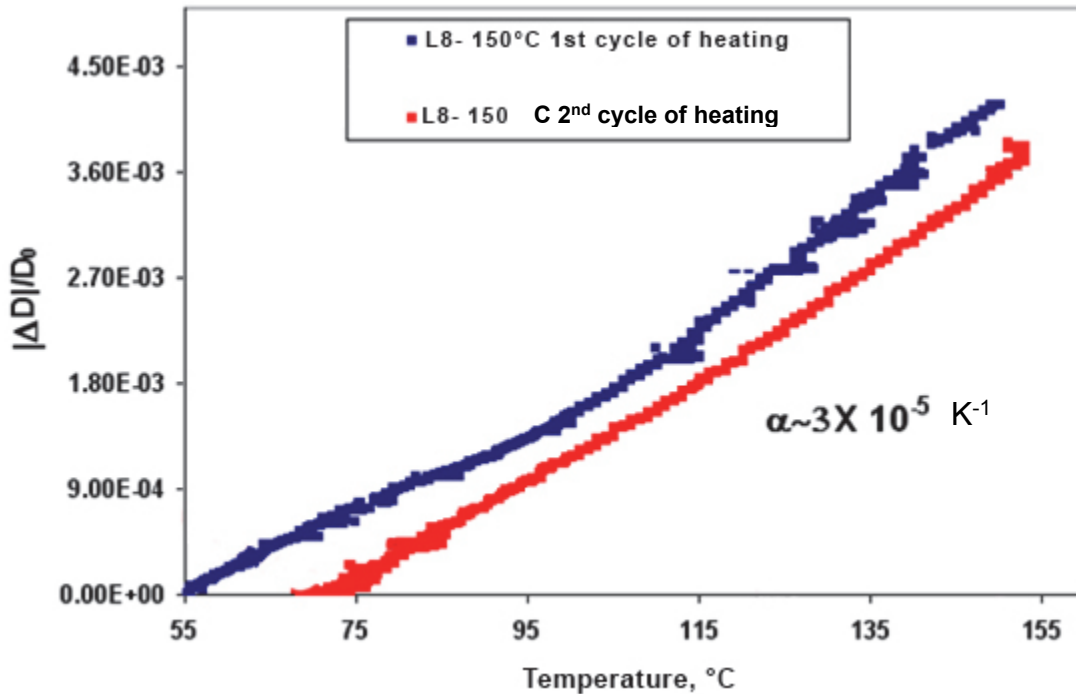


Figure 115: Thermal expansion curves for L8 for the 1st and 2nd cycles of heating up to 150°C

3.4 DISCUSSION OF PHASE 2 RESULTS

The Phase 2 study consists of three groups of experiments as shown in Table 4. The first series concerns physical property measurements, using dry and saturated samples. The second series includes uniaxial compressive strength tests on dry and saturated Cobourg limestone for non-heat treated samples, and heat treated at 50°C, 100°C and 150°C. The third set of experiments was carried out to measure the axial, diametral and volumetric strain, ultrasonic wave-velocity, static and dynamic elastic constants and permeability changes at ambient and elevated temperatures, at hydrostatic condition and at differential stresses up to failure.

The results suggest that Cobourg limestone has a porosity of about 0.5 to 1%, and a dry and saturated density of 2.55 and 2.66 g/cc, respectively. This rock shows a fair amount of heterogeneity in terms of its texture. The majority of the cored specimens are characterized with random/irregular sizes and shapes of clay pockets and discontinuous shaly partings that are also responsible for its anisotropic behaviour at sample scale. In the Phase 2 study, two axial LVDTs were used to record the total axial deformation, rather than using strain gauges. The latter can only capture the deformational responses locally. The UCS tests for saturated samples suggest that the limestone has an average saturated uniaxial compressive strength of 63 MPa. The saturated specimens also show an average Young's modulus of 26 GPa, with standard deviation of 0.4 GPa. The average dry UCS for this rock for limited untreated specimen is 82.7 MPa, with a standard deviation of 1.4 MPa. The average dynamics Young's modulus for dry specimens is 28 GPa, with a standard deviation of 4.2 GPa. The UCS and elastic modulus values for both dry and saturated appear to be significantly less than those

obtained during the Phase 1 testing. Such discrepancies could be attributed to sampling at different locations and the drying of Phase 1 samples in the core storage facility (over 20 year old).

The effect of pre-heating up to 150°C seems not to affect the dry UCS. UCS for 50°C treated specimens (three specimens) showed an average UCS value of 89.4 MPa, with a standard deviation of 23 MPa, characterized by an average Young's modulus of 29.6 GPa, with a standard deviation of 6.3 GPa. UCS for 100°C treated specimens (three specimens) showed an average UCS value of 91.4 MPa, with a standard deviation of 14 MPa. These specimens showed an average Young's modulus value of 34.4 GPa, with a standard deviation of 3.2 GPa. The three 150°C treated specimens showed an average UCS value of 87.6 MPa, with a standard deviation of 11 MPa and an average Young's modulus value of 23.7 GPa, with a standard deviation of 1.7GPa.

Figure 116 shows the comparative stress-strain curves for selected specimens tested under THM conditions (Table16). Specimens tested at 100°C (L5 and L9) and 150°C (L7 and L8) show a higher average failure strength of 132 and 128 MPa, compared to the rest of the specimens tested under RT (103 MPa), 50°C (92 MPa). The 150°C specimen (L7) experienced the highest level of axial and diametral strain, mainly due to the fact that it was heated more than other specimens. A thermal stress of 40 MPa was registered for the L7 specimen, whereas 100°C resulted in a thermal stress of 33 MPa, both starting from 14 MPa of axial stress. Table 16 shows the triaxial compressive strength; quasi-static Young's modulus (E_t) and Poisson's ratio of all the specimens tested at room temperature and elevated in situ temperature. Specimen L8 (2nd cycle of heating) shows highest E_t of 38 GPa and L4 specimen shows lowest E_t of 17.9 GPa. A constant thermal stress rate of 0.22 MPa/°C was observed for Cobourg limestone for specimens heated up to 100 and 150°C. The heating procedure was kept consistent for all 6 specimens that were heated in-situ, i.e., under a constant confining pressure (12.5 MPa) and a constant heating rate of 0.8°C/min under constant axial displacement control mode (axial strain was restrained by keeping axial actuator on hold position after applying 12.5 MPa of axial load). 100°C and 150°C specimens show brittle type of post failure stress-strain curves and show higher quasi-static Young's modulus and are characterized with stable post heating seismic wave velocities up to failure probably due to dehydration effect caused by heating.

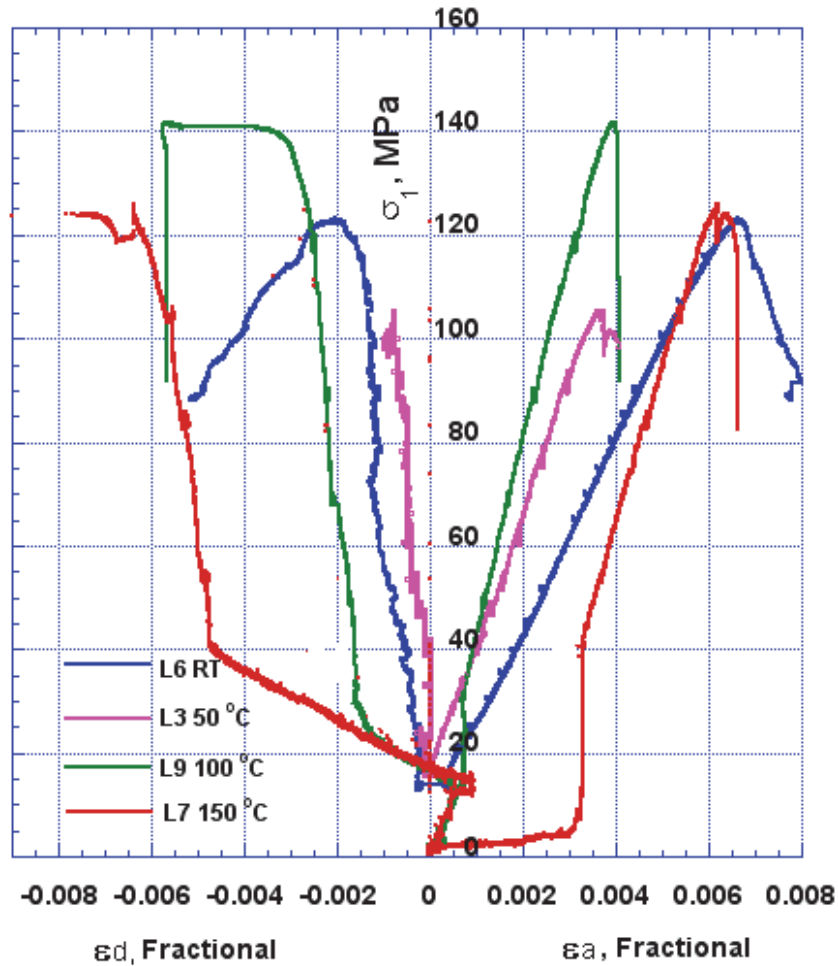


Figure 116: Stress-strain plots for RT, 50 °C, 100 °C and 150 °C specimens tested under coupled THM

Table 16: The compressive strength, Young's modulus and Poisson's ratio for specimens tested at ambient and elevated temperatures under constant pressure of 12.5 MPa

Sample Name	Temp °C	σ_1 Failure MPa	E_t Static GPa	Poisson's Ratio
6b	RT	122	19	0.35
L3	50	104	19.4	0.28
L4	50	80	17.9	0.21
L9	100	140	37	0.3
L5	100	121	30	0.16
L7	150	124	31	0.19
L8(II)	150	133	38	0.16

The L8 specimen was used for a second cycle of heating under constant load control in order to evaluate a global volumetric strain as a function of heating up to 150°C. In this experiment, L8

specimen was allowed to expand axially as well. It was found that the L8 specimen experienced volumetric expansion during the second cycle of loading, with the exception that it was free to expand axially during the second round of heating. The thermal dilation coefficient is calculated to be in the range of 3 to $3.5 \times 10^{-5} \text{ } ^\circ\text{K}^{-1}$. A linear thermal expansion curve is observed in plotting the diametral strain against the temperature increments for the 100 and 150°C heated specimens. Figure 117 shows the effect of in-situ heating on compression wave velocity along the vertical axis (Z) for RT and specimens thermally treated up to 150°C . The 100 and 150°C specimens experienced the highest level of velocity reduction along Z directions. V_{PX} and V_{PY} both show the highest level of velocity reduction due to the maximum lateral expansion experienced (Figure 120).

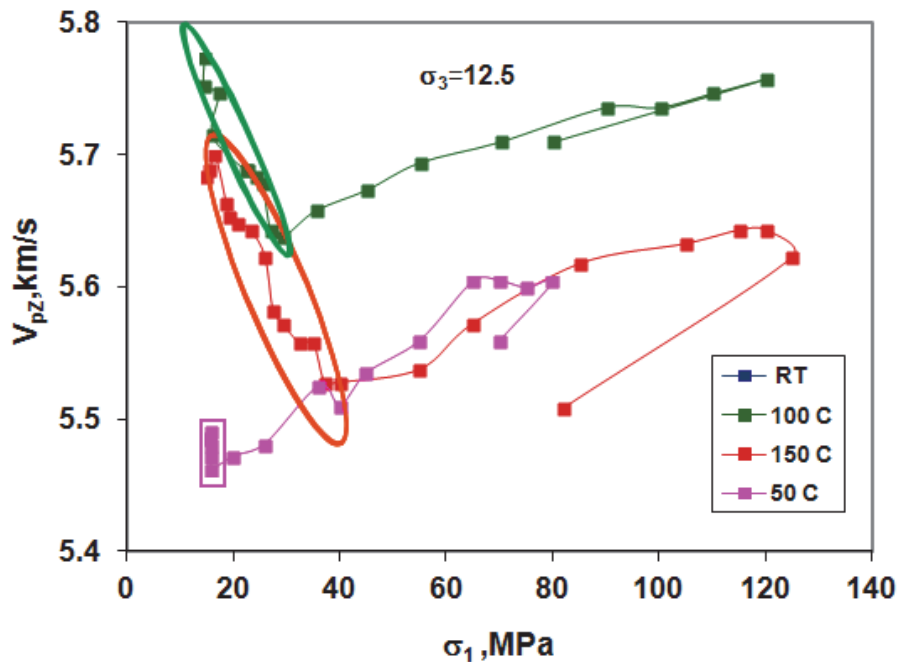


Figure 117: Variation of V_{PZ} (compression wave along vertical direction) for RT, 50°C , 100°C and 150°C during in-situ heating. Points in the box and oval circles show the effect of thermal heating

Figure 118 shows the variation of compressional wave velocities as a function of in situ heating and differential stresses for Z axis for RT and in-situ heated specimens and Figure 119 shows the variation of shear wave velocities for the same direction regarding the same specimens. 150°C and 100°C specimens are characterized by larger reduction of S_{1Z} shear wave velocities, whereas RT specimen shows higher values of S_{1Z} . Shear wave velocities measured along vertical axis show an increasing trend during loading stages for all specimens. Figures 120a and 120b show the shear wave velocities, S_1 and S_2 along X axis. Maximum thermal expansion along lateral directions caused a maximum shear wave velocity reduction for the 150°C specimen, as shown by values within the red oval in Figure 120. A further decrease in lateral shear and compression waves as a function of increased differential stresses can be related to the generation/nucleation and growth of axial microcracks and micro damages in response to axial stresses.

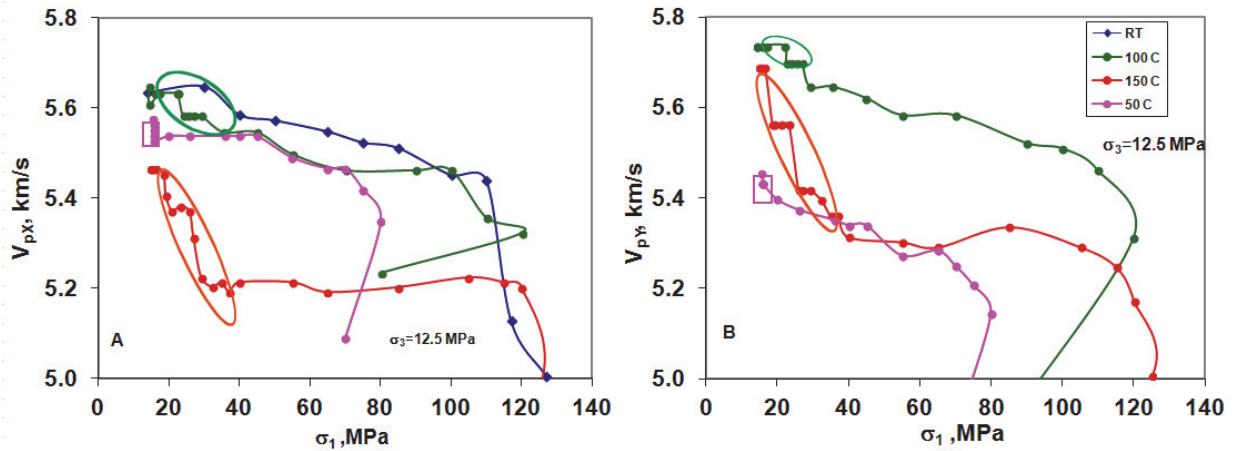


Figure 118: (a) Evolution of V_P along the X axis for RT, 50°C, 100°C and 150°C during in-situ heating (values shown within oval and rectangle), and as a function of differential stresses under constant σ_3 and constant displacement control and (b) Evolution of V_{PY} in the other horizontal axis

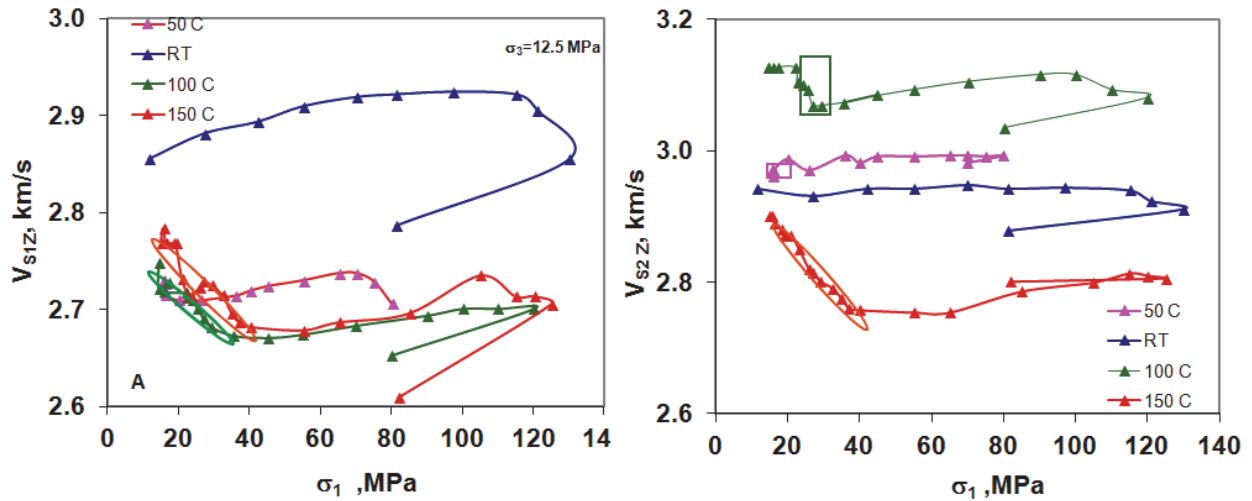


Figure 119: Evolution of (a) V_{S1Z} and (b) V_{S2Z} (vertical direction) for RT, 50°C, 100°C and 150°C during in-situ heating (values shown in ovals and rectangles)

The rate of velocity decrease accelerates closer to failure strength in all of the specimens being tested. Figure 120 shows the variation of comparative shear wave velocities as a function of in situ heating and differential stresses for X axis for RT and heated specimens.

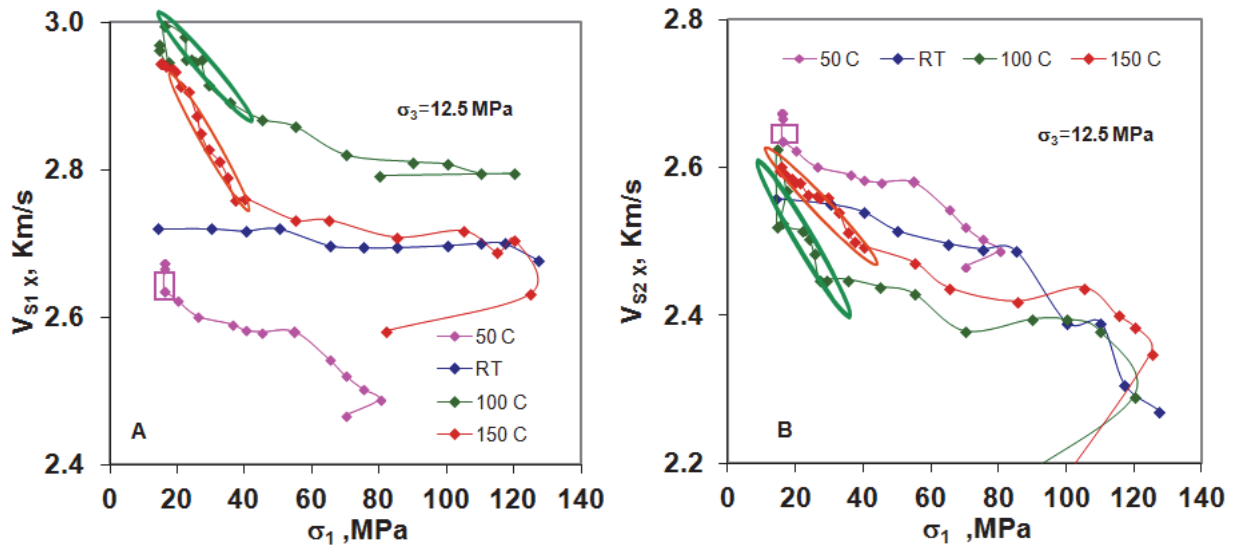


Figure 120: Evolution of (a) V_{S1} and (b) V_{S2} along the X axis for RT, 50°C, 100°C and 150°C during in-situ heating (values shown in the oval and rectangle)

Variation of calculated Young's modulus (E_{dz}) along the Z axis (parallel to σ_1 direction) as a function of heating and axial stresses shows a characteristic initial decreasing trend for 100°C and 150°C specimens. This trend increases as a function of differential stress increments reflecting on closure of pre-existing microcracks and weak shaly partings prior to the failure (Figure 121). The variation of calculated E_{dY} and E_{dX} during heating show a decreasing order due to lateral expansion of the specimens heated up to 100°C and 150°C as shown in Figures 122 and 123. The E_{dZ} , E_{dY} and E_{dX} show a further decreasing trend as a function of axial stress increments, due to generation of microcracks parallel to the loading direction especially at the stress levels closer to failure strength. Comparison of the E_d calculated for 1st and 2nd cycles of heating at 150°C (Table 14, third row with Table 15, first row) indicates that L8 specimen has experienced a permanent thermal damage, showing that E_{dZ} dropped from 55 GPa to 52 GPa and E_{dX} decreased from 47 GPa to 39 GPa and E_{dY} decreased from 44 GPa to 38 GPa. Higher lateral decrease of dynamic Young's modulus in comparison to axial dynamic Young's modulus indicates that a higher permanent thermal damage was experienced in L8 specimen since it was allowed to expand laterally during first and second cycle of heating. E_{dZ} increases from 48 to 55 when the load reaches 120 MPa prior to the peak strength (130 MPa) due to closure of weak shaly partings.

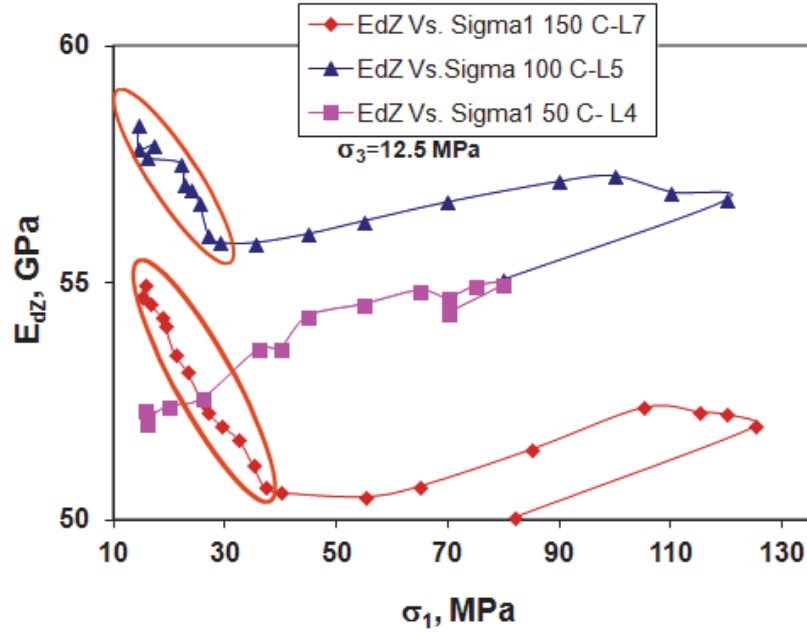


Figure 121: Variation of moduli along Z axis for RT, 50°C, 100°C and 150°C during in-situ heating (values shown in oval)

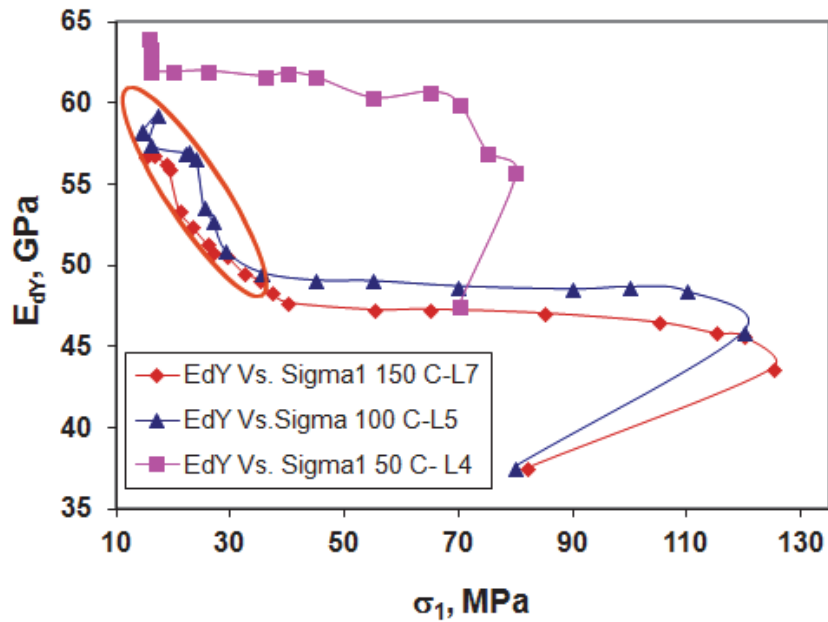


Figure 122: Variation of moduli along Y axis for RT, 50°C, 100°C and 150°C during in-situ heating (values shown in oval)

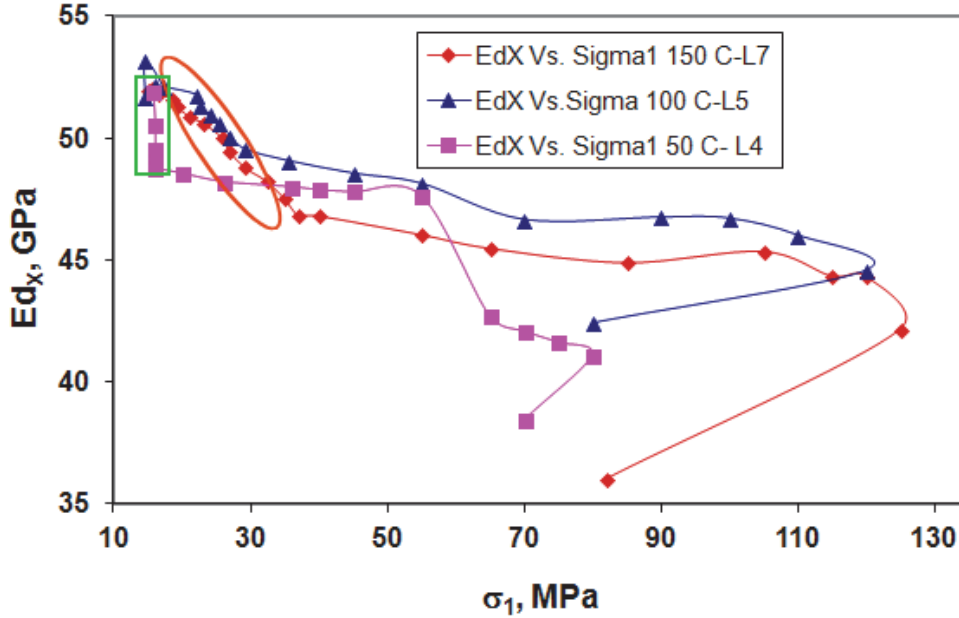


Figure 123: Variation of E_{d_x} (dynamic Young's modulus along X Axis) for RT, 50°C, 100°C and 150°C during in-situ heating (values shown in oval and rectangle)

Figure 124 shows the variation of k measured under hydrostatic stress of 12.5 MPa at ambient temperature for three in-situ heated specimens (points shown in the circles). Permeability values for respective target temperatures show a reduction proportional to the amount of thermal stresses increment caused by thermal expansion that these specimens have experienced. All three specimens show a lower value for permeability after heating. The three specimens show a similar trend of reduction of permeability as a function of differential stresses up to a certain axial stress, followed by an increase prior to failure. The trend is compatible with the trend observed in the evolution of compression and shear wave velocities as a function of axial stress increments. Specimen expansion reduces the specimen stiffness, reflecting on the reduction of seismic wave velocities, and further the calculated dynamic Young's modulus. The reduction of seismic wave velocities may indicate that intra-matrix expansion of pore spaces takes place with incremental temperature changes. This phenomenon is more evident for specimens heated up to 150°C.

Figure 125 shows the result of UCS and triaxial compressive strength for all the specimens tested at ambient and target temperatures. Based on the limited test data, it is observed that uniaxial and triaxial compressive strengths for 100°C specimens show higher values than other specimens tested for the same properties, i.e., UCS and coupled THM experiments.

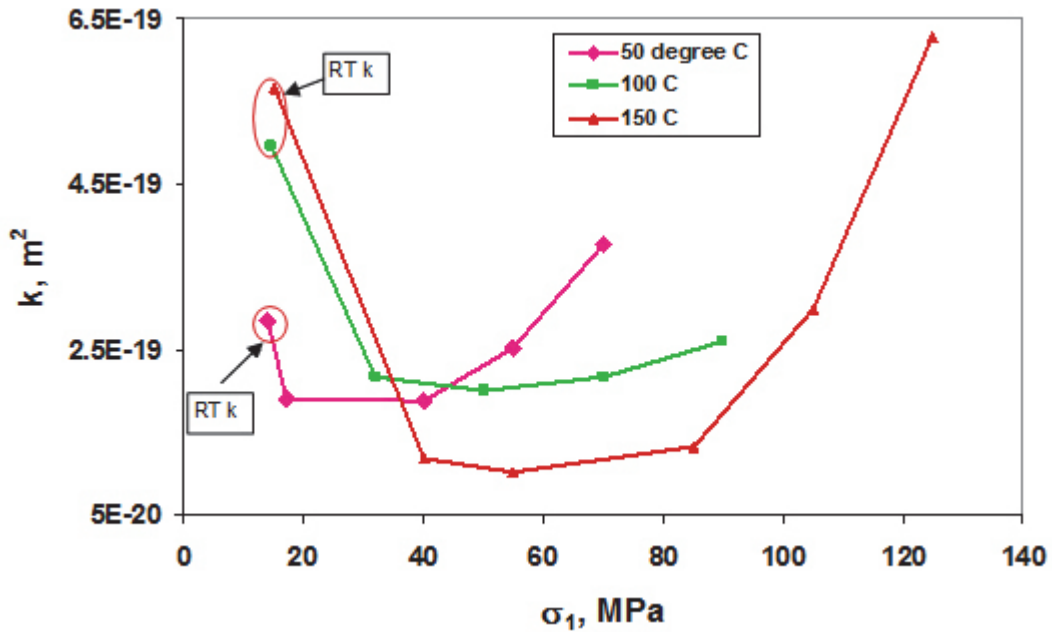


Figure 124: Permeability as a function of differential stresses measured under ambient temperature (25°C, RT K) and elevated temperatures

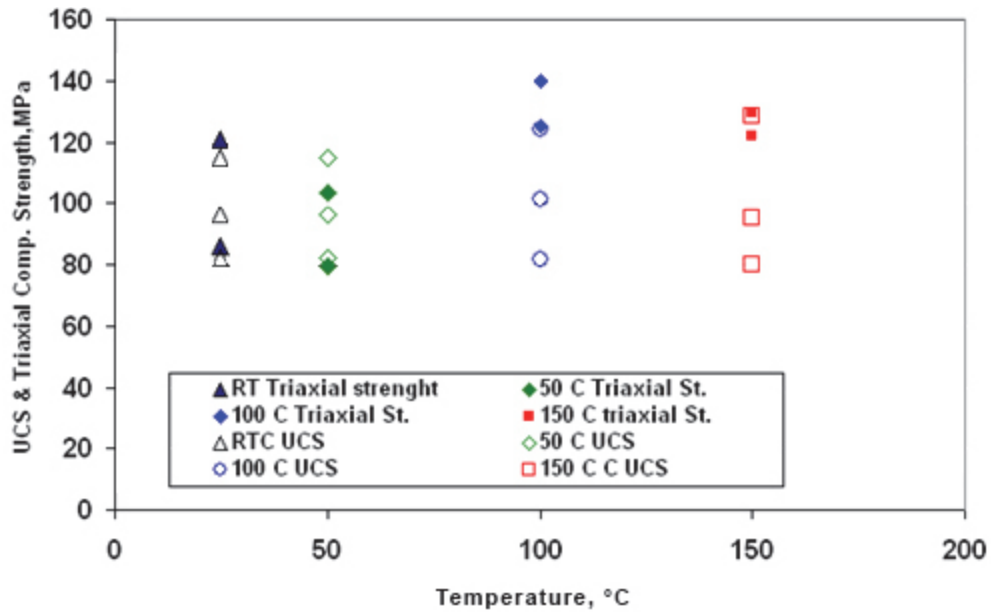


Figure 125: UCS and triaxial compressive strengths as a function of temperature for all specimens in Phase 2

This study shows that there is a self-consistent relationship among strength, deformation (static and dynamic elastic constants), wave velocities, and permeability (k) during the various stages of the THM experiment for Cobourg limestone specimens.

4. SUMMARY AND CONCLUSIONS

The effects of thermo-hydro mechanical (THM) coupling processes on the properties of Cobourg limestone were investigated in a two phase experimental approach.

Under the Phase 1 experiments, two groups of experiments were performed to characterize the Cobourg limestone under thermo-mechanical (TM) and thermo-hydraulic (TH) coupling processes. Uniaxial compressive strength (UCS) tests on 50 mm diameter dry and saturated Cobourg limestone specimens, retrieved during the field investigation of Darlington Nuclear Station, with and without pre-heated treatment with temperatures ranging from ambient to 125°C. These tests were aimed to study the TM behaviour of the limestone. The third group of tests was designed to investigate TH coupled behaviour of the rock utilizing the Floor Stander Acoustic System and a servo-controlled permeameter to measure the changes in ultrasonic wave-velocities and permeability in the rock with temperature. All tests were performed on 38 mm diameter specimens under a hydrostatic condition of up to 12.5 MPa to simulate a nominal repository depth of 500 m.

Similar to Phase 1, the first group of tests in Phase 2 studies the TM behaviour of the Cobourg limestone which involved UCS tests on both dry and saturated heat and non-heat treated specimens. The specimens were heat treated to 50°C, 100°C and 150°C prior to the UCS testing. The second set of experiments was carried out on in-situ heated specimens to investigate the THM coupling effects by measuring changes in various mechanical, geophysical and hydraulic parameters, such as stress-strains, ultrasonic wave-velocities, static and dynamic elastic constants and permeabilities, in a geophysical imaging Hoek type triaxial cell.

The results from these experiments suggest:

1. The Cobourg Limestone is fairly strong. From Phase 1 testing, an average uniaxial compressive strength of 121 MPa for dry 50 mm diameter specimens from the field investigation of Darlington Nuclear Generating Station was obtained. When the rock was subjected to re-saturation, the average UCS reduced to 83 MPa. Because the limestone was fairly heterogeneous and can be affected by sampling at different locations, the average dry UCS measured from the specimens retrieved from the St. Mary Quarry, Bowmanville, for Phase 2 testing was 82.7 MPa. The saturated specimens also revealed a similar reduction in rock strength with an UCS of 63 MPa.

A similar trend was observed for Young's moduli.

2. There is no specific trend of strength or Young's modulus noticed from both Phase 1 and 2 testing on specimens subjected to pre-heating processes.
3. The results of the Floor Stander testing suggest that the permeability of the sample decreases with an increase in hydrostatic stress. The permeability also decreases with temperature. With temperature increased from ambient temperature (25°C) to 125°C, the permeability decreased by about an order of magnitude. The seismic wave velocity evolution and negative strain registered by axial LVDTs further confirms the thermal expansion of the samples, and that the observed reduction is a function of temperature increment. This permeability reduction could be the result of the expansion of clay material in the sample causing clogging of the interconnected

- pore fluid network, i.e., the throat effect. Desaturation of the specimen could be another reason for permeability reduction with temperature increase.
4. All THM tests in Phase 2 were conducted by maintaining 5 MPa pore pressure on each end of specimens allowing the amount of thermal pressurisation caused by the difference in thermal expansion between solid phase of rock and pore fluid to be measured. This provides a better understanding on the THM behaviour of Cobourg limestone specimens under thermal loading up to 150°C.
 5. The evolution of seismic wave velocities, thus the dynamic elastic constants, with temperature reflect the effect of thermal expansion (or stress) or sample dehydration closer to the loading platens proportionally as temperature is raised to 150°C. This variation is observed to be highest for 150°C and it entails the decrease of the elastic constants of the calcite minerals as the temperature increases.
 6. The evolution of seismic wave velocities and dynamic elastic constants as a function differential stresses observed in the limestone captures the effect of induced damage/swelling occurring in the specimens tested under the influence of thermal heating. Shear wave velocity measured seems to be more sensitive to the heating stage coupled with micro-thermal expansion and micro-damages due to unequal thermal responses of constituent minerals and clay component of the specimens. In contrast, the compressional wave velocities are more affected by the progressive growth and opening of micro-cracks during the differential compression loading. Our study shows that the elastic wave velocity measurements provide better indicators of earlier dilatancy than the diametral strain measurements.
 7. All Cobourg limestone specimens show a systematic decrease of permeability (under THM processes) as a function of heating and differential stress increments followed by an increase in permeability values responding to fracture initiation and propagation parallel to the major principal stress prior to failure. This behaviour is consistent with the evolution of seismic wave velocities with heating, differential stress increments, and the deformational pattern of tested specimens.
 8. Experiments performed during various stages of this study estimate extremely low rock matrix permeabilities for the argillaceous Cobourg limestone, perpendicular to partings, in the range of 10^{-19} to 10^{-20} m².
 9. A constant thermal stress rate of 0.21MPa/°C is measured during heating of specimens up to 100 and 150°C. A temperature-dependent thermal coefficient of expansion ($\alpha = 3$ to 3.5×10^{-5} K⁻¹) is suggested for Cobourg limestone based on the current investigations for specimens tested under described triaxial condition.

ACKNOWLEDGEMENTS

We are grateful to Mr. Mark Jensen, Dr. Monique Hobbs, Mr. Tom Lam, Dr. Ben Belfadhel and Dr. Toivo Wanne (formerly) of the Nuclear Waste Management Organization, Toronto, Ontario for their interest in this research and their continuous support. We are grateful to Mr. Sebastian D. Goodfellow for his contribution in sample preparation, help during testing with GICA cell.

REFERENCES

- Boulin, P.F., P. Bretonnier, N. Glan, J.M. Lombard. Contribution of the steady state method to water permeability measurement in very low permeability porous media, *Oil and Gas Science and Technology-Rev. IFP Energies nouvelles*, DOI: 0.2516/ogst/2011169.
- Brace, W. F., J.B. Walsh and W.T. Frangos. 1968. Permeability of granite under high pressure. *J. Geophys. Res.* 73(6), pp. 2225-2236.
- Christensen, N.I. 1990. Seismic velocities in "Practical handbook of physical properties of rocks and minerals." R.S. Carmichael, ed. CRC Press, Boca Raton, Florida, 429-546.
- Cooper, H. and G. Simmons. 1977. The effect of cracks on the thermal expansion of rocks. *Earth Plan. Sci. Lett.* 36:404-412.
- Gueguen, Y. and V. Palciauskas. 1998. Introduction to the physics of rock, Princeton University Press, Princeton.
- Horseman, S. T. and T. J. McEwen. 1996. Thermal constraints on disposal of heat-emitting waste in argillaceous rocks. *Eng. Geol.*, 41, pp. 5-16.
- ISRM. 1977. Suggested method for determining uniaxial compressive strength of rock materials. Document No. 1, first revision.
- ISRM. 1981. Part 1: Suggested method for determining water content, porosity, density, absorption and related properties. *ISRM Suggested Methods; Rock Characterization testing and monitoring*, Int. Soc. Rock Mech. Pp. 81-89.
- Roy, D.M., B.E. Scheetz, J. Pommersheim and P.H. Licastro. 1993. Development of transient permeability theory and apparatus for measurements of cementitious materials, Material research laboratory, The Pennsylvania State University, University Park, Pennsylvania.
- Tiab, D. and E.C. Donaldson. 1996. *Petrophysics: theory and practice of measuring reservoir rock and fluid transport properties*, Gulf Publishing Company, Houston, Texas.
- Zhang, C-L., T. Rothfuchs, K. Su and H. Nasser. 2007. Experimental study of the thermo-hydro-mechanical behaviour of indurated clays. *Physics and Chemistry of the Earth*, 32: 957-965.

APPENDIX A: ACOUSTIC EMISSION ANALYSIS

During each experiment performed in the geophysical imaging cell A (GICA), AE was continuously acquired by 18 piezo-electric transducers at a sampling rate of 10MHz. After each experiment the continuous data was harvested using ASC InSite software and the conclusion was that AE was not recorded at any time during 9 experiments. The hypothesis was that AE produced by a soft limestone was occurring at lower frequencies and therefore was well below the excitation range of the transducers that were used. Appendix B details a uniaxial experiment performed on a Cobourg limestone core (190 mm × 100 mm) with the purpose of characterizing the frequency content of acoustic emissions (AE) produced by this rock.

Eight Physical Acoustic Corporation (PAC) R6 transducers, with an effective range of 35 to 100 kHz were secured to the rock using electrical tape and ultrasonic couplant. Flat patches were ground into the cylindrical wall of the sample to allow for full contact between the sensor surfaces and the rock. The PAC sensors were connected to Cooknell Electronics CA6 amplifiers using BNC cables. The CA6 amplifier has a bandwidth of 10 kHz to 10MHz and maximum output of 1V_{rms}. Amplified ultrasonic data was continuously acquired by three ASC Richter units sampling at 10 MHz. After the experiment, continuous AE data was harvested using the ASC InSite Auto Leach module. In this module, an event is defined by a set number of channels observing an event over a set amplitude threshold within a set time window. The discrete AE was then source located using the ASC InSite Location module. Arrival times were initially auto-picked and then assuming a known velocity structure, a downhill simplex method was used with a minimum of 5 P-wave arrivals. Figures A1 and A2 show the schematic experimental and Laboratory setups for the experiment, respectively.

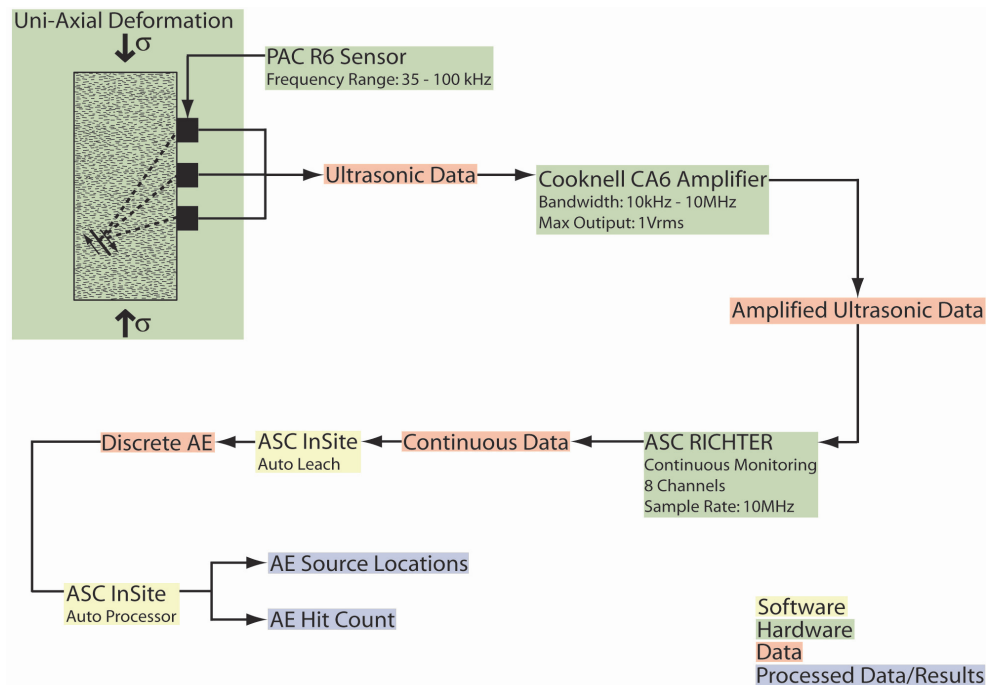


Figure A1: Schematic of experimental set-up, data processing steps, and processed data

A limestone core, 191mm long and 101.3mm in diameter had its ends ground flat and parallel using a surface grinder. Flat spots were created at eight locations on the cylindrical surface where sensors would be placed. Sensor coordinates were chosen to maximize focal coverage.



Figure A2: Experimental set-up, showing larger specimen of Cobourg limestone secured with 8 PAC AE sensors and continuous data acquisition system under UCS test

The coordinate system and sensor locations are presented in Figures A3 and A4.

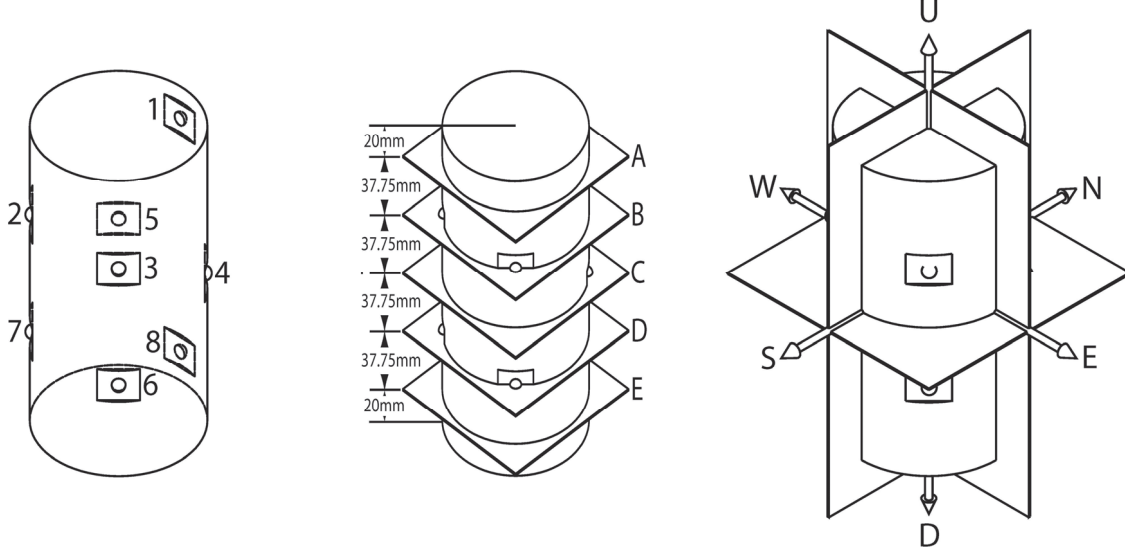


Figure A3: Coordinate system and AE sensor locations

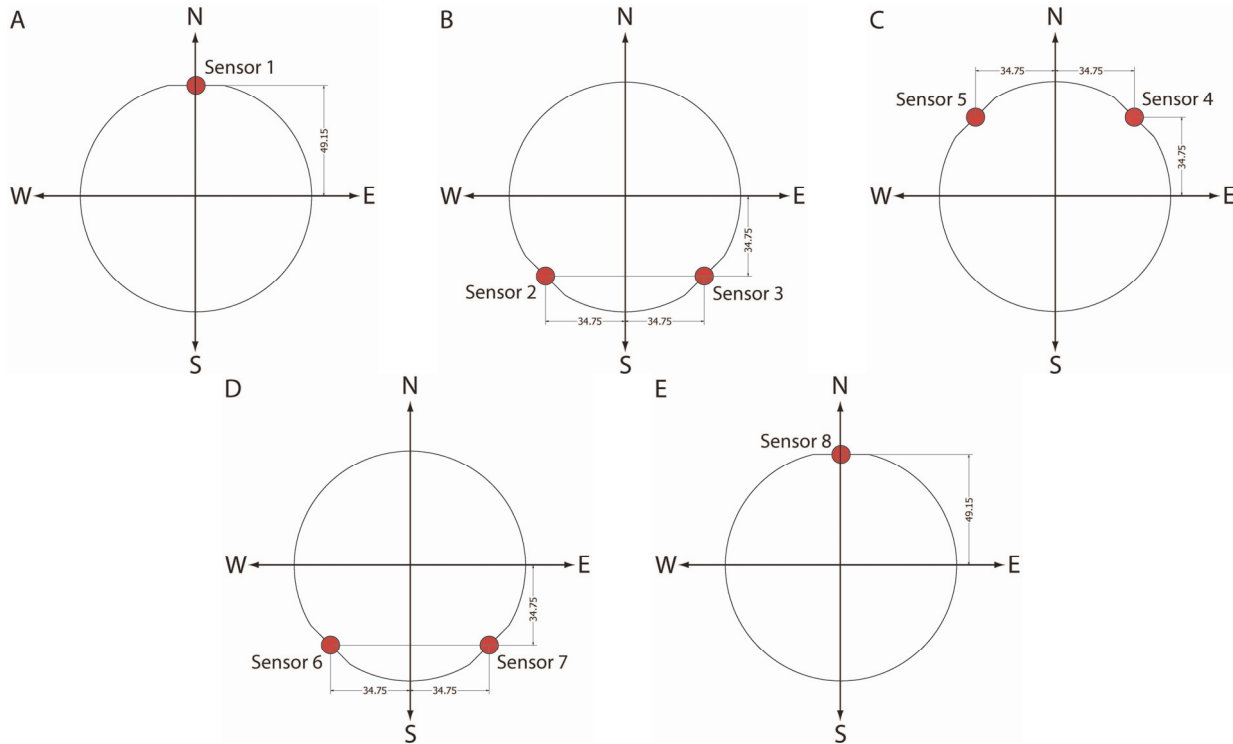


Figure A4: AE sensor locations

The room dry limestone specimen was secured in MTS compression machine and loaded at a constant strain rate of 5.2×10^{-6} . Stress and strain were monitored using load cells within the loading mechanism and LVDTs respectively. Stress, AE hits per second and cumulative AE hits are presented in Figure A5. The experiment lasts roughly 12 minutes and a peak stress of 100MPa was reached. Continuous AE data was harvested with the following criterion for hit

count analysis: An event is defined as a minimum of three sensors exceeding 100mV. A total of 9000 events were recorded with the previously mentioned criterion.

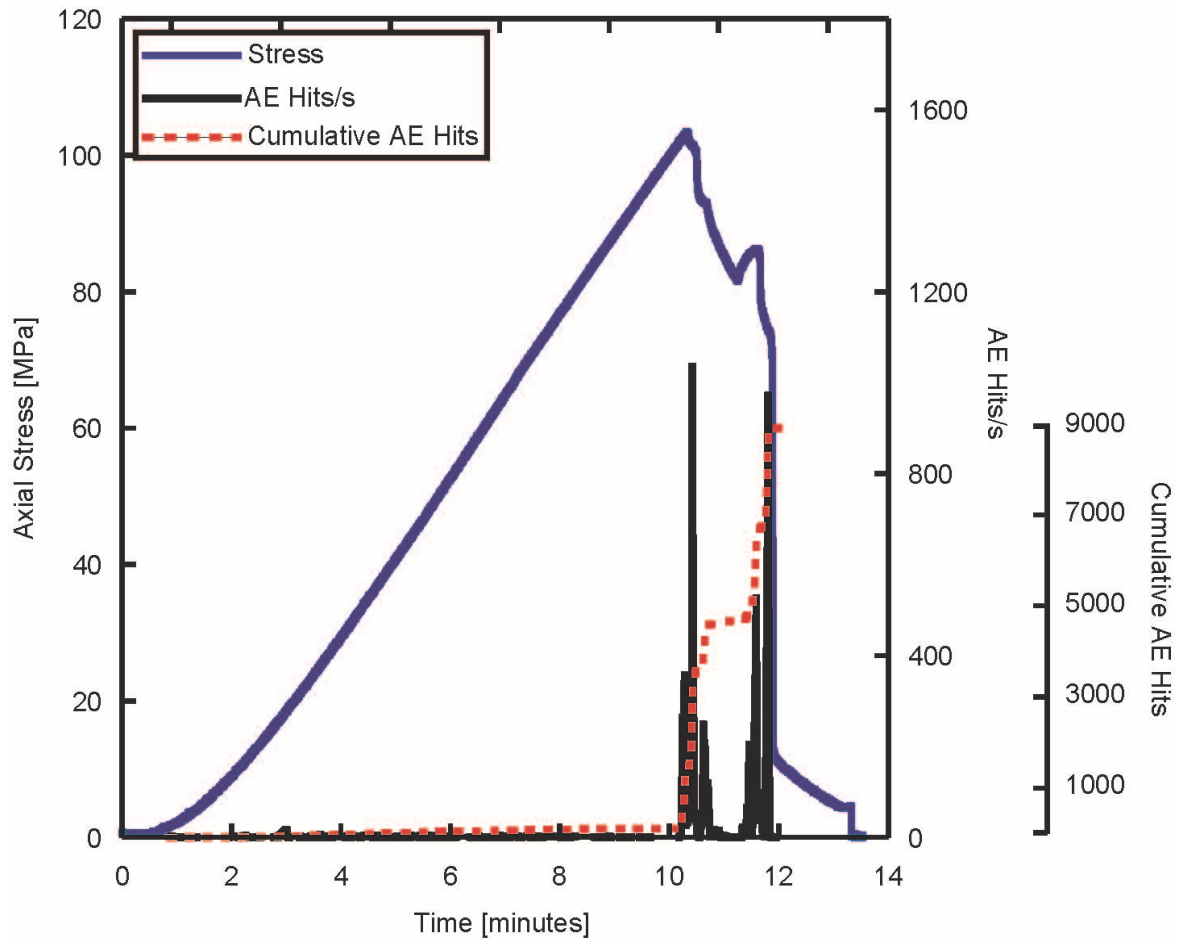
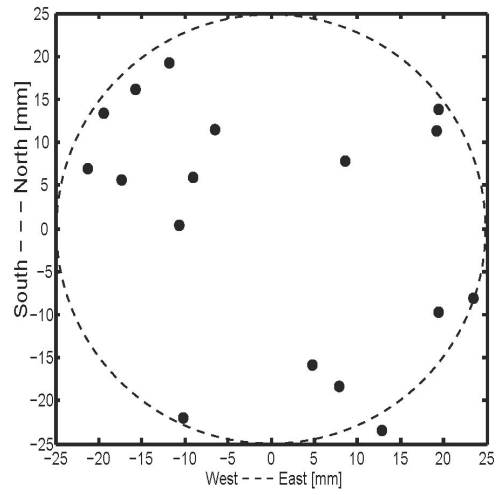
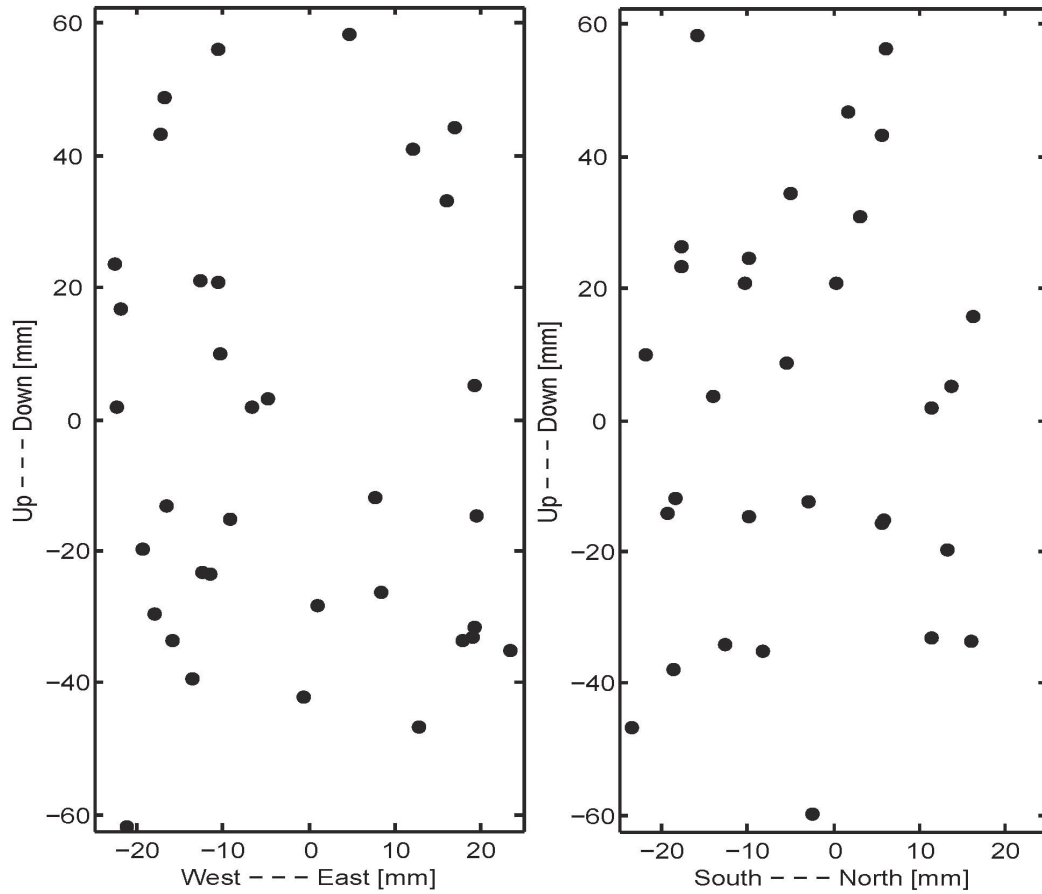


Figure A5: Stress, AE Hits/s and Cumulative AE Hits plotted against time

Continuous AE data was harvested using a different criterion for source location analysis. An event was defined as a minimum of 4 sensors exceeding 500mV. A total of 1000 events were recorded with the previously mentioned criterion. After auto-picking the waveforms and computing the source locations, the events were filtered and non AE events were discarded. The remaining waveforms were picked manually and events were relocated. After this process, 79 events remained and their projected locations on three orthogonal planes are presented in Figure A6. The AE source locations do not highlight any major failure features which are due to the relatively small number of events which were successfully located. The number of successful AE source locations could be increased by optimizing the picking algorithm and velocity structure and adding more AE sensors. Tested Cobourg limestone specimen is shown in figure A7, revealing failure pattern characterized with axial and longitudinal cracks and failure planes.



a) South-North/West-East plane.



b) Up-Down/West-East plane.

c) Up-Down/South-North plane.

Figure A6: Acoustic emission source locations projected on three orthogonal planes



Figure A7: Tested larger Cobourg limestone specimen for AE analysis showing failure pattern characterized with axial failure planes

Eight waveforms from event #1 are presented in Figure A8 with their arrival times displayed by vertical red lines. The waveform window is 8190 sample points or 0.819ms long and the peak voltage is 985mV.

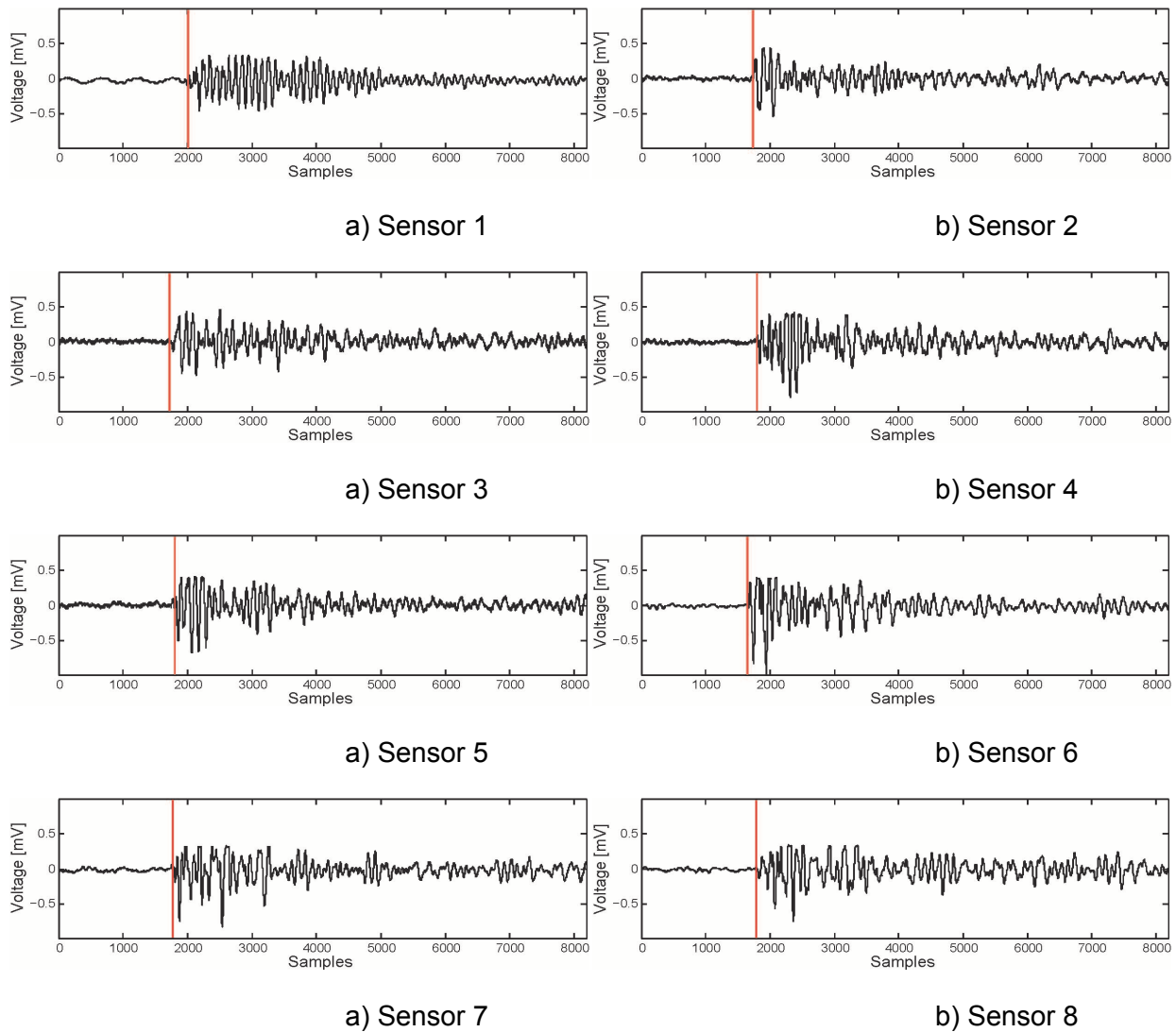


Figure A8: Waveforms and auto-picking results for Event #1

AE waveforms from Cobourg limestone experiment and a tri-axial Westerly granite experiment were compared to test our hypothesis. The Westerly granite waveform is only 4000 samples long but was plotted for 8000 samples to keep a consistent scale. Visually it is clear from the time histories (Figure A9a and c) that AE produced by the limestone has a much lower characteristic frequency. The power spectra of the waveforms were computed and are presented in Figure A9b. Westerly granite AE shows spectral peaks at 442, 684 and 818 kHz (Fig. A9c and d) whereas Limestone AE has a much lower peak at 100kHz (Fig. A8a and b).

The results from this experiment confirm our hypothesis that the reason AE was never recorded during any prior experiments is because GICA transducers have an effective range of 500 kHz to 1.5MHz, which is much higher than the characteristic frequency of Cobourg limestone AE.

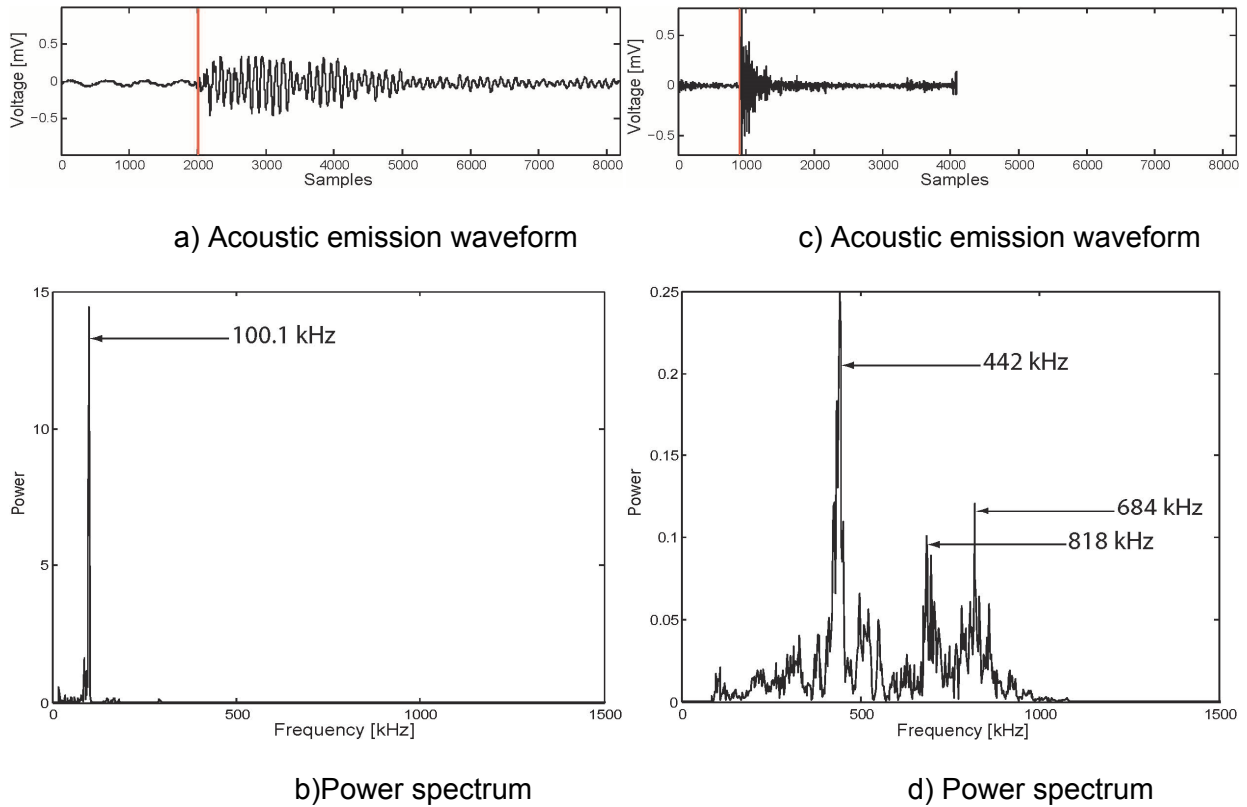


Figure A9: Comparison between Cobourg Limestone (a, b) and Westerly Granite (c, d) acoustic emission waveforms

SCHEMATIC DRAWING OF PERMEABILITY APPARATUS DESIGN

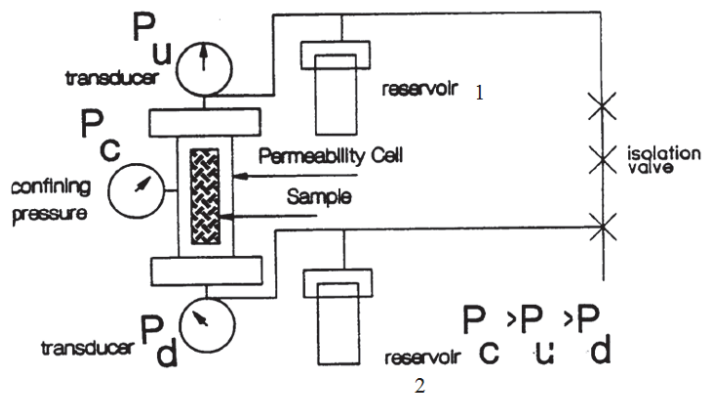


Figure A10: Schematic drawing of permeability apparatus showing detail of pulse decay method. P_u = pore water pressure in the upstream side of the specimen, P_d = pore water pressure in the downstream side of the specimen, P_c = confining pressure, (Roy et al., 1993)

Storage factor calculation for the permeability pulse decay measurement set up using steel specimen:

It is important to measure the storage factor of the testing set-up prior to pulse decay permeability measurements using a steel specimen within the testing set-up. Figure A11 shows such a set-up with a steel specimen in the cell, σ_1 was raised to 50 MPa axially and a confining pressure (P_c) was raised up to 30 MPa within the cell first. Next, using the quizix pump the pore water pressure was raised in steps up to 25 MPa (first by steps of 2 MPa up to 10 MPa and then by steps of 5 MPa up to 25 MPa) and the volume of water needed to pressurize each side of the steel sample was recorded. The pressure was decreased the same way to plot the full cycles of the loading and unloading steps. The applied volume was checked to account for any possible leaks and thus the storage factor estimation was not affected (Figure A12). Figure A13 shows the comparison of the volume of water used to cause 25 MPa of water pressure during the loading and unloading stages. This variation indicates that the storage factor was not affected by any leakage issues. During this test, the ΔP_p and the volume of water were recorded to calculate the storage factor. Figure A14 shows the variation of the calculated storage factor as a function of applied pore water pressure up to 20 MPa on the upstream side. The upstream storage factor decreased with pressure from $2.5E-10m^2$ to $1.3E-10m^2$, (Figure A14). The results obtained herein are consistent with the compressibilities obtained in the test procedure shown in Boulin et al. (2012).

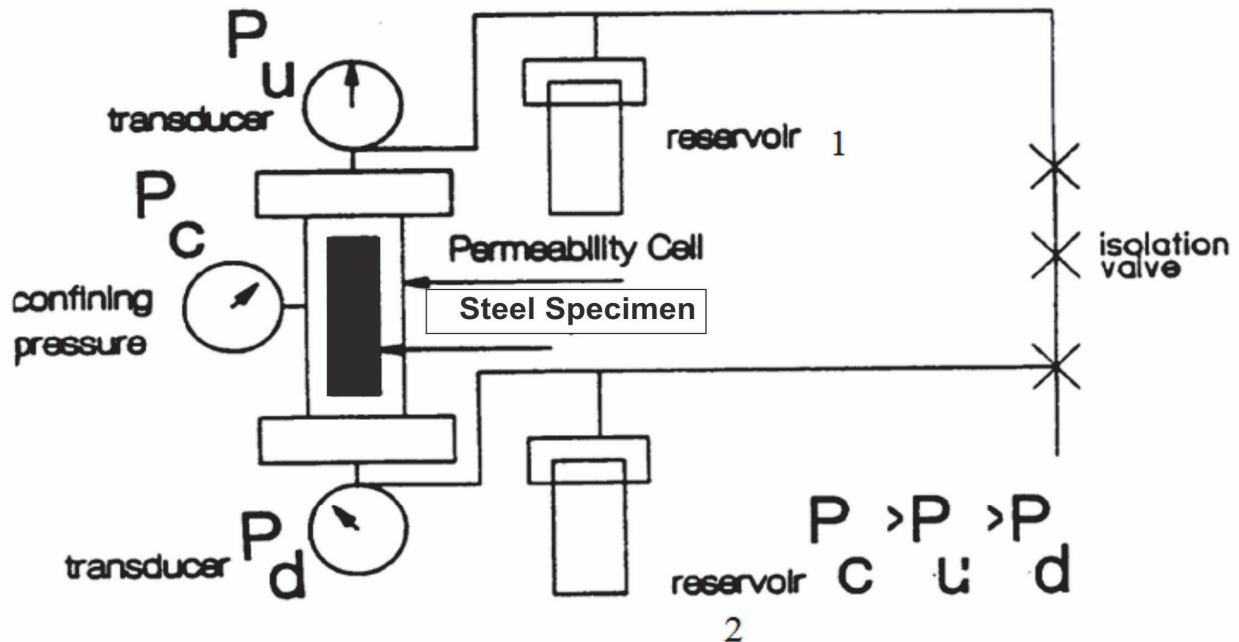


Figure A11. Modified schematic drawing of permeability apparatus showing detail of pulse decay method with the steel specimen within the cell (Roy et al., 1993). The steel sample was used in our permeability testing set-up to measure reservoir storage values and its overall system compressibility. The results found in this calibration test are consistent with the compressibilities shown in Boulin et al. (2012)

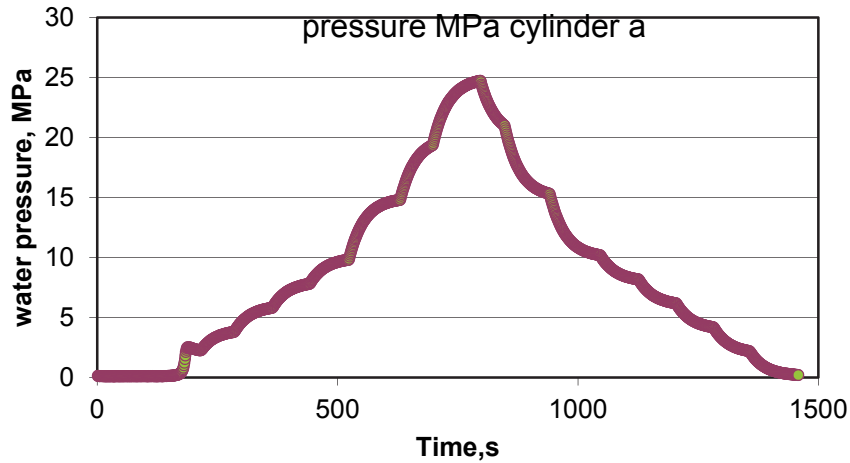


Figure A12. Variation of applied pore water pressure (Pp) as a function of time tested on the top platen (reservoir 1) within the permeability test set-up

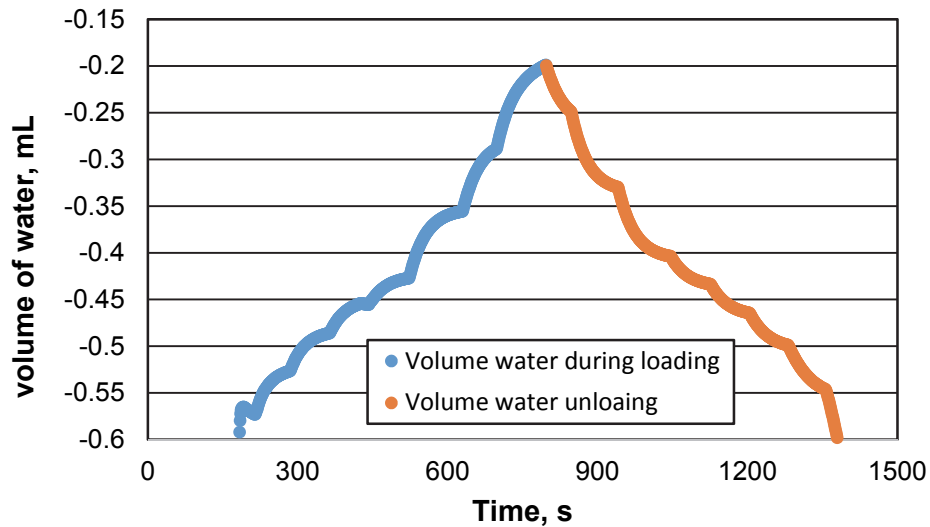


Figure A13. Variation of volume of water used during pore water pressure loading and unloading steps up to 25 MPa within the cell with steel specimen

Following 1 is used to calculate the storage factor for upstream side of testing set-up:

$$S(u) = \rho_w * g * V_{u,d}/dP_w \quad (A1)$$

Where, $S(u)$ storage factor of upstream reservoir, ρ_w = water density, g = gravity, $V_{u,d}$ = volume of water to pressurize upstream reservoir and dP_w = delta water pressure. Figure A14 shows the variation of storage factor as a function of applied water pressure for the testing set-up.

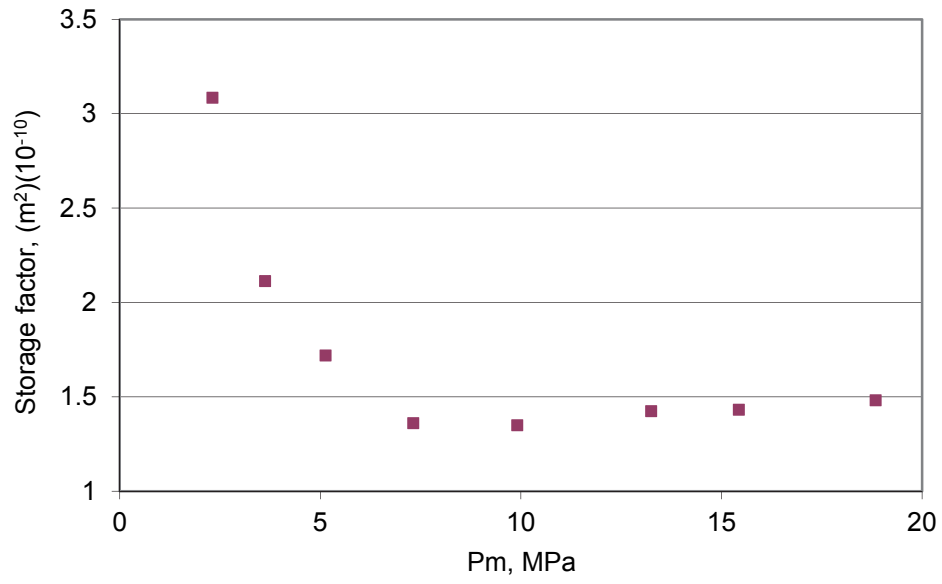


Figure A14. Variation of storage factor as a function of applied pore water pressure for the upstream reservoir